A first evidence of the CMSSM is appearing soon

Programs in Science and Engineering
Course in Material Science
Student ID: 11DS007
Kenichi Sugai

Doctoral Course Supervisor: Associate Professor Joe Sato

Abstract

We explore the coannihilation region of the constrained minimal supersymmetric standard model (CMSSM) being consistent with current experimental/observational results. The requirements from the experimental/observational results are the 125GeV Higgs boson mass and the relic abundances of both the dark matter and light elements, especially the lithium-7. We put these requirements on the calculated values, and thus we obtain the allowed region. Then we give predictions to the mass spectra of the SUSY particles, the anomalous magnetic moment of muon, branching fractions of the B-meson rare decays, the direct detection of the neutralino dark matter, and the number of SUSY particles produced in a 14TeV run at the LHC experiment. Comparing these predictions with current bounds, we show the feasibility of the test for this scenario in near future experiment.

Contents

Chapter 1

Introduction

The challenges of the LHC are to discover the Higgs boson and to search for new physics beyond the standard model (SM). The discovery of the Higgs boson was reported by the ATLAS [1] and the CMS collaborations [2]. Meanwhile no signals of new physics have been observed so far from the LHC. However, nature indicates the existence of physics beyond the SM that accounts for the shortcomings in the SM, e.g., no candidate of dark matter, the origin of neutrino mass, the baryon asymmetry of the universe, and so on.

It is a challenge to confirm the new physics from only experimental/observational data. Theoretical studies in advance are essential to identify the signatures of new physics. We now have measurement data of the Higgs boson, the relic abundance of the dark matter, and so on. What we should do, therefore, is to precisely extract probable parameter space, and predict the signatures in each scenario of new physics by using the measured data.

One of the leading candidates of the new physics is the supersymmetric (SUSY) extension of the SM. A scenario in this extension is the constrained minimal supersymmetric SM (CMSSM) which is a simple but phenomenologically successful framework. In the CMSSM, all of the observables are described by only five parameters, and these parameters are tightly connected with the property of the Higgs boson [3, 4, 5, 6, 7, 8]. The reported mass of the Higgs boson, $m_h \simeq 125\text{GeV}$, suggests heavy SUSY particles [9, 10, 11, 12]. This suggestion is consistent with a null signal of exotics at the LHC. The heavy SUSY particles imply the heavy dark matter in this framework, because the lightest SUSY particle (LSP) works as the dark matter.

Cosmological and astrophysical measurements strongly indicate the existence of dark matter, and numerical simulations suggest that weakly interacting massive particles (WIMPs) are the most feasible candidate for the dark matter [13, 14, 15, 16, 17, 18]. In the CMSSM with R-parity conservation, the bino-like neutralino is the LSP and consequently is a WIMP dark matter candidate. The measured abundance of the neutralino dark matter can be acquired in the coannihilation region[1]. The heavy neutralino dark matter requires a large coannihilation rate. The large coannihilation rate sufficiently reduces the relic number density of the neutralino, and can reproduce the measured abundance of dark matter. The large coannihilation rate needs the tight degeneracy in mass between the neutralino LSP and the stau NLSP (NLSP: next to the lightest SUSY particle) [24, 25]. Indeed in large part of parameter space wherein the mass of the Higgs boson is consistent with the reported one, the mass difference between the neutralino LSP and the stau NLSP is smaller than the mass of tau lepton, m_τ [26, 27]. Such a tight degeneracy makes the stau NLSP a long-lived charged massive particle (CHAMP) [28, 29].

The long-lived CHAMPs can modify the chain of nuclear reactions in a stage of big-bang nucleosynthesis (BBN), and hence distort the primordial abundances of light elements. The success and failure of the nucleosynthesis are quite sensitive to the property of the long-lived CHAMPs, e.g., the

[1]The measured abundance is obtained also in the focus-point region in which measured abundance of dark matter can be reproduced by the large mixing of the bino and the Higgsino components [19, 20]. The latest XENON100 dark matter search, however, excludes most of parameter spaces of the focus-point region [21, 22, 23]

lifetime, the number density, the electric charge, and so on [30, 31, 32, 33, 34, 35, 36, 37, 38, 39, 40, 41, 42, 43, 44, 45, 46, 47, 48, 49, 50, 51, 52, 53, 54, 55, 56, 57, 58, 59, 60, 61]. The success of the nucleosynthesis means to reproduce the measured abundances of light elements. Notice that the measured abundance of lithium-7 (^{7}Li) is reported to be inconsistent with the theoretical prediction in the standard BBN; the measured one is $^7\mathrm{Li/H} = 1.48 \pm 0.41 \times 10^{-10}$ [62] and the theoretical prediction is $^7\mathrm{Li/H} = 5.24 \times 10^{-10}$ [63]. This inconsistency is known as the lithium-7 problem [64], and the success of the nucleosynthesis includes also solving the problem. It is important to emphasize that the success of the nucleosynthesis constrains and predicts the property of the stau NLSP.

In this thesis we give predictions to experimentally identify the CMSSM as the new physics in the light of the natures of the Higgs boson, the measured abundance of dark matter, and the success of the nucleosynthesis. We concentrate on the scenario wherein the mass difference of the neutralino LSP and the stau NLSP is smaller than the mass of tau lepton, and the longevity of the stau is guaranteed by the tight phase space.

Both the mass and the signal strength of the Higgs boson are correlated with parameters of the stop sector. So it sheds light on the sign(μ), m_0, A_0, and $\tan\beta$ which we defer to sfermion parameters. The predictability of the derived relations, however, is not strong because the parameter space contains too many degrees of freedom. It should be noted that, combining the relations from the natures of the Higgs boson and the values of sfermion parameters from the BBN, as we will find, simple relations between m_0 and A_0 are shown. Furthermore the degeneracy of the neutralino LSP and the stau NLSP in the coannihilation region set a relation between $M_{1/2}$ and sfermion parameters. Thus accumulating all of relations and constraints, we give theoretical clues on the likely parameter space of the CMSSM. Then we calculate the observables of terrestrial experiments based on the analysis. After the discovery of SUSY signals, by checking observables with the calculation we make it possible to confirm the CMSSM in the near future.

This thesis is organized as follows. In next chapter, we briefly review the Big Bang Nucleosynthesis and explain Lithium problem. In chapter III, we review the Stau BBN scenario. We show in this chapter that the longevity of the stau, the formation of the bound state between long lived stau and nuclei, exotic nuclear reactions, and relic density of stau at he BBN era. We show the solution for the lithium problem and relic abundance of the dark matter in the light of MSSM. In chapter IV, we explore allowed parameter space of the CMSSM. In Sec. 4.1 we recall the framework of the CMSSM, keeping an eye on the coannihilation scenario. Then we set the constraint on some input parameters from the viewpoint of the report of the Higgs boson and the observed abundances of both dark matter and light elements. The derived model space is for stau-neutralino coannihilation region and that solves the Li problem. The constraints is substantially weakened without considering the Li problem, and hence the assumption is important. In Sec. 4.2, we show the allowed region of the CMSSM parameters obtained by the constraints. The relations of the parameters are derived from the results. In Sec. 4.3, we show the predictions for SUSY mass spectrum, the anomalous magnetic moment of the muon, branching fractions of the B-meson rare decays, and direct detection of the neutralino dark matter in the allowed region. We show the number of the signals of the long-lived stau and the neutralino at the LHC experiment, and then we discuss the verification of the scenario in Sec 4.4. Chap. 5 is devoted to a summary and a discussion.

Chapter 2

Review of the Big Bang Nucleosynthesis

We review the mechanism of the Big Bang Nucleosynthesis (BBN) in this chapter. We roughly divide the processes of the BBN into three part as follow. Firstly the ratio between number density of neutron (n) and proton (p) is fixed by chemical equilibrium through weak interaction. Next n and p make the deuteron (d). At the last, helium (He) is made from n, p, and d. We explain each part in detail from now. We refer [56, 65, 66, 67, 68] through the chapter.

2.1 Neutron - Proton ratio ($T \leq 0.8\mathbf{MeV}$)

Before explaining the BBN, we consider the condition of the universe when the temperature of the that is higher than 1 MeV. p and n exchange each other through the following reactions,

$$n \leftrightarrow p + e^- \bar{\nu}_e, \tag{2-1-1a}$$

$$\nu_e + n \leftrightarrow p + e^-, \tag{2-1-1b}$$

$$e^+ + n \leftrightarrow p + \bar{\nu}_e. \tag{2-1-1c}$$

If the timescale of these reactions is shorter than the age of the universe, the system is in the chemical equilibrium. Then the chemical potential of these particles have a relation as follows:

$$\mu_n + \mu_\nu = \mu_p + \mu_e. \tag{2-1-2}$$

Here we consider that the temperature of the universe is $\mathcal{O}(1\mathrm{MeV})$, (anti) electron and (anti) neutrino are relativistic particles. Then the number density of the (anti) electron $n_{e^-}(n_{e^+})$ and (anti) neutrino $n_{\nu_e}(n_{\bar{\nu}_e})$ have a relation with T and chemical potential as follows:

$$\begin{aligned} n_{e^-} - n_{e^+} &= \frac{1}{3}\mu_e T^2, \\ n_{\nu_e} - n_{\bar{\nu}_e} &= \frac{1}{6}\mu_{\nu_e} T^2. \end{aligned} \tag{2-1-3}$$

We use following facts that i) $\eta_\mathrm{b} \equiv n_\mathrm{b}/n_\gamma \simeq 10^{-10}$ (η_b is the baryon to photon ratio) and ii) the universe is neutral, i.e., $n_\mathrm{b} \simeq n_{e^-} - n_{e^+}$ to derive a relation as follows:

$$\mu_e \ll T \tag{2-1-4}$$

Therefore we neglect the chemical potential of e. Here we assume that the chemical potential of μ_e is also negligible. Then the relation Eq. (2-1-2) becomes as follows:

$$\mu_n = \mu_p \tag{2-1-5}$$

Meanwhile n and p are non-relativistic particles, and hence n_p and n_p are expressed as follows:

$$n_p = 2\left(\frac{m_p T}{2\pi}\right)^{3/2} \exp\left[-\frac{m_p - \mu_p}{T}\right], \tag{2-1-6}$$

$$n_n = 2\left(\frac{m_n T}{2\pi}\right)^{3/2} \exp\left[-\frac{m_n - \mu_n}{T}\right], \tag{2-1-7}$$

Using Eqs. (2-1-5), (2-1-6), and (2-1-7), we write the ratio of n_n and n_p as follows:

$$\frac{n_n}{n_p} = \exp\left(-\frac{Q}{T}\right), \tag{2-1-8}$$

$$Q = m_n - m_p = 1.293 \quad [\text{MeV}]. \tag{2-1-9}$$

In this way, the weak interaction reactions fix the ratio between n_n and n_p. We see from Eqs. (2-1-8) and (2-1-9) that the number density of n is smaller than that of p because the mass of n is larger than that of p.

However the reaction rates of the exchange process between n and p decrease with decreasing the temperature of the universe. When the reaction rates become smaller than the Hubble expansion rate (H), n and p decouple from the thermal bath, and the ratio between n_n and n_p is frozen-out. Here we show the temperature of the universe when the ratio is frozen-out. To do this, we consider the reaction rate of the exchange processes between n and p. We obtain the reaction rate by integrating the square amplitude of reaction process times the density in the phase space through the all momentum of final state. For the conservation of the energy and the momentum, we put the delta function in the calculation. For example, the reaction rate of inverse process of Eq.(2-1-1b) is given by

$$\Gamma_{pe\to\nu n} = \frac{1}{(2\pi)^5}\int f_e(E_e)[1 - f_\nu(E_\nu)]|\mathcal{M}|^2_{pe\to\nu n}\delta(p_p + p_e - p_\nu - p_n)\frac{d^3p_\nu}{2E_\nu}\frac{d^3p_n}{2E_n}, \tag{2-1-10}$$

where $f_i(E_i)$ is the density in the phase space, and E_i and p_i are the energy and four momentum of particle$i$, respectively. Reaction amplitudes of Eqs. (2-1-1a), (2-1-1b), and (2-1-1c) are proportional to that of β decay, and hence expressed as follows,

$$|\mathcal{M}|^2 \propto G_F^2(1 + 3g_A^2), \tag{2-1-11}$$

where G_F is the fermi coupling constant and $g_A \simeq 1.26$ is the axial vector coupling constant.

The value both of Q and electron mass determine the integral range. We here define following physical parameters with no dimension for simplicity of the calculation.

$$q = \frac{Q}{m_e}, \quad \epsilon = \frac{E_e}{m_e}, \quad z = \frac{m_e}{T}, z_\nu = \frac{m_e}{T_\nu}, \tag{2-1-12}$$

where T_ν is the temperature of the neutrino. Using the parameters, we give the reaction rate as followings,

$$\Gamma_{pe\to\nu n} = \frac{G_F^2(1 + 3g_A^2)m_e^5}{2\pi^3}\int_q^\infty d\epsilon \frac{\epsilon(\epsilon - q)^2\sqrt{\epsilon^2 - 1}}{(1 + e^{\epsilon z})(1 + e^{(q-\epsilon)z_\nu})} \tag{2-1-13}$$

The behavior in the limits of high or low temperature is given by,

$$\Gamma_{pe\to\nu n} \to \begin{cases} \dfrac{G_F^2(1 + 3g_A^2)m_e^5}{2\pi^3}\left(\dfrac{T}{m_e}\right)^3 \exp\left(-\dfrac{Q}{T}\right) & \text{for} \quad T \ll Q, m, \\ \dfrac{7}{60}\pi(1 + 3g_A^2)G_F^2 T^5 & \text{for} \quad T \gg Q, m. \end{cases} \tag{2-1-14}$$

We compare the reaction rate with the Hubble expansion rate to check which the system being in the nuclear statistical equilibrium (NSE) or no NSE. Taking the fact that the universe was dominated by radiation into account, we express the Hubble expansion rate as follows;

$$H \simeq 1.66 g_*^{1/2} \frac{T^2}{m_{\rm pl}} \simeq 5.5 \frac{T^2}{m_{\rm pl}}, \tag{2-1-15}$$

where g_* is the sum of the freedom degree of relativistic particles, $m_{\rm pl}(= 1.22 \times 10^{19}$ GeV) is the planck mass. Using Eq. (2-1-14) and (2-1-15), we obtain the ratio given by

$$\frac{\Gamma}{H} = \left(\frac{T}{0.8 \text{ MeV}} \right)^3. \tag{2-1-16}$$

We see from the equation that the exchange processes occur rapidly when the temperature of the universe is higher than 0.8 MeV, and hence the ratio of number density between p and n is as same as that in NSE. On the other hand, when the temperature of the universe is lower than 0.8 MeV, the exchange processes between n and p become frozen-out, and then the ratio is fixed. Left panel in Fig.2.1 shows $\Gamma_{n\to p}$ and H as a function of T, and right panel shows the ratio n_n/n_p as a function of T. At the $T = 0.1$ MeV, n-p ratio is about 1/7. Almost all n at the temperature make the ^{4}He, and hence the abundance of ^{4}He, $Y = \rho_{\rm He}/\rho_{\rm b}$ (here $\rho_{\rm He}$ is the density of He, and $\rho_{\rm b}$ is that of baryon) finally become as follows:

$$Y = \frac{2(n_n/n_p)}{1 + n_n/n_p} \simeq 0.25. \tag{2-1-17}$$

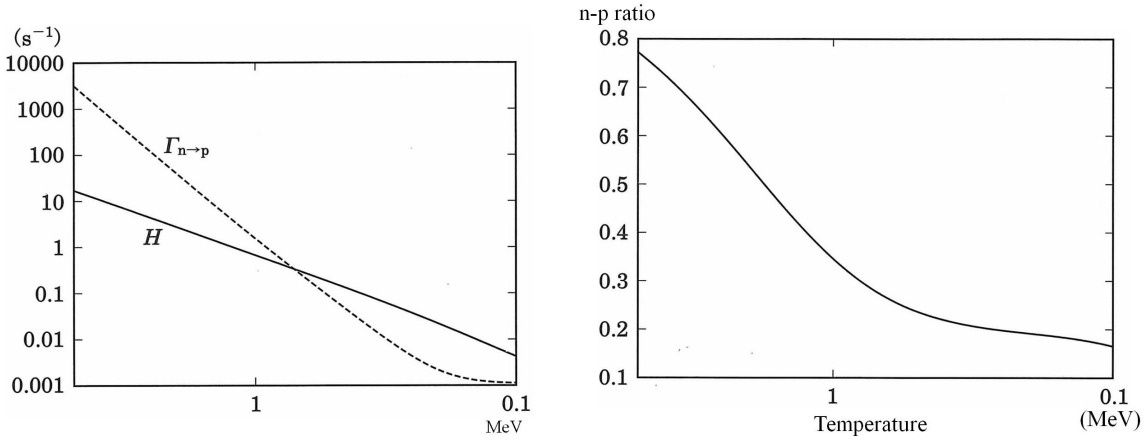

Figure 2.1: Left panel:$\Gamma_{n\to p}$ and H as a function of T. Right panel:The ratio n_n/n_p as a function of T.

2.2 Deuteron synthesis

We can make a rough estimation for the last abundance of He. However we must know the mechanism of deuteron synthesis to make a accurate estimation. Deuteron synthesis is needed to occur helium synthesis.

The fusion of n and p forms the d.

$$p + n \leftrightarrow d + \gamma \tag{2-2-1}$$

The binding energy of d, E_d is 2.22 MeV, and hence photon with energy $\geq E_d$ can break a d into its component n and p.

From now on, we show a rough estimation for the relative numbers density of p, n, and d and derive the starting temperature of deuteron synthesis T_d. Here we define T_d as the temperature at which $n_d/n_n = 1$

Firstly we express the number density of d like Eqs. (2-1-6) and (2-1-7) as follows:

$$n_d = 3\left(\frac{m_d T}{2\pi}\right)^{3/2} \exp\left(-\frac{m_d}{T}\right). \tag{2-2-2}$$

Using Eqs.(2-1-6), (2-1-7) and (2-2-2), we show the relative numbers density of p, n, and d as follows:

$$\frac{n_d}{n_p n_n} = 6\left(\frac{\pi}{m_n T}\right)^{3/2} \exp\left(\frac{E_d}{T}\right), \tag{2-2-3}$$

where we approximate $m_p = m_d/2 = m_n$.

Next we show the T_d. As long as the Eq. (2-2-3) holds true, d - n ratio is expressed as follows:

$$\frac{n_d}{n_n} = 6n_p\left(\frac{\pi}{m_n T}\right)^{3/2} \exp\left(\frac{E_d}{T}\right), \tag{2-2-4}$$

We can write the d-n ratio as a function of T and the η_b if we make some simple assumptions. We see from the Fig. 2.1 that n-p ratio is 0.2 when the exchange processes are frozen-out. Using the fact, we approximate n_p as follows:

$$n_p \simeq 0.8 n_{\mathrm{b}} = 0.8\eta_b n_\gamma = 0.8\eta_b \left[0.243 T^3\right] \tag{2-2-5}$$

Substituting Eq. (2-2-5) into Eq. (2-2-4), we find that the d-n ratio is a relatively simple function of T:

$$\frac{n_d}{n_n} \simeq 6.5\eta_b \left(\frac{T}{m_n}\right)^{3/2} \exp\left(\frac{E_d}{T}\right) \tag{2-2-6}$$

The temperature T_d of deuteron synthesis can be found by solving the equation.

$$1 \simeq 6.5\eta_b \left(\frac{T}{m_n}\right)^{3/2} \exp\left(\frac{E_d}{T}\right) \tag{2-2-7}$$

With $m_n = 939.6$ MeV, $E_d = 2.22$ MeV, and $\eta_b = 6.05\times10^{-10}$, the temperature of deuteron synthesis is $T_d \simeq 0.070$ MeV. Therefore, when the temperature of the universe decreases to 0.070 MeV, the abundance of d rapidly increases and then the helium synthes is ready to start.

2.3 Beyond Deuteron

The d-n ratio does not remain indefinitely at the equilibrium value given by Eq. (2-2-6). Once a significant amount of d forms, many possible nuclear reactions are available. For example, d reacts with p to form ^{3}He:

$$d + p \leftrightarrow^3 \mathrm{He} + \gamma, \tag{2-3-1}$$

Alternatively, d also reacts with n to form ^{3}H, also known as t:

$$d + n \leftrightarrow t + \gamma, \tag{2-3-2}$$

Triton is unstable;it spontaneously decays to ^{3}He as($t \rightarrow^3 \mathrm{He} + e + \bar{\nu}_e$). However, the decay time of t is approximately 18 year ; during the brief time that BBN lasts, $t$can be regarded as effectively stable.

Deuteron also reacts with each other to form ^{4}He:

$$d + d \leftrightarrow^4 \mathrm{He} + \gamma. \tag{2-3-3}$$

Table 2.1: Binding energy and freedom

${}^{A}Z$	B_A[MeV]	g_A
d	2.22	3
t	6.92	2
^{3}He	7.72	2
^{4}He	28.3	1
^{12}C	92.2	1

However, it is more likely that the interaction of two d will end in the formation of t or ^{3}He as follows:

$$d + d \leftrightarrow t + p, , \tag{2-3-4}$$

$$d + d \leftrightarrow {}^3\text{He} + n. \tag{2-3-5}$$

A large amount of t or ^{3}He is never present during the BBN era. Soon after they are formed, they are converted to ^{4}He by reactions such as

$$t + p \leftrightarrow {}^4\text{He} + \gamma, \tag{2-3-6}$$

$${}^3\text{He} + p \leftrightarrow {}^4\text{He} + \gamma, \tag{2-3-7}$$

$$t + d \leftrightarrow {}^4\text{He} + n, \tag{2-3-8}$$

$${}^3\text{He} + p \leftrightarrow {}^4\text{He} + p. \tag{2-3-9}$$

All reactions from Eq. (2-3-1) to Eq. (2-3-7) does not involve neutrinos; they involve the strong nuclear force, and have large cross-sections and fast reaction rates. Thus, once nucleosynthesis begins, d, t, and ^{3}He are all efficiently converted to ^{4}He.

Once ^{4}He is reached, however, the orderly march of nucleosynthesis to heavier and heavier nuclei reaches a roadblock. For such a light nucleus, ^{4}he is exceptionally tightly bound, as shown at Tab.2.1. By contrast, there are no stable nuclei with $A = 5$. ^{5}He and ^{5}Li are not stable nuclei. Thus, ^{4}He is resistant to destruct by p and n. Small amounts of ^{6}Li and ^{7}Li, the two stable isotopes of lithium, are made by reactions such as

$${}^4\text{He} + d \leftrightarrow {}^6\text{Li} + \gamma, \tag{2-3-10}$$

$${}^4\text{He} + t \leftrightarrow {}^7\text{Li} + \gamma. \tag{2-3-11}$$

In addition, small amounts of ^{7}Be are made by reactions such as

$${}^4\text{He} + {}^3\text{He} \leftrightarrow {}^7\text{Be} + \gamma. \tag{2-3-12}$$

The synthesis of nuclei with $A > 7$ is hindered by the absence of stable nuclei with $A = 8$. For example, if^{8}Be is made by the reaction

$${}^4\text{He} + {}^4\text{He} \rightarrow {}^8\text{Be}, \tag{2-3-13}$$

then the ^{8}Be nucleus falls back apart into a pair of ^{4}He nuclei with a decay time of only $\tau = 3\times10^{-16}$s.

2.4 SBBN reaction network

Figure.2.2 shows the output of the SBBN reaction network [56]. We obtain this time evolution of number density of each nucleus by solving the set of Boltzmann equations on the abundances of the different species,

$$\frac{dY_i}{dt} = -H(T)T\frac{dY_i}{dT} = \sum(\Gamma_{ij}Y_j + \Gamma_{ikl}Y_kY_l + ...), \tag{2-4-1}$$

where $Y_i = n_i/n_{\rm b}$ are the time t(or temperature T)-dependent ratios between the number density n_i and the baryon number density $n_{\rm b}$ of light elements $i = p, n, d,^4$ He, and so on. The $\Gamma_{ij...}$ represent generalized rates for element internal conversion and decay that can be determined in experiments and/or inferred from theoretical calculations. $H(T)$ is the temperature dependent Hubble expansion rate.

The full form of the Boltzmann equations should be given in terms of particle distribution functions over energy and momenta. However, in practice, the system of Eq. (2-4-1), which assumes thermal distributions for nuclei, provides an excellent approximation because the frequent interactions with the numerous γs and $e^{\pm}$s in the plasma keep the light elements tightly coupled to the radiation field. The dependence of $H(T)$ on the temperature of the primordial plasma can be further specified;

$$H(T) = T^2 \left(\frac{8\pi^3 g_* G_N}{90}\right)^{1/2}, \quad \text{where} g_* = g_{\rm boson} + \frac{7}{8} g_{\rm fermion}, \tag{2-4-2}$$

where the gs denote the excited relativistic degrees of freedom. This expression needs to be interpolated across the electron-positron annihilation epoch, in which the photon bath is heated with respect to the neutrino reservoir. The neutrinos maintain a quasi-thermal spectrum with temperature

$$T_\nu \simeq \left(\frac{4}{11}\right)^{1/3} T, \tag{2-4-3}$$

in the approximation of full neutrino decoupling at the time of electron-positron annihilation[with small calculable corrections] Following $e^{\pm}$ annihilation, the Hubble rate is given by $H(T) \simeq T_9^2/(2 \times 178{\rm s})$, where T_9 denotes the photon temperature T in units of 10^9 K.

Beginning from the earliest times, the following sequence of of events occurs:

(a) the chemical decoupling of neutrinos from the thermal bath,

(b) the annihilation of electrons and positrons,

(c) the freeze-out of neutrons and photons,

(d) an intermission" between the n/p freeze-out and the deuteron ignition at the end of the "bottleneck",

(e) helium synthesis at $T_9 \simeq 0.85$ (70keV), and

(f) a follow-up stage in which the main nuclear reactions gradually drop out of equilibrium and the abundances of all light elements freeze out.

We explain the Figure from now on. Initially, at $T \gg 10^9 K$, almost aall baryon is in the form of free p and n. As the deuteron density increases upward, however, the point is eventually reached where significant amounts of t, ^{3}He, and ^{4}He are formed. By the time the temperature has dropped to $T \simeq \times 10^8$K, at $t \simeq 600$sec, BBN is essentially over. Nearly all the baryons are in the form of free p or ^{4}He nuclei. The small residue of free n decays into p. Small amounts of d, t, and ^{3}He are left over, a tribute to the incomplete nature of BBN. (t later decays to ^{3}He.) Very small amounts of ^{6}Li, ^{7}Li, and ^{7}Be are made. (^{7}Be is later converted to ^{7}Li by electron capture:$^7{\rm Be} + e^- \rightarrow {}^7{\rm Li} + \nu_e$.) The freeze-out abundances are given by the horizontal lines on the right-hand side of the graph. Although some neutrons are still generated by residual deuteron (d) fusion below $T_9 \simeq 0.1$ (10keV), they are too few in number to cause any further change in the elemental abundances.

Fig. 2.3 shows the abundance of ^{4}He (mass fraction), d, ^{3}He and ^{7}Li (in number of atoms relative to H) as a function of the baryonic density. The thickness of the curves reflect the nuclear uncertainties. They were obtained by a Monte-Carlo calculation using for the nuclear rate uncertainties those obtained by [69] with the notable exception of $^3{\rm He}(\alpha,\gamma)^7{\rm Be}$ [70] and $^1{\rm H}(n,\gamma)d$[71]. The horizontal lines represent the limits on the ^{4}He, d, and ^{7}Li primordial abundances deduced from spectroscopic observations. The vertical stripe represents the baryonic density deduced from

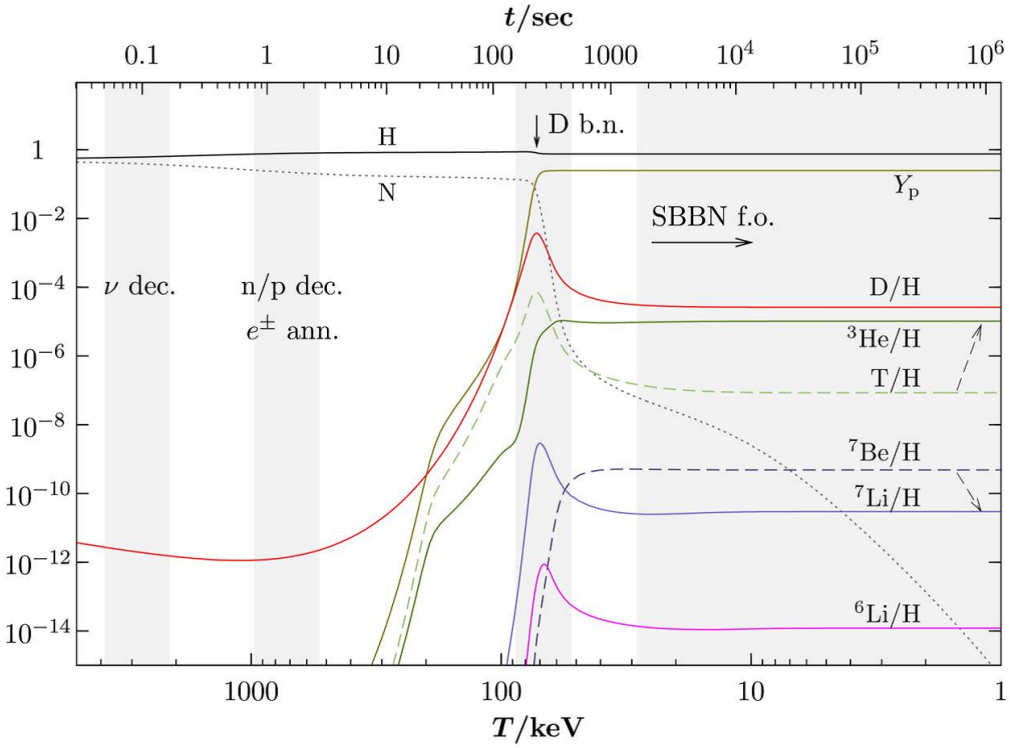

Figure 2.2: Time and temperature evolution of all standard BBN (SBBN) relevant nuclear abundances. The vertical arrow indicates the moment at $T_{9i} \simeq 0.85$ at which most of the helium nuclei are synthesized. The gray vertical bands indicate main BBN stages. From left to right: neutrino decoupling, electron-positron annihilation and n/p freeze-out, d bottleneck, and freeze-out of all nuclear reactions. Proton (p) and neutron (n) are fiven relative to $n_{\rm b}$ whereas Y_p denotes the ^{4}He mass fraction [56].

CMB observations.[72]. The concordance between BBN and observations is in perfect agreement for deuteron. Considering the large uncertainty associated with ^{4}He observations, the agreement with CMB+BBN is fair. The calculated ^{3}He values is close to its galactic value showing that its abundance has little changed during galactic chemical evolution. On the contrary, the ^{7}Li, CMB+BBN calculated abundance is significantly higher than the spectroscopic observations:from a factor of $\simeq 3$ [73] when using the Descouvemont *et al.* library [69] only and the Ryan *et al.* observations [74] (dotted lines in lower panel of Fig. 2.3), to a factor of $\simeq 5$[75, 76] when using the new rates and Li observations [77]. Table 2.4 displays the comparison between BBN abundances deduced from the WMAP results and the spectroscopic observation. The origin of this lithium discrepancy between CMB+BBN and spectroscopic observations remains an open question. Note also that with the new determination of ^{4}He primordial abundances [78, 79], the agreement for ^{4}He becomes marginal. As shown on the figure, and increase of the rate of expansion of the universe during BBN (simulated by an additional effective neutrino family) would improve the situation.

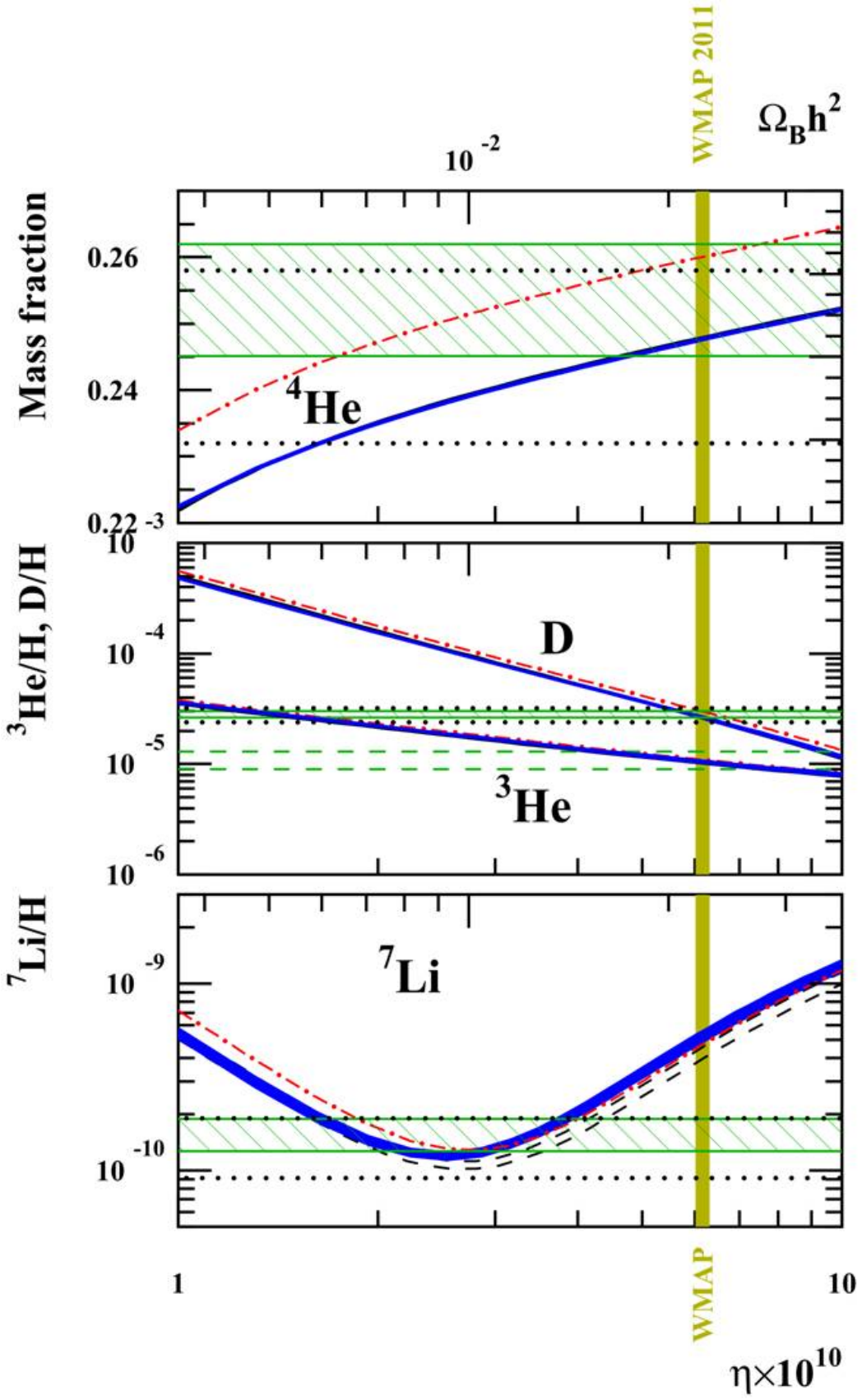

Figure 2.3: Abundances of ^{4}He (mass fraction), d, ^{3}He and ^{7}Li (by number relative to p) as a function of the baryon to photon ratio η_b showing the effect of nuclear uncertainties [76]. The vertical stripe corresponds to the WMAP baryonic density while the horizontal area represent the adopted primordial abundances (dotted lines those adopted in CV10 [76]). The dashed curves represent previous calculations[73] before the re-evaluatioin [70] of the $^3\mathrm{He}(\alpha,\gamma)^7\mathrm{Be}$ rate. The dot-dashed lines correspond to 4 *effective* neutrino families.

Table 2.2: Yields at WMAP baryonic density compared to observations.

	Cyburt et al 2008 [75]	CV10 [76]	Observations	Factor
^{4}He	0.2486 ± 0.0002	0.2476 ± 0.0004	0.2534 ± 0.0083 [79]	$\times 10^0$
d/p	2.49 ± 0.17	2.68 ± 0.15	3.02 ± 0.23 [80]	$\times 10^{-5}$
^{3}He/p	1.00 ± 0.07	1.05 ± 0.04	1.1 ± 0.2 [81]	$\times 10-5$
^{7}Li/p	$5.24^{0.71}_{-0.67}$	5.14 ± 0.50	1.58 ± 0.31 [77]	$\times 10^{-10}$

Chapter 3

Stau BBN Scenario

In this chapter we review the Stau BBN scenario. We simultaneously solve the Lithium Problem and the relic abundance of the dark matter in this scenario as follows.

The Standard Model extended with supersymmetry(SUSY) is one of the models that can accommodate long-lived charged massive particles (CHAMPs). With the R-Parity conservation, the lightest SUSY particle (LSP) is stable and become a cold dark matter. Interestingly, it can offer a long-lived CHAMPs if the LSP is the bino-like neutralino, $\tilde{\chi}_1^0$. Coannihilation mechanism is required to account for the dark matter abundance in this case [114], where the LSP and the next-lightest SUSY particle (NLSP) are almost degenerate in mass. Staus can acquire a long lifetime when the mass difference with the LSP is less than the mass of tau lepton. If the stau lives long sufficient to survive until the BBN era, the staus has an influence on the abundance of light elements through exotic nuclear reactions. The influence depends on the character of the stau, and the character depends on the MSSM parameter space. Therefore we solve the Litium problem and explain the relic abundance of the dark matter by choosing the allowed region in MSSM parameter space.

The outline of this chapter is as follows. In Sec. 3.1 we explain the mechanism of the longevity of the stau. Here we show the analytical equation for the decay of the stau and the dependence of the lifetime of the stau on the mass difference. In Sec. 3.2, we explain how to calculate the bound energy between a stau and nucleus, the cross section and reaction rate for forming the bound state. In this scenario the exotic nuclear reaction happens through the bound state, and hence these calcularion is important. In Sec. 3.3, we review the mechanism of the exotic nuclear reactions. The long-lived stau forms bound state with light nuclei, and then change the nuclei to other nuclei. We calculate the decay rate of these exotic nuclear reactions and show the timescales. In Sec. 3.4 we calculate the relic density of stau at the beginning of the BBN era. We put constraints on the parameter space of MSSM by connecting the calculation of the relic density of stau to the observation of the light elements abundance, which strongly depends on the relic density of stau.

3.1 Long lived stau

In this section, we show analytical calculation for the lifetime of the stau and numerical results of the lifetime [29]. The stau is a mass eigenstate consisting of superpartner pf left- and right-hand taus. The relation between a mass eigenstate and a gauge eigenstate is given as follows,

$$\begin{pmatrix} \tilde{\tau}_L \\ \tilde{\tau}_R \end{pmatrix} = \begin{pmatrix} \cos\theta_\tau & \sin\theta_\tau e^{i\gamma_\tau} \\ -\sin\theta_\tau e^{-i\gamma_\tau} & \cos\theta_\tau \end{pmatrix} \begin{pmatrix} \tilde{\tau}_1 \\ \tilde{\tau}_2 \end{pmatrix}, \tag{3-1-1}$$

where θ_τ is mixing angle, γ_τ is CP violating phase, and $\tilde{\tau}_{1(2)}$ is the lighter (heavier) stau. We represent the lighter stau as $\tilde{\tau}$ in this paper, and the stau is expressed by $\tilde{\tau}_L, \tilde{\tau}_R$ as follows,

$$\tilde{\tau} = \cos\theta_\tau \tilde{\tau}_L + \sin\theta_\tau e^{-i\gamma_\tau} \tilde{\tau}_R. \tag{3-1-2}$$

The decay modes of the stau governed by the mass difference between the stau and the neutralino, according to the kinematics. In this paper we interested in the small mass difference, we consider following four decay modes and show the diagrams in Fig.3.1.

$$\begin{aligned}
&\tilde{\tau} \to \tilde{\chi}_1^0 + \tau, \\
&\tilde{\tau} \to \tilde{\chi}_1^0 + \nu_\tau + \pi, \\
&\tilde{\tau} \to \tilde{\chi}_1^0 + \nu_\tau + l + \nu_l \quad (e, \mu \in l)
\end{aligned} \tag{3-1-3}$$

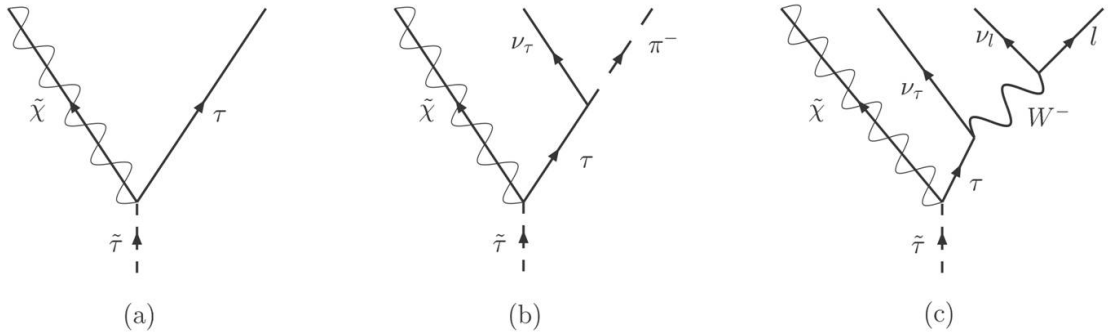

Figure 3.1: Feynmann diagrams of stau decay:(a)$\tilde{\tau} \to \tilde{\chi}_1^0\tau$, (b)$\tilde{\tau} \to \tilde{\chi}_1^0\nu_\tau\pi$, (c)$\tilde{\tau} \to \tilde{\chi}_1^0\nu_\tau l\nu_l$.

The interaction Lagrangian describing the stau decay is given by

$$\mathcal{L} = \tilde{\tau}^*\overline{\tilde{\chi}_1^0}(g_L P_L + g_R + P_R)\tau + \sqrt{2}G_{\rm F}\nu_\tau\gamma_\mu P_L\tau J^\mu + \frac{4G_{\rm F}}{\sqrt{2}}(\bar{l}\gamma^\mu P_L\nu_l)(\bar{\nu_\tau}\gamma_\mu P_L\tau) + h.c. \tag{3-1-4}$$

The first, second, and third terms describe decay mode of two, three, and four body, respectively. Here P_L and P_R are the projection operators, $G_{\rm F}$ is the Fermi constant, and g_L and g_R are the coupling constants given by

$$g_L = \frac{g}{\sqrt{2}\cos\theta_W}\sin\theta_W\cos\theta_\tau, \quad g_R = \frac{\sqrt{2}g}{\cos\theta_W}\sin\theta_W\sin\theta_\tau e^{i\gamma_\tau}, \tag{3-1-5}$$

where g is the weak coupling constant and $\theta_W$is the Weinberg angle. The expression of J^μ is given by

$$J^\mu = f_\pi\cos\theta_c p_\pi^\mu, \tag{3-1-6}$$

where $f_\pi \simeq 92.4$ GeV is the pion decay constant, $\theta_c \simeq 0.974$ is the Cabibbo angle, and p_π^μ is the four momentum of the pion.

Using the interaction Lagrangian, we obtain the decay rates for the two body as follows,

$$\begin{aligned}
\Gamma_{\text{2-body}} = &\frac{1}{16\pi m_{\tilde{\tau}}^3}(m_{\tilde{\tau}}^4 + m_{\tilde{\chi}_1^0}^4 + m_\tau^4 - 2m_{\tilde{\tau}}^2 m_{\tilde{\chi}_1^0}^2 - 2m_{\tilde{\tau}}^2 m_\tau^2 - 2m_{\tilde{\chi}_1^0}^2 m_\tau^2)^{1/2} \\
&\times \left\{(g_L^2 + |g_R|^2)(m_{\tilde{\tau}}^2 - m_{\tilde{\chi}_1^0}^2 - m_\tau^2) - 4\text{Re}[g_L g_R]m_\tau m_{\tilde{\chi}_1^0}\right\}.
\end{aligned} \tag{3-1-7}$$

For 3-body decay, the decay rate is given by

$$\begin{aligned}
\Gamma_{\text{3-body}} = &\frac{G_{\rm F}^2 f_\pi^2\cos\theta_c^2((\delta m)^2 - m_\pi^2)}{128\pi^3 m_{\tilde{\tau}}^3} \\
&\times \int_0^1 dx\sqrt{((\delta m)^2 - q_f^2)((\delta m + 2m_{\tilde{\chi}_1^0})^2 - q_f^2)}\frac{1}{(q_f^2 - m_\tau)^2 + (m_\tau\Gamma_\tau)^2}\frac{(q_f^2 - m_\pi^2)^2}{q_f^2} \\
&\times (q_f^2 - m_\pi^2)\left[(g_L^2 q_f^2 + |g_R|^2 m_\tau^2)((\delta m)^2 + 2m_{\tilde{\chi}_1^0}\delta m - q_f^2) - 4\text{Re}[g_L g_R]m_{\tilde{\chi}_1^0} m_\tau q_f\right].
\end{aligned} \tag{3-1-8}$$

Here q_f^2 is given by

$$q_f^2 = (\delta m)^2 - ((\delta m)^2 - m_f^2)x, \tag{3-1-9}$$

where the index $f \ni \pi, e, \mu$ denotes a massive particle, except for the neutralino, in the final state, $f = \pi$ in the three body decay. Γ_τ is the decay width.

In the 4-body decay processes, the decay rate is given by

$$\begin{aligned}\Gamma_{\text{4-body}} = & \frac{G_{\text{F}}^2((\delta m)^2 - m_l^2)}{24(2\pi)^5 m_{\tilde{\tau}}^3} \\ & \times \int_0^1 dx \sqrt{((\delta m)^2 - q_f^2)((\delta m + 2m_{\tilde{\chi}_1^0})^2 - q_f^2)} \frac{1}{(q_f^2 - m_\tau^2)^2 + (m_\tau \Gamma_\tau)^2} \frac{1}{q_f^4} \\ & \times \Big[\left\{ \frac{1}{4}(g_L^2 q_f^2 + |g_R^2| m_\tau^2)((\delta m)^2 + 2m_{\tilde{\chi}_1^0}\delta m - q_f^2) - \text{Re}[g_L g_R] m_{\tilde{\chi}_1^0} m_\tau q_f^2 \right\} \\ & \times \left\{ 12 m_l^4 q_f^4 \log\left[\frac{q_f^2}{m_l^2}\right] + (q_f^4 - m_l^4)(q_f^4 - 8m_l^2 q_f^2 + m_l^4) \right\} \Big],\end{aligned} \tag{3-1-10}$$

where $l = e, \mu$ and q_f^2 is given by Eq.(3-1-9).

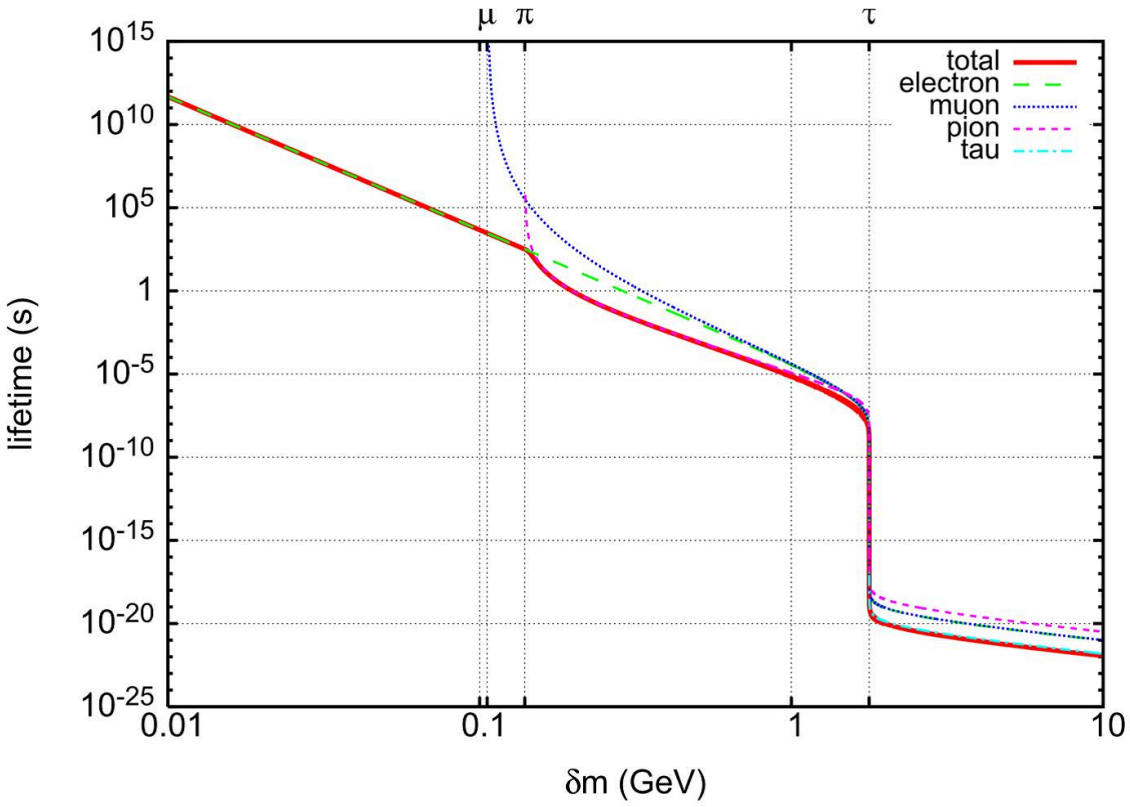

Figure 3.2: Total lifetime and partial lifetimes of each decay mode as a function of δm. The lines label electron, muon, pion, and tau correspond to the processes $\tilde{\tau} \to \tilde{\chi}_1^0 e \nu_\tau \bar{\nu}_e, \tilde{\tau} \to \tilde{\chi}_1^0 \mu \nu_\tau \bar{\nu}_\mu, \tilde{\tau} \to \tilde{\chi}_1^0 \nu_\tau \pi$, and $\tilde{\tau} \to \tau$, respectively. Here we take $m_{\tilde{\chi}_1^0} = 300$ GeV, $\theta_\tau = \pi/3$, and $\gamma_\tau = 0$.

We show the total lifetime and partial lifetimes of each decay mode of the stau as a function of δm. Here we take $m_{\tilde{\chi}_1^0} = 300$ GeV, $\theta_\tau = \pi/3$, and $\gamma_\tau = 0$. It is important to emphasize here that the lifetime is increases drastically with increasing δm. The 2-body decay is kinematically allowed in the region with $\delta m > m_\tau$, and the 2-body decay rate is lager than the 3/4 body decay rate. In the

region with $\delta m < m_\tau$, the 2-body decay is kinematically forbidden, and hence the stau must decay into mainly 3-body, $\tilde{\tau} \to \tilde{\chi}_1^0 \nu_\tau \pi$. Thus, a discontinuity is at $\delta m = m_\tau$ and the life time drastically increase in $\delta m < m_\tau$. At the $\delta m = m_\pi$ the lifetime increases slightly. This is due to the fact that the dominant mode changes from 3-body to 4-body decay. In contrast, the life time does not increase much at $\delta m = m_\mu$ even though the decay mode of $\tilde{\tau} \to \tilde{\chi}_1^0 \mu \nu_\tau \bar{\nu}_\mu$ is kinematically forbidden in $\delta m < m_\mu$. This is because the muon production processes is already kinematically suppressed and the electron production processes govern the stau decay.

Here we also point that the lifetime of the stau is larger than 10^3 seconds in the region with $\delta m < 0.1$ GeV. The values are important for stau-BBN scenario as we explained later.

3.2 Formation of stau-nucleus bound states

As we explain in sec.(3.1), the stau become long lived if the mass difference is smaller than the mass of tau lepton. In the case that the stau survives until the BBN era, the stau forms bound state with nucleus. Through the bound state, the stau induce exotic nuclear reactions.

In this section, we firstly review mechanism for formation of stau-nucleus bound state [34]. We show capture rate of stau for nucleus, universe temperature at which a bound state is formed. Next, we explain exotic nuclear reactions induced by the stau. We numerically estimate time scale of these reactions. taking into account of the time scales, we show the allowed region in parameter space of stau where calculated abundances of light element is consistent with the observed values.

3.2.1 Evaluation of binding energy

If the stau survive in BBN era, the stau forms bound state with nucleus. Assuming uniform charge distribution in side the light element, we review the calculation for binding energy of the bound state.

Hamiltonian for a stau and a nucleus is given as follows,

$$H = \begin{cases} \dfrac{p^2}{2m_X} - \dfrac{Z_X Z_c \alpha}{2r_X} + \dfrac{Z_X Z_c \alpha}{2r_X}\left(\dfrac{r}{r_X}\right)^2 & \text{for } (r < r_X), \\ \dfrac{p^2}{2m_X} - \dfrac{Z_X Z_c \alpha}{r} & \text{for } (r > r_X), \end{cases} \tag{3-2-1}$$

where α is the fine structure constant, $r_X \sim 1.2A^{1/3}/200\text{MeV}^{-1}$ is the nuclear radius, Z_X is the electric charge of the nucleus, and Z_c is the electric charge of the stau. A is the atomic number, and m_X is the mass of the nucleus X. Here we assumed $m_X \ll m_c \sim \mathcal{O}(100)$GeV, which means the reduced mass $1/\mu = 1/m_c + 1/m_X \sim 1/m_X$.

Given hamiltonian as eq.(3-2-1), the binding energy for the bound state is given as follows,

$$E_{\text{bin}} \simeq \begin{cases} \dfrac{1}{2} Z_X^2 Z_c^2 \alpha^2 m_X^2 & \text{for } 0 < Z_X Z_c \alpha m_X r_X < 1, \\ \dfrac{1}{r_X}\left(\dfrac{1}{m_X r_X} F(Z_X Z_c \alpha m_X r X)\right) & \text{for } 1 < Z_X Z_c \alpha m_X r_X < 2, \\ \dfrac{3}{2}\left[\dfrac{Z_X Z_c \alpha}{r_X} - \dfrac{1}{r_X}\left(\dfrac{Z_X Z_c \alpha}{m_X r_X}\right)\right] & \text{for } 2 < Z_X Z_c \alpha m_X r_X < \infty, \end{cases} \tag{3-2-2}$$

In this way, the expressions for the binding energy are different each others. This is because approximation used in calculation is different. For $0 < 0 < Z_X Z_c \alpha m_X r_X < 1$, the Coulomb model gives a good approximation. On the other hand, the harmonic oscillator approximation gives a better approximation for $2 < Z_X Z_c \alpha m_X r_X < \infty$. We see from the above equations that the binding energies depends on charge, radius of each nucleus, and the mass of nucleus.

Table.3.1 shows the nuclear radius, the nuclear mass excess, the nuclear mass, and the binding energy. The nuclear mass and mass excess are expressed by using atomic mass unit as follows,

$$m_X = Au + \Delta_X, \tag{3-2-3}$$

Table 3.1: parameters

X	Z_X	$r_X(\mathrm{fm/GeV^{-1}})$	$a_X(\mathrm{fm/GeV^{-1}})$	$\Delta_X(10^{-3}\mathrm{GeV})$	$m_X(\mathrm{GeV})$	$E_{\rm bin}(\mathrm{MeV})$
p	1	1.200/6.081	28.80/146.0	7.289	0.9388	0.025
d	1	1.512/7.662	14.41/73.04	13.14	1.876	0.050
t	1	1.731/8.772	9.625/48.78	14.95	2.809	0.075
^{3}He	2	1.731/8.772	4.813/24.39	14.93	2.809	0.270
^{4}He	2	1.905/9.654	3.626/18.38	2.425	3.728	0.311
^{6}He	2	2.181/11.05	2.412/12.22	17.59	5.607	0.597
^{6}Li	3	2.181/11.05	1.609/8.153	14.09	5.603	0.914
^{7}Li	3	2.296/11.64	1.379/6.989	14.91	6.535	0.952
^{7}Be	4	2.296/11.64	1.034/5.241	15.77	6.536	1.490
^{8}Be	4	2.400/12.16	0.9066/4.594	4.942	7.457	1.550

where A is the mass number. The Bohr radius of each nucleus is expressed as follows,

$$a_X = \frac{m_e}{Z m_{\rm red}} a_0. \tag{3-2-4}$$

Here m_e is the mass of electron, a_0 is the Bohr radius of the hydrogen, $a_0 = 0.52918 \times 10^{-10}$m.

3.2.2 Recombination Cross Section

We describe the equation for the recombination cross section from the free state to the 1S bound state. In this evaluation, we assume a hydrogen-type bound state through a dipole photon emission[82] and a point like particle for the captured light element. The cross section is expressed as follows,

$$\begin{aligned}\sigma_r v &= \frac{2^9\pi^2\alpha Z_X^2}{3}\frac{E_{\rm bin}}{m_X^3 v}\left(\frac{E_{\rm bin}}{E_{\rm bin}+\frac{1}{2}m_X v^2}\right)^2 \frac{\exp\left[-4\sqrt{\frac{2E_{\rm bin}}{m_X v^2}}\tan^{-1}\left(\sqrt{\frac{m_X v^2}{2E_{\rm bin}}}\right)\right]}{1-\exp\left[-2\pi\sqrt{\frac{2E_{\rm bin}}{m_X v^2}}\right]} \\ &\simeq \frac{2^9\pi^2\alpha Z_X^2}{3e^4}\frac{E_{\rm bin}}{m_X^3 v},\end{aligned} \tag{3-2-5}$$

where v is the relative velocity of a stau and a nucleus. Note that we have $m_X v^2/2 \simeq 3T/2 \gg E_{\rm bin}$ for NR particles in kinetic equilibrium. Here we use the Coulomb model (hydrogen type) to evaluate the capture rate, where the binding energy $E_{\rm bin} = \alpha^2 Z_C^2 Z_X^2 m_X/2$ and the Bohr radius $r_B^{-1} \simeq \alpha Z_C Z_X m_X$.

The thermal-averaged cross section is written as

$$\begin{aligned}\langle\sigma_r v\rangle &= \frac{1}{n_1 n_2}\left(\frac{g}{(2\pi)^3}\right)^2 \int d^3p1 d^3p_2 \exp\left[-\frac{E_1+E_2}{T}\right]\sigma_r v \\ &= \frac{1}{n_G n_r}\left(\frac{g}{(2\pi)^3}\right)^2 \int d^3p_G \exp\left[-\frac{m_G}{T}\right]\exp\left[-\frac{p_G^2}{2m_G T}\right]\int d^3p_r^3 \sigma_r v \exp\left[-\frac{p_r^2}{2\mu T}\right] \\ &= \frac{2^9\pi\alpha Z_X^2\sqrt{2\pi}}{3e^4}\frac{E_{\rm bin}}{m_X^2\sqrt{m_X T}},\end{aligned} \tag{3-2-6}$$

where $m_G = m_1 + m_2$ and $\mu = m_X m_C/(m_X + m_C) \simeq m_X$ with

$$\begin{aligned} n_G &= \frac{g}{(2\pi)^3}\int d^3p_G \exp\left[-\frac{m_G}{T}\right]\exp\left[-\frac{p_G^2}{2m_G T}\right], \\ n_r &= \frac{g}{(2\pi)^3}\int d^3p_r \exp\left[-\frac{p_r^2}{2\mu T}\right]. \end{aligned} \tag{3-2-7}$$

Here we have assumed that only one stau is captured by a nucleus. Since the photon emission from a stau is suppressed, the recombination cross section for the further capture of an additional stau by the bound state would be much smaller. Therefore, as a first step, it would reasonable to ignore the multiple capture of staus by a nucleus.

3.2.3 Boltzmann equations

We firstly consider the case in which the kinetic and chemical equilibrium between the staus and the nuclei are not established. Here we must solve the Boltzmann equations for the staus, a nucleus and a bound states to obtain the number density. For staus,

$$\frac{\partial}{\partial t}n_C + 3Hn_C = \left[\frac{\partial}{\partial t}n_C\right]_{\rm capture}, \tag{3-2-8}$$

where H is the Hubble expansion rate. For a nucleus,

$$\frac{\partial}{\partial t}n_X + 3Hn_X = \left[\frac{\partial}{\partial t}n_X\right]_{\rm fusion} + \left[\frac{\partial}{\partial t}n_X\right]_{\rm capture}. \tag{3-2-9}$$

For the bound state,

$$\frac{\partial}{\partial t}n_{(C,X)} + 3Hn_{(C,X)} = \left[\frac{\partial}{\partial t}n_{(C,X)}\right]_{\rm fusion} - \left[\frac{\partial}{\partial t}n_C\right]_{\rm capture}. \tag{3-2-10}$$

By using the detailed balance relation between the forward process $X + C \to \gamma + (X, C)$ an the reverse process $\gamma + (X, C) \to X + C$, the capture reaction may be written by

$$\left[\frac{\partial}{\partial t}n_X\right]_{\rm capture} = \left[\frac{\partial}{\partial t}n_C\right]_{\rm capture} \simeq -\langle\sigma_r v\rangle[n_C n_X - n_{C,X}n_\gamma(E > E_{\rm bin})], \tag{3-2-11}$$

where

$$n_\gamma(E > E_{\rm bin}) \equiv n_\gamma \frac{\pi^2}{2\zeta(3)}\left(\frac{m_X}{2\pi T}\right)^{3/2}\exp[-\frac{E_{\rm bin}}{T}], \tag{3-2-12}$$

and

$$n_\gamma = \frac{2\zeta(3)}{\pi^2}T^3. \tag{3-2-13}$$

For a light element, if $\langle\sigma_r v\rangle n_C/H \ll 1$ is satisfied and the kinetic equilibrium is well established, we can get the Saha equation by requiring an equilibrium condition $\left[\frac{\partial}{\partial t}n_X\right]_{\rm capture} = 0$ in this equation.

When the temperature is higher than the binding energy of light nucleus, the destruction rate of the bound states by scatterings off the thermal photons with $E > E_{\rm bin}$ is rapid. Then only a small fraction of bound states can be formed, $n_{(C,X)} \sim n_C n_X/n_\gamma(E > E_{\rm bin}) \gg n_X$. Once the temperature becomes lower than the binding energy, the capture starts, and the bound state becomes stable if the other destruction processes among the nuclei are inefficient. The critical temperature at which the capture becomes efficient is estimated as follows. In the case of $n_X > n_C$, taking $n_C \sim n_{(C,X)}$, we get a relation

$$\left(\frac{m_X}{T}\right)^{3/2}\exp\left[-\frac{E_{\rm bin}}{T}\right] \sim \frac{n_X}{n_\gamma} = \mathcal{O}(10^{-10}). \tag{3-2-14}$$

On the other hand, in the case of $n_X < n_C$, taking $n_X \sim n_{(C,X)}$, we have

$$\left(\frac{m_X}{T}\right)^{3/2}\exp\left[-\frac{E_{\rm bin}}{T}\right] \sim \frac{n_C}{n_\gamma} \sim \mathcal{O}(10^{-10})\left(\frac{100{\rm GeV}}{m_C}\right)\left(\frac{\Omega_C}{0.23}\right), \tag{3-2-15}$$

where Ω_C is the abundance of the stau.

This analysis shows that the critical temperature is approximately

$$T_c \simeq \frac{E_{\rm bin}}{40}. \tag{3-2-16}$$

The number density of the bound state is calculated by solving the Boltzmann equations. Figure.3.3 shows the evolution of the bound ratios of ^{4}He,^{7} Li and ^{7}Be as a function of the universe temperature of T [45]. Here we defined the bound ratio as $n_{(\tilde{\tau},X)}/n_X$. The value of $Y_{\tilde{\tau},\rm BF}$ is the yield value of staus at the time of *the formation of the bound state* with nuclei $t_{\rm BF}$. The value of $Y_{\tilde{\tau},\rm BF}$ is expressed by the yield value of the stau at the *freeze-out* time and the lifetime of the stau as follows,

$$Y_{\tilde{\tau},\rm BF} = Y_{\tilde{\tau},\rm FO} \exp\left[-\frac{t_{\rm BF}}{\tau_{\tilde{\tau}}}\right], \tag{3-2-17}$$

where $\tau_{\tilde{\tau}}$ is the lifetime of the stau.

We see from this figure that the critical temperature is different in case of ^{4}He, ^{7}Li, and ^{7}Be. We estimate the critical temperature by using eq.(3-2-16) and Tab.3.1 as follows,

$$\begin{aligned} T_c|_{\rm He} &\simeq \frac{E_{\rm bin}|_{\rm He}}{40} = 7.8{\rm keV}, \\ T_c|_{\rm Li} &\simeq \frac{E_{\rm bin}|_{\rm Li}}{40} = 23.8{\rm keV}, \\ T_c|_{\rm Be} &\simeq \frac{E_{\rm bin}|_{\rm Be}}{40} = 37.3{\rm keV}, \end{aligned} \tag{3-2-18}$$

and these values mainly depend on the charge number of nucleus.

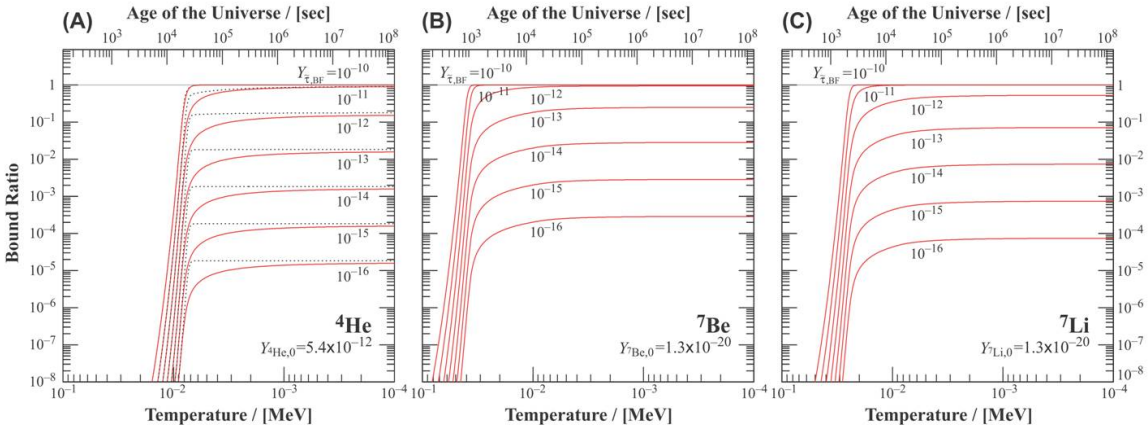

Figure 3.3: Evolution of the bound ratio of the nuclei ^{4}He,^{7} Be, and ^{7}Li. We vary the abundance of the stau at the time of the formation of the bound state from 10^{-10} to 10^{-16} in each figure. In Fig.3.3(a), we also plotted lines corresponding curves predicted using the Saha equation for reference [45].

3.3 Exotic Nuclear Reactions

We explain exotic nuclear reactions induced by the long lived stau. We take into account following three reactions;

- Stau-Catalyzed Fusion Reaction [33, 37],
- Internal Conversion Reaction [40],

- ^{4}He Spallation Reactions [58].

In following subsections, we show how to calculate timescale of these reactions in details.

3.3.1 Stau-Catalayzed Fusion

Lithium 6 is produced by following reactions in Standard BBN scenario,

$$^4\mathrm{He} + \mathrm{d} \rightarrow^6 \mathrm{Li} + \gamma. \tag{3-3-1}$$

The reaction rate is smaller than those of reactions producing other light elements.

If the stau has sufficient lifetime to survive the BBN era, the stau makes bound state with ^{4}He and then reacts with d as follows,

$$(\tilde{\tau}^4\mathrm{He}) + \mathrm{d} \rightarrow^6 \mathrm{Li} + \gamma. \tag{3-3-2}$$

Here the stau act as catalyst and enhance the reaction rate about six times larger than that of Eq.(3-3-1). The cross section of the reaction Eq.(3-3-2) is expressed as follows,

$$\mathrm{N_A}\langle\sigma_{\mathrm{CF}}v\rangle = 2.37\times10^8\times(1-0.34\mathrm{T_9})\mathrm{T_9}^{-\frac{2}{3}}\exp\left(-5.33\mathrm{T_9}^{-\frac{1}{3}}\right) \quad [\mathrm{cm^3 s^{-1} mol}], \tag{3-3-3}$$

where $\mathrm{N_A}$ is the Avogadro constant and $\mathrm{T_9}$ is dimensionless quantity defined as follows,

$$\mathrm{T_9} = \frac{\mathrm{T}}{10^9\mathrm{K}}. \tag{3-3-4}$$

3.3.2 Internal Conversions

When a stau forms a bound state with a nucleus, the bound state decays through as follows,

$$\begin{aligned}\tilde{\tau} + {}^7\mathrm{Be} &\rightarrow (\tilde{\tau}{}^7\mathrm{Be}) \rightarrow \tilde{\chi}_1^0 + \nu_\tau + {}^7\mathrm{Li},\\ \tilde{\tau} + {}^7\mathrm{Li} &\rightarrow (\tilde{\tau}{}^7\mathrm{Li}) \rightarrow \tilde{\chi}_1^0 + \nu_\tau + {}^7\mathrm{He}.\end{aligned} \tag{3-3-5}$$

Fig.(3.3.2) show these reactions.

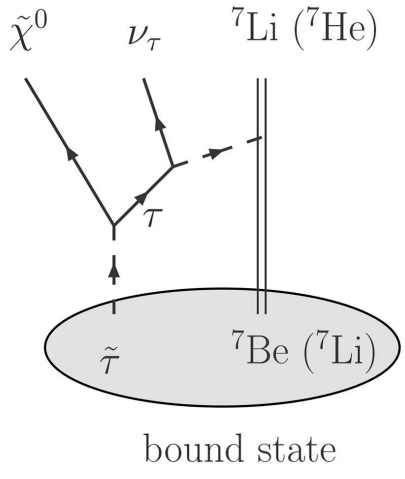

Figure 3.4: The Feynmann diagrams of internal conversion of ^{7}Be (^{7}Li).

After these reactions, ^{7}Li and ^{7} He are broken to another particles due to a reaction with back ground particles.

The reaction rates of Eqs. (3-3-5) is given by

$$\Gamma_{\rm IC} = |\Psi|^2 \sigma_{\rm IC} v, \tag{3-3-6}$$

where $|\psi|^2$ expresses the overlap of the wave function between a stau and a nucleus. When we assume that the bound state is in S-state of hydrogen-like atom, the overlap of the wave function is expressed as follows,

$$|\psi|^2 = \frac{1}{\pi r_X^3}, \tag{3-3-7}$$

where r_X is a nuclear radius and $\sigma_{\rm IC} v$ is a cross section of the reactions. The cross secton is fiven by

$$\begin{aligned}\sigma_{\rm IC} v = \frac{1}{2E_{\tilde\tau} 2E{\rm Be}} \int d{\rm LIPS} |\langle \overline{\tilde\chi_1^0} \nu_\tau^7{\rm Li} | \mathcal{L}_{\rm int} | \tilde\tau^7{\rm Be}\rangle|^2 \\ \times (2\pi)^4 \delta^{(4)}(p_{\tilde\tau} + p_{\rm Be} - p_{\tilde\chi_1^0} - p_{\nu_\tau} - p_{\rm Li}).\end{aligned} \tag{3-3-8}$$

where

$$d{\rm LIPS} = \prod_i \frac{d^3 p_i}{(2\pi)^3 2E_i} \tag{3-3-9}$$

, and $i \in \tilde\chi_1^0, \nu_\tau, ^7$ Li in the case.

We calculate the reaction rates of Eqs. (3-3-5) by using the Lagrangian in Eq. (3-1-4). The squared amplitude in the Eq. (3-3-8) is expressed as follows

$$\langle \tilde\chi_1^0 \nu_\tau^7{\rm Li} | \mathcal{L}_{\rm int} | \tilde\tau^7{\rm Be}\rangle = \langle ^7{\rm Li} | J_\mu | ^7{\rm Be}\rangle \langle \tilde\chi_1^0 \nu_\tau | \tilde\tau^* \overline{\tilde\chi_1^0} (g_L P_L + g_R P_R)\tau \times \sqrt{2} G_{\rm F} \nu_\tau \gamma^\mu P_L \tau | \tilde\tau\rangle. \tag{3-3-10}$$

Here the matrix element of the hadronic part is given by

$$|\langle ^7{\rm Li} | J_\mu | ^7{\rm Be}\rangle|^2 = \frac{(1+3g_A^2) 16\pi^3 E_{\rm Be} E_{\rm Li} {\rm log}_{10} 2}{m_e^5 G_{\rm F}^2} \frac{1}{\rm ft}, \tag{3-3-11}$$

where we fixes ft $= 10^{3.3}$ sec. In thsi equation, we approximately calculate only temr of $\mu = 0$ and we omit other terms. Then we calculate the matrix element of the leptonic part as follows

$$\langle \tilde\chi_1^0 \nu_\tau | \tilde\tau^* \overline{\tilde\chi_1^0} (g_L P_L + g_R P_R)\tau \times \sqrt{2} G_{\rm F} \nu_\tau \gamma^\mu P_L \tau | \tilde\tau\rangle = \frac{4 m_{\tilde\chi_1^0} G_{\rm F}^2 |g_R|^2 E_{\nu_\tau}}{m_\tau^2}. \tag{3-3-12}$$

We calculate the cross section of the reactions by using these equations as follows,

$$\begin{aligned}\sigma_{\rm IC} v &= \frac{(1+3g_A^2) 2 |g_R|^2 {\rm log}_{10} 2}{105} \frac{p_{\rm Max}^7}{m_{\tilde\tau} m_\tau^2 m_{\rm Li}^2 m_e^5} \frac{1}{\rm ft}, \\ p_{\rm Max} &= \sqrt{2 m_{\rm Li} (m_{\tilde\tau} - m_{\tilde\chi_1^0} + m_{\rm Be} - m_{\rm Li} - E_{{\rm bin;Be}})}\end{aligned} \tag{3-3-13}$$

These reactions occur more efficiently than standard nuclear reactions due to two reasons: i) the overlap of the wave functions of the two becomes large since the stau and particle are packed in the small space, ii) the small difference between the two allows virtual exchange of the hadronic current even if $\delta m < m_\pi$.

We show the timescales of internal conversion processes as the function of δ m in Fig.(3.5). We see from the figure that the timescales in $\delta m \sim 1.0(0.1)$ GeV is about $10^{-6}(10^{-3})$ sec. Meanwhile the timescales of forming bound state between the stau and ^{7}Li/^{7}Be are about 10^3 sec. From the fact we see that the bound state is broken to other state soon after forming.

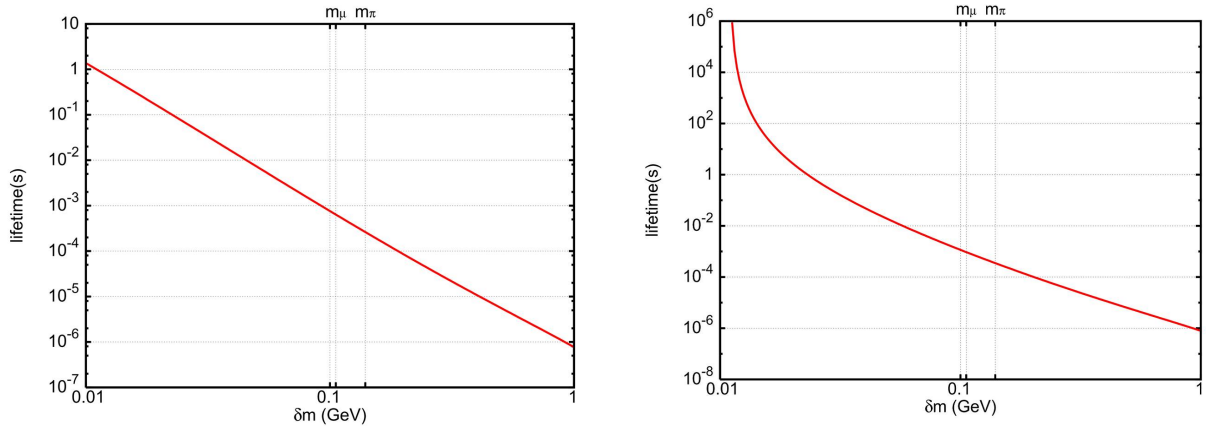

Figure 3.5: The timescales of internal conversion processes as the function of δ m. Left pane;: $(\tilde{\tau}^7\mathrm{Be}) \to \tilde{\chi}_1^0 + \nu_\tau + {}^7\mathrm{Li}$, right panel:$(\tilde{\tau}^7\mathrm{Li}) \to \tilde{\chi}_1^0 + \nu_\tau + {}^7\mathrm{He}$. We take $m_{\tilde{\chi}_1^0} = 300\mathrm{GeV}$, $\theta_\tau = \pi/3$, and $\gamma_\tau = 0$ in both figures.

3.3.3 ^{4}He Spallation Reactions

The exotic nuclear reaction through the bound state between stau-^{4}He is not only the ^{6}Li catalyzed fusion reaction. The bound state, $(\tilde{\tau}^4\mathrm{He})$, is also broken to other states as follows,

$$(\tilde{\tau}^4\mathrm{He}) \to \tilde{\chi}_1^0 + \nu_\tau + \mathrm{t} + \mathrm{n}, \tag{3-3-14a}$$
$$(\tilde{\tau}^4\mathrm{He}) \to \tilde{\chi}_1^0 + \nu_\tau + \mathrm{d} + \mathrm{n} + \mathrm{n}, \tag{3-3-14b}$$
$$(\tilde{\tau}^4\mathrm{He}) \to \tilde{\chi}_1^0 + \nu_\tau + \mathrm{p} + \mathrm{n} + \mathrm{n} + \mathrm{n}. \tag{3-3-14c}$$

These reactions are expressed as Fig. 3.6. The reaction rates of Eq. (3-3-14) are calculated from

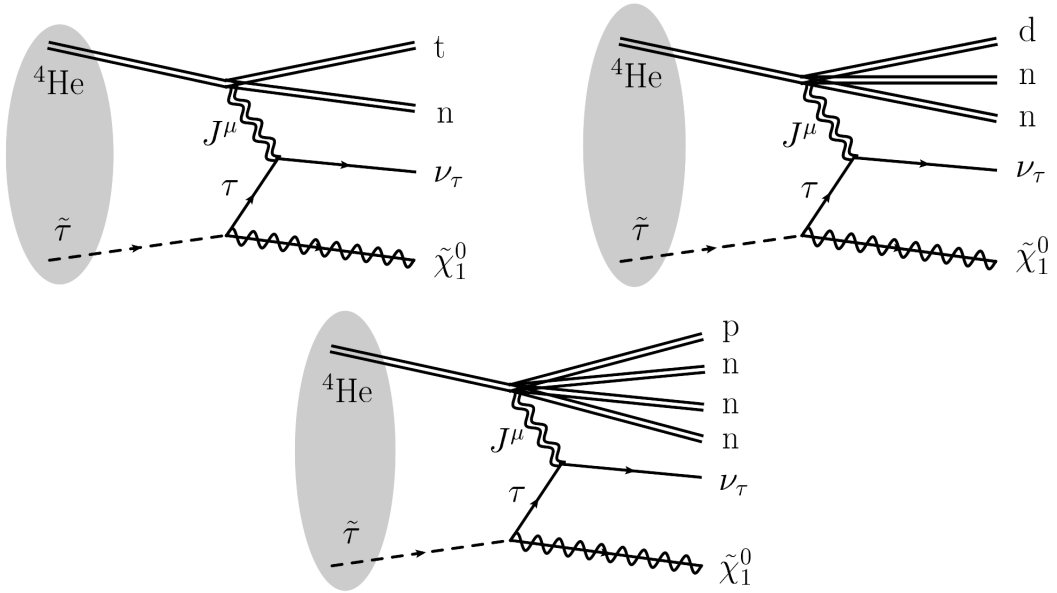

Figure 3.6: The spallation processes of ^{4}He induced by the long-lived stau.

the Lagrangian in Eq. (3-1-4).

$(\tilde{\tau}^4\mathbf{He}) \to \tilde{\chi}_1^0 + \nu_\tau + \mathbf{t} + \mathbf{n}$

First we consider the process Eq. (3-3-14a). The rate of this process is expressed as

$$\Gamma_{\rm tn} = \frac{1}{\tau_{\rm tn}} = |\psi|^2 \sigma_{\rm tn} v \tag{3-3-15}$$

where $|\psi|^2$ stands for the overlap of the wave functions of the stau and the ^{4}He nucleus, and $\tau_{\rm tn}$ is the timescale of this reaction. We estimate the overlap by

$$|\psi|^2 = \frac{(Z\alpha m_{\rm He})^3}{\pi} \tag{3-3-16}$$

where Z and $m_{\rm He}$ represent the atomic number and the mass of ^{4}He, respectively, and α is the fine structure constant. We assumed that the stau is pointlike particle and is much heavier than ^{4}He nucleus so that the reduced mass of the bound state is equal to the mass of ^{4}He nucleus itself. The cross section of the elementary process for this reaction is denoted by $sigma_{\rm tn}v$ and calculated as

$$\begin{aligned}
\sigma_{\rm tn} v &\equiv \sigma v((\tilde{\tau}^4{\rm He}) \to \tilde{\chi}_1^0 \nu_\tau {\rm tn}) \\
&= \frac{1}{2E_{\tilde{\tau}}} \int \frac{d^3\boldsymbol{p}_\nu}{(2\pi)^3 2E_\nu} \frac{d^3\boldsymbol{p}_{\tilde{\chi}_1^0}}{(2\pi)^3 2E_{\tilde{\chi}_1^0}} \frac{d^3\boldsymbol{q}_{\rm n}}{(2\pi)^3} \frac{d^3\boldsymbol{q}_{\rm t}}{(2\pi)^3} \\
&\times |\mathcal{M}((\tilde{\tau}^4{\rm He}) \to \tilde{\chi}_1^0 \nu_\tau {\rm tn})|^2 \\
&\times (2\pi)^4 \delta^{(4)}(p_{\tilde{\tau}} + p_{\rm He} - p_\nu - q_{\rm t} - q_{\rm n}).
\end{aligned} \tag{3-3-17}$$

Here p_i and E_i are the momentum and the energy of the particle species i, respectively.

We briefly show the calculation of the amplitude of this process. The amplitude is deconstructed as

$$\begin{aligned}
\mathcal{M}((\tilde{\tau}^4{\rm He}) \to \tilde{\chi}_1^0 \nu_\tau {\rm tn}) &= \langle {\rm tn} \tilde{\chi}_1^0 \nu_\tau | \mathcal{L}_{\rm int} | {}^4{\rm He} \tilde{\tau} \rangle \\
&= \langle {\rm tn} | J^\mu | {}^4{\rm He} \rangle \langle \tilde{\chi}_1^0 \nu_\tau | j_\mu | \tilde{\tau} \rangle.
\end{aligned} \tag{3-3-18}$$

Here we omitted the delta function for the momentum conservation and the spatial integral . The weak current J_μ consists of a vector current V_μ and an axial vector current A_μ as $J_\mu = V_\mu + g_{\rm A} A_\mu$, where $g_{\rm A}$ is the axial coupling constant. The relevant components of the currents in this reaction are V^0 and A^i $(i = 1, 2, 3)$. We take these operators as a sum of a single-nucleon operators as

$$V^0 = \sum_{a=1}^{4} \tau_a^- e^{i\boldsymbol{q}\cdot\boldsymbol{r}_a}, \quad A^i = \sum_{a=1}^{4} \tau_a^- \sigma_a^i e^{i\boldsymbol{q}\cdot\boldsymbol{r}_a}, \tag{3-3-19}$$

where $\boldsymbol{q}$ is the momentum carried by the current, $\boldsymbol{r}_a$ is the spatial coordinate of the $a-$th nucleon ($a \in \{1, 2, 3, 4\}$), and τ_a^- and σ_a^i denote the isospin ladder operator and the spin operator of the $a-$th nucleon, respectively. Each component leads to a part of hadronic matrix element:

$$ {\rm tn}\langle {\rm tn} | V^0 | {}^4{\rm He} \rangle = \sqrt{2} \mathcal{M}_{\rm tn}, \tag{3-3-20}$$

$$\langle {\rm tn} | g_{\rm A} A^+ | {}^4{\rm He} \rangle = \sqrt{2} g_{\rm A} \mathcal{M}_{\rm tn}, \tag{3-3-21}$$

$$\langle {\rm tn} | g_{\rm A} A^+ | {}^4{\rm He} \rangle = -\sqrt{2} g_{\rm A} \mathcal{M}_{\rm tn}, \tag{3-3-22}$$

$$\langle {\rm tn} | g_{\rm A} A^3 | {}^4{\rm He} \rangle = -\sqrt{2} g_{\rm A} \mathcal{M}_{\rm tn}, \tag{3-3-23}$$

where $A^\pm = (A^1 \pm iA^2)/\sqrt{2}$. Given the relevant wave functions of a ^{4}He nucleus, a triton, and a neutron, we obtain the hadronic matrix element as

$$\mathcal{M}_{\rm tn} = \left(\frac{128\pi}{3} \frac{a_{\rm He} a_{\rm t}^2}{(a_{\rm He} + a_{\rm t})^4} \right)^{3/4} \left\{ \exp\left[-\frac{\boldsymbol{q}_{\rm t}^2}{3a_{\rm He}} \right] - \exp\left[-\frac{\boldsymbol{q}_{\rm n}^2}{3a_{\rm He}} - \frac{(\boldsymbol{q}_{\rm t} + \boldsymbol{q}_{\rm n})^2}{6(a_{\rm He} + a_{\rm t})} \right] \right\} \tag{3-3-24}$$

Table 3.2: Input values of the matter radius $R_{\rm mat}$ for d, t, and ^{4}He, the magnetic radius $R_{\rm mag}$ for p and n, nucleus mass m_X, excess energy Δ_X for the nucleus X, and each reference.

nucleus	$R_{\rm mat(mag)}$ [fm]/[GeV^{-1}]	m_X [GeV]	Δ_X [GeV]
p	0.876 / 4.439 [83]	0.9383 [88]	6.778×10^{-3} [89]
n	0.873 / 4.424 [84]	0.9396 [88]	8.071×10^{-3} [89]
d	1.966 / 9.962 [85]	1.876 [89]	1.314×10^{-2} [89]
t	1.928 / 9.770 [86]	2.809 [89]	1.495×10^{-2} [89]
^{4}He	1.49 / 7.55 [87]	3.728 [89]	2.425×10^{-3} [89]

Here $\boldsymbol{q}_{\rm t}$ and $\boldsymbol{q}_{\rm n}$ are three-momenta of the triton and the neutron, respectively, and $a_{\rm He}$ and $a_{\rm t}$ are related to the mean square matter radius $R_{\rm mat}$ by

$$a_{\rm He}=\frac{9}{16}\frac{1}{(R_{\rm mat})^2_{\rm He}},\quad a_{\rm t}=\frac{1}{2}\frac{1}{(R_{\rm mat})^2_{\rm t}}. \tag{3-3-25}$$

We list in Tab. 3.2 input values of the matter radius for the numerical calculation in this article. The remaining part is straightforwardly calculated to be

$$|\langle\tilde{\chi}^0_1\nu_\tau|j_0|\tilde{\tau}\rangle|^2=|\langle\tilde{\chi}^0_1\nu_\tau|j_z|\tilde{\tau}\rangle|^2=4G_{\rm F}^2|g_{\rm R}|^2\frac{m_{\tilde{\chi}^0_1}E_\nu}{m_\tau^2}, \tag{3-3-26}$$

$$|\langle\tilde{\chi}^0_1\nu_\tau|j_\pm|\tilde{\tau}\rangle|^2=4G_{\rm F}^2|g_{\rm R}|^2\frac{m_{\tilde{\chi}^0_1}E_\nu}{m_\tau^2}\left(1\mp\frac{p^z_\nu}{E_\nu}\right), \tag{3-3-27}$$

where E_ν and p^z_ν are the energy and $z-$component of the momentum of the tau neutrino, respectively. We assumed that the stau and the neutralino are non-relativistic. This equation includes not only all the couplings such as $G_{\rm F}$, $g_{\rm L}$, and $g_{\rm R}$, but also the effect of the virtual tau propagation in the Fig. 3.6. Note here that $g_{\rm L}$ coupling does not contribute. This is because the virtual tau ought to be left-handed at the weak current, and it flips its chirality during the propagation since the transferred momentum is much less than its mass.

Combining hadronic part with the other part, we obtain the squared amplitude as

$$|\mathcal{M}((\tilde{\tau}^4{\rm He})\to\tilde{\chi}^0_1\nu_\tau{\rm tn})|^2=\frac{8m_{\tilde{\chi}^0_1}G_{\rm F}^2|g_{\rm R}|^2}{m_\tau^2}(1+3g_{\rm A}^2)\mathcal{M}^2_{\rm tn}E_\nu \tag{3-3-28}$$

Integrating on the phase of the final states, we obtain the cross section as

$$\begin{aligned}\sigma_{\rm tn}v=&\frac{8}{\pi^2}\left(\frac{32}{3\pi}\right)^{3/2}g^2\tan^2\theta_W\sin^2\theta_\tau(1+3g_A^2)G_{\rm F}^2\\&\times\Delta^4_{\rm tn}\frac{m_{\rm t}m_{\rm n}}{m_{\tilde{\tau}}m_\tau^2}\frac{a_{\rm He}^{3/2}a_{\rm t}^3}{(a_{\rm He}+a_{\rm t})^5}I_{\rm tn},\end{aligned} \tag{3-3-29}$$

$$\begin{aligned}I_{\rm tn}=&12\int_0^1 ds\int_0^{\sqrt{1-s^2}}dt(1-s^2-t^2)^2st\\&\times\left\{\frac{1}{6}\frac{k_{\rm t}k_{\rm n}}{a_{\rm He}+a_{\rm t}}st\exp\left[-\frac{2}{3}\frac{k_{\rm t}^2}{a_{\rm He}}t^2\right]+\frac{1}{4}\exp\left[-\frac{2}{3}\frac{k_{\rm n}^2}{a_{\rm He}}s^2-\frac{1}{3}\frac{k_{\rm n}^2s^2+k_{\rm t}^2t^2}{a_{\rm He}+a_{\rm t}}\right]\sinh\left[\frac{2}{3}\frac{k_{\rm t}k_{\rm n}}{a_{\rm He}+a_{\rm t}}st\right]\right.\\&\left.-\exp\left[-\frac{1}{3}\frac{k_{\rm n}^2s^2+k_{\rm t}^2t^2}{a_{\rm He}}-\frac{1}{6}\frac{k_{\rm n}^2s^2+k_{\rm t}^2t^2}{a_{\rm He}+a_{\rm t}}\right]\sinh\left[\frac{1}{3}\frac{k_{\rm t}k_{\rm n}}{a_{\rm He}+a_{\rm t}}st\right]\right\}\end{aligned} \tag{3-3-30}$$

Here $\Delta_{\rm tn}, k_{\rm t}$, and $k_{\rm n}$ are defined as

$$\Delta_{\rm tn} \equiv \delta m + \Delta_{\rm He} - \Delta_{\rm t} - \Delta_{\rm n} - E_{\rm b}, \tag{3-3-31}$$

$$k_{\rm t} =\equiv \sqrt{2m_{\rm t}\Delta_{\rm tn}}, \tag{3-3-32}$$

$$k_{\rm n} =\equiv \sqrt{2m_{\rm n}\Delta_{\rm tn}} \tag{3-3-33}$$

where Δ_X is the excess energy of the nucleus X, and $E_{\rm b}$ is the binding energy of $(\tilde{\tau}^4{\rm He})$ system.

$(\tilde{\tau}^4\mathbf{He}) \to \tilde{\chi}_1^0 + \nu_\tau + \mathbf{d} + \mathbf{n} + \mathbf{n}$

The rate of another spallation process of Eq. (3-3-14b) is similarly calculated. The cross section is calculated to be

$$\sigma v_{\rm dnn} = \frac{192}{\pi^4} g^2 \tan^2\theta_{\rm W} \sin^2\theta_\tau G_{\rm F}^2 \Delta_{\rm dnn}^4 \frac{m_{\rm n} m_{\rm d}}{m_{\tilde{\tau}} m_\tau^2} \left(\frac{2a_{\rm d}}{a_{\rm He}(a_{\rm d}+a_{\rm He})^2}\right)^{3/2} I_{\rm dnn}, \tag{3-3-34}$$

where

$$\begin{aligned}
I_{\rm dnn} &= \int_0^1 ds \int_0^{\sqrt{1-s^2}} dt \int_0^{\sqrt{1-s^2-t^2}} du (1-s^2-t^2-u^2)^2 \\
&\times \Big\{ (1+3g_A^2) a_{\rm He} k_{\rm n}^3 s t^2 u \exp\left[-\frac{3k_{\rm d}^2 s^2 + 4k_{\rm n}^2 u^2}{4a_{\rm He}}\right] \sinh\left[\frac{k_{\rm n} k_{\rm d}}{a_{\rm He}} su\right] \\
&- \sqrt{2}(1+g_A^2) a_{\rm He} k_{\rm n}^3 s t u^2 \exp\left[-\frac{3k_{\rm d}^2 s^2 + 2k_{\rm n}^2 t^2 + 2k_{\rm n}^2 u^2}{4a_{\rm He}}\right] \sinh\left[\frac{1}{\sqrt{2}} \frac{k_{\rm n} k_{\rm d}}{a_{\rm He}} st\right] \\
&+ 2\sqrt{2} g_{\rm A}^2 (a_{\rm He} + a_{\rm d}) k_{\rm n}^3 s t u^2 \exp\left[-\frac{k_{\rm n}^2(2t^2+u^2)}{2a_{\rm He}} - \frac{k_{\rm d}^2 s^2 + 2k_{\rm n}^2 t^2}{4(a_{\rm He}+a_{\rm d})}\right] \sinh\left[\frac{1}{\sqrt{2}} \frac{k_{\rm d} k_{\rm n}}{a_{\rm He}+a_{\rm d}} st\right] \\
&- 16\sqrt{2} g_A^2 \frac{a_{\rm He}^2}{a_{\rm He}+a_{\rm d}} \sqrt{5a_{\rm He}^2 + 6a_{\rm He}a_{\rm d} + 2a_{\rm d}^2}\, k_{\rm n} s u \\
&\quad \times \exp(-A_1 k_{\rm d}^2 s^2 - A_2 k_{\rm n}^2 t^2 - A_3 k_{\rm n}^2 u^2) \sinh(A_4 k_{\rm d} k_{\rm n} s t) \sinh(A_5 k_{\rm n}^2 t u) \Big\}
\end{aligned} \tag{3-3-35}$$

Here $\Delta_{\rm dnn}, k_{\rm d}, k_{\rm n}$ and $A_i (i = 1-5)$ are defined as follows:

$$\begin{aligned}
\Delta_{\rm dnn} &\equiv \delta m + \Delta_{\rm He} - \Delta_{\rm d} - 2\Delta_{\rm n} - E_{\rm b}, \\
k_{\rm n} &\equiv \sqrt{2m_{\rm n}\Delta_{\rm dnn}}, \\
k_{\rm d} &\equiv \sqrt{2m_{\rm d}\Delta_{\rm dnn}}, \\
A_1 &\equiv \frac{4a_{\rm He}+3a_{\rm d}}{8a_{\rm He}(a_{\rm He}a_{\rm d})}, \\
A_2 &\equiv \frac{22a_{\rm He}^3 + 44a_{\rm He}^2 a_{\rm d} + 30 a_{\rm He} a_{\rm d}^2 + 7a_{\rm d}^3}{4a_{\rm He}(a_{\rm He}+a_{\rm d})(5a_{\rm He}^2 + a_{\rm He}a_{\rm d} + 2a_{\rm d}^2)}, \\
A_3 &\equiv \frac{8a_{\rm He}^2 + 9a_{\rm He}a_{\rm d} + 3a_{\rm d}^2}{4a_{\rm He}(5a_{\rm He}^2 + a_{\rm He}a_{\rm d} + 2a_{\rm d}^2)}, \\
A_4 &\equiv \frac{1}{4a_{\rm He}(a_{\rm He}+a_{\rm d})} \sqrt{10a_{\rm He}^2 + 12a_{\rm He}a_{\rm d} + 4a_{\rm d}^2}, \\
A_5 &\equiv \frac{(a_{\rm He}+a_{\rm d})^2}{2a_{\rm He}(5a_{\rm He}^2 + 6a_{\rm He}a_{\rm d} + 2a_{\rm d}^2)}.
\end{aligned} \tag{3-3-36}$$

$(\tilde{\tau}^4\mathbf{He}) \to \tilde{\chi}_1^0 + \nu_\tau + \mathbf{p} + \mathbf{n} + \mathbf{n} + \mathbf{n}$

The cross section of spallation process of Eq. (3-3-14c) is calculated to be

$$\sigma v_{\rm pnnn} = \frac{8}{\pi^9} \left(\frac{32\pi^3}{a_{\rm He}^3}\right)^{3/2} g^2 \tan^2\theta_{\rm W} \sin^2\theta_\tau (1+3g_A^2) G_F^2 a_{\rm He} \Delta_{\rm pnnn}^7 \frac{m_{\rm N}^5}{m_{\tilde{\tau}} m_\tau^2} I_{\rm pnnn}, \tag{3-3-37}$$

where

$$I_{\rm pnnn} = \int_0^1 ds \int_0^{\sqrt{1-s^2}} dt \int_0^{\sqrt{1-s^2-t^2}} du \int_0^{\sqrt{1-s^2-t^2-u^2}} dv (1-s^2-t^2-u^2-v^2)^2 s t^2 u v^2 \\ \times \left\{ \frac{1}{\sqrt{2}} \exp\left[-\frac{k_N^2}{2a_{\rm He}} (3s^2+t^2+2u^2) \right] \sinh\left[\frac{\sqrt{2}k_{\rm N}^2}{a_{\rm He}} su \right] - \exp\left[-\frac{k_N^2}{2a_{\rm He}} (3s^2+t^2+u^2+v^2) \right] \sinh\left[\frac{k_{\rm N}^2}{a_{\rm He}} su \right] \right\} \tag{3-3-38}$$

where $\Delta_{\rm pnnn}$ and $k_{\rm N}$ are defined as follows:

$$\begin{aligned} &\Delta_{\rm pnnn} \equiv \delta m + \Delta_{\rm He} - \Delta_p - 3\Delta_n - E_{\rm b}, \\ &k_{\rm n} \equiv \sqrt{2 m_{\rm N} \Delta_{\rm pnnn}}. \end{aligned} \tag{3-3-39}$$

In this calculation, we assumed proton and neutron have an identical kinetic energy, and then the factor $k_{\rm p}$ and $k_{\rm n}$, which are introduced to factorize their kinetic energies, are also identical. $k_{\rm N}$ is the identical factor, and here we took $m_{\rm N} = m_{\rm n}$.

3.3.4 Comparing the rate of spallation reaction with that of stau-catalyzed fusion

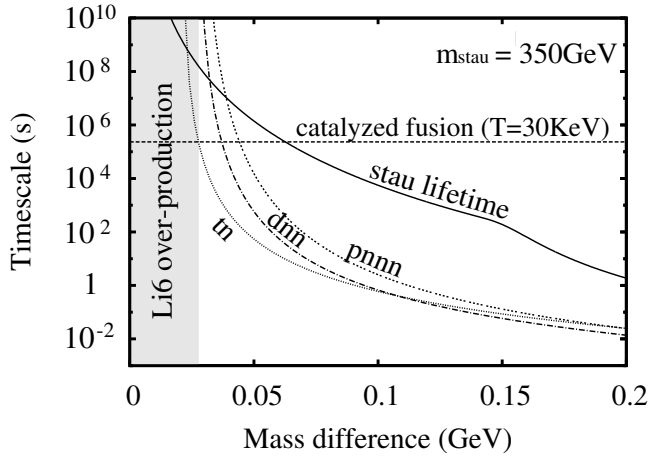

Figure 3.7: Timescale of spallation processes as a function of δm and the stau-catalyzed fusion at the universe temperature $T = 30$keV [37]. The lifetime of free $\tilde{\tau}$ (solid line) is also depicted. Here we took $m_{\tilde{\tau}} = 350$GeV, $\sin\theta_\tau = 0.8$, and $\gamma_\tau = 0$.

We compare the rate of the spallation and that of the stau-catalyzed fusion. We first note that the rate of stau-catalyzed fusion strongly depends on the temperature [37], and we fix the reference temperature to be 30keV. Staus begin to form a bound state with ^{4}He at this temperature, which corresponds to cosmic time of 10^3s. Thus the bound state is formed when the lifetime of staus is longer than 10^3s.

Figure 3.7 shows the timescale of the spallation processes as a function of δm. The lifetime of free stau is plotted by a solid line. We took the reference values of $m_{\tilde{\tau}} = 350$GeV, $\sin\theta_\tau = 0.8$, and $\gamma_\tau = 0$. The inverted rate of the stau-catalyzed fusion at the temperature of 30keV is also shown by the horizontal dashed line. Once a bound state is formed, as long as the phase space of spallation processes are open sufficiently that is $\delta m \gtrsim 0.026$GeV, those processes dominate over other processes. There $\tilde{\tau}$ property is constrained to evade the over-production of d and/or t. For $\delta m \lesssim 0.026$GeV, the dominant process of ($\tilde{\tau}^4$He) is stau-catalyzed fusion, since the free $\tilde{\tau}$ lifetime

is longer than the timescale of stau-catalyzed fusion. Thus light gray region is forbidden due to the over-production of ^{6}Li.

This interpretation of Fig.2 is not much altered by varying the parameters relevant with $\tilde{\tau}$. First cross sections of spallation processes are inversely proportional to $m_{\tilde{\tau}}$, and then the timescale of each process linearly increases as $m_{\tilde{\tau}}$ increases. Thus, even when $m_{\tilde{\tau}}$ is larger than $m_{\tilde{\tau}} = 350\text{GeV}$ by up to a factor of ten, the region of ^{6}Li over-production scarcely changes. Next we point out that our result depend only mildly on the left-right mixing of the stau. Indeed, cross section of the ^{4}He spallation is proportional to $\sin^2\theta_\tau$. Its order of magnitude will not change as long as the right-handed component is significant.

3.4 Relic density of Stau at the BBN era

In this subsection, we calculate the relic density of stau at the BBN era. Firstly, we briefly review the Boltzmann equations for the number density of stau and neutralino based on the thermal relic scenario. Then, we discuss the number desnisty evolution of stau and neutralino quantitatively. In subsec.3.4.2, we investigate the significant processes for the calculation of the relic density of stau. Finally, we obtain the Boltzmann equations for the relic density of stau in a convenient form.

3.4.1 Boltzmann equations for the number density evolution of stau and neutralino

In this subsubsection, we show the Boltzmann equations of stau and neutralino.

We are interested in the relic density of stau in the coannihilation scenario. In this scenario, stau and neutralino are quasi-degenerate in mass and decouple from the thermal bath almost at the same time. Thus the relic density of stau is given by solving a coupled set of the Boltzmann equations for stau and neutralino as simultaneous differential equation. For simplicity, we use the Maxwell-Boltzmann statistics for all species instead of the Fermi-Dirac for fermions and the Bose-Einstein for bosons, and assume T-invariance. With these simplifications, the Boltzmann equations of them are given as follows,

$$\begin{aligned}\frac{dn_{\tilde{\tau}^-}}{dt} + 3Hn_{\tilde{\tau}^-} =& -\sum_i \sum_{X,Y} \langle\sigma v\rangle_{\tilde{\tau}^- i \leftrightarrow XY} \left[n_{\tilde{\tau}^-} n_i - n^{eq}_{\tilde{\tau}^-} n^{eq}_i \left(\frac{n_X n_Y}{n^{eq}_X n^{eq}_Y} \right) \right] \\ & - \sum_{i \neq \tilde{\tau}^-} \sum_{X,Y} \left\{ \langle\sigma' v\rangle_{\tilde{\tau}^- X \to iY} \left[n_{\tilde{\tau}^-} n_X \right] - \langle\sigma' v\rangle_{iY \to \tilde{\tau}^- X} \left[n_i n_Y \right] \right\}, \end{aligned} \tag{3-4-1}$$

$$\begin{aligned}\frac{dn_{\tilde{\tau}^+}}{dt} + 3Hn_{\tilde{\tau}^+} =& -\sum_i \sum_{X,Y} \langle\sigma v\rangle_{\tilde{\tau}^+ i \leftrightarrow XY} \left[n_{\tilde{\tau}^+} n_i - n^{eq}_{\tilde{\tau}^+} n^{eq}_i \left(\frac{n_X n_Y}{n^{eq}_X n^{eq}_Y} \right) \right] \\ & - \sum_{i \neq \tilde{\tau}^+} \sum_{X,Y} \left\{ \langle\sigma' v\rangle_{\tilde{\tau}^+ X \to iY} \left[n_{\tilde{\tau}^+} n_X \right] - \langle\sigma' v\rangle_{iY \to \tilde{\tau}^+ X} \left[n_i n_Y \right] \right\}, \end{aligned} \tag{3-4-2}$$

$$\begin{aligned}\frac{dn_{\tilde{\chi}^0_1}}{dt} + 3Hn_{\tilde{\chi}^0_1} =& -\sum_i \sum_{X,Y} \langle\sigma v\rangle_{\tilde{\chi}^0_1 i \leftrightarrow XY} \left[n_{\tilde{\chi}^0_1} n_i - n^{eq}_{\tilde{\chi}^0_1} n^{eq}_i \left(\frac{n_X n_Y}{n^{eq}_X n^{eq}_Y} \right) \right] \\ & - \sum_{i \neq \tilde{\chi}^0_1} \sum_{X,Y} \left\{ \langle\sigma' v\rangle_{\tilde{\chi}^0_1 X \to iY} \left[n_{\tilde{\chi}^0_1} n_X \right] - \langle\sigma' v\rangle_{iY \to \tilde{\chi}^0_1 X} \left[n_i n_Y \right] \right\}. \end{aligned} \tag{3-4-3}$$

Here n and n^{eq} represent the actual number density and the equilibrium number density of each particle. Index i denotes stau and neutralino, and index X and Y denote SM particles. Note that if relevant SM particles are in thermal equilibrium, $n_X = n^{eq}_X, n_Y = n^{eq}_Y$, and $(n_X n_Y / n^{eq}_X n^{eq}_Y) = 1$

then these equations are reduced into a familiar form. $\langle\sigma' v\rangle$ and $\langle\sigma v\rangle$ are the thermal averaged cross sections, which is defined by

$$\begin{aligned}\langle\sigma v\rangle_{12\to 34} &\equiv g_{12}\frac{\int d^3\mathbf{p_1}d^3\mathbf{p_2}f_1 f_2(\sigma v)_{12\to 34}}{\int d^3\mathbf{p_1}d^3\mathbf{p_2}f_1 f_2} \\ &= g_{12}\frac{\int d^3\mathbf{p_1}d^3\mathbf{p_2}f_1 f_2(\sigma v)_{12\to 34}}{n_1^{eq}n_2^{eq}}\end{aligned} \tag{3-4-4}$$

where f is the distribution function of a particle, v is the relative velocity between initial state particles, and $g_{12} = 2(1)$ for same(different) particles 1 and 2. In this work, we assume that all of the supersymmetric particles except for stau and neutralino are heavy, and therefore do not involve them in the coannihilation processes.

The first line on the right hand side of Eqs. (3-4-1), (3-4-2) and (3-4-3) accounts for the annihilation and the inverse annihilation processes of the supersymmetric particles ($ij \leftrightarrow XY$). Here index j denotes stau and neutralino. As long as R-parity is conserved, the final number density of neutralino DM is controlled only by these processes. The second line accounts for the exchange processes by scattering off the cosmic thermal background ($iX \leftrightarrow jY$). These processes exchange stau with neutralino and vice versa, and thermalize them. Consequently, the number density ratio between them is controlled by these processes. Instead, these processes leave the total number density of the supersymmetric particles. Note that in general, although there are terms which account for decay and inverse decay processes of stau ($\tilde{\tau} \leftrightarrow \tilde{\chi}_1^0 XY...$) in the Boltzmann equations, we omit them. It is because we are interested in solving the ^{7}Li problem by the long-lived stau, and the whole intention of this work is to search parameters which can provide the solution for the ^{7}Li problem. Hence we assume that the stau is stable enough to survive until the BBN era, and focusing on the mass difference between stau and neutralino is small enough to make it possible.

In this subsection, we discuss the evolution of the number density of each species. Firstly, we discuss the number density evolution of neutralino DM. Since we have assumed R-parity conservation, all of the supersymmetric particles eventually decay into the LSP neutralino. Thus its final number density is simply described by the sum of the number density of all the supersymmetric particles

$$N = \sum_i n_i. \tag{3-4-5}$$

For N, that is the number density of the neutralino, we get the Boltzmann equation by summing Eqs (3-4-1), (3-4-2) and (3-4-3),

$$\frac{dN}{dt} + 3HN = -\langle\sigma v\rangle_{sum}\left[NN - N^{eq}N^{eq}\right] \tag{3-4-6}$$

$$\langle\sigma v\rangle_{sum} \equiv \sum_{i=\tilde{\chi}_1^0,\tilde{\tau}}\sum_{X,Y}\langle\sigma v\rangle_{\tilde{\chi}_1^0 i\leftrightarrow XY} \tag{3-4-7}$$

Solving the Eq. (3-4-6), we obtain N and find the freeze out temperature of the total number density of all the SUSY particles T_f by using the standard technique [25]:

$$\frac{m_{\tilde{\chi}_1^0}}{T_f} = \ln\frac{0.038 g m_{pl} m_{\tilde{\chi}_1^0}\langle\sigma v\rangle}{g_*^{1/2}(m_{\tilde{\chi}_1^0}/T_f)} \simeq 25. \tag{3-4-8}$$

Here, g and $m_{\tilde{\chi}_1^0}$ are the internal degrees of freedom and the mass of neutralino, respectively. The Plank mass $m_{pl} = 1.22\times 10^{19}$ GeV, and g_* are the total number of the relativistic degrees of freedom. Consequently, we see that $4\text{GeV} \le T_f \le 40\text{GeV}$ for $100\text{GeV} \le m_{\tilde{\chi}_1^0} \le 1000\text{GeV}$.

To obtain the relic density of stau, we solve a coupled set of the Boltzmann equations, (3-4-1), (3-4-2) and (3-4-3) as simultaneous differential equation. Each Boltzmann equation contains the contribution of the exchange processes. These processes exchange stau with neutralino and vice verse. At the temperature T_f, the interaction rate of the exchange processes is much larger than

that of the annihilation and the inverse annihilation processes. This is because the cross sections of the exchange processes are in the same order of magnitude as that of the annihilation and the inverse annihilation, but the number density of the SM particles is much larger than that of the supersymmetric particles which is suppressed by the Boltzmann factor. Thus even if the total number density of stau and neutralino is frozen out at the temperature T_f, each number density of them continue to evolve through the exchange processes.

Thus, to calculate the relic density of stau, we have to follow the two-step procedures. As a first step, we calculate the total relic density of the SUSY particles by solving the Eq. (3-4-6). We use the publicly available program micrOMEGAs [90] to calculate it. The second step is the calculation of the number density ratio of stau and neutralino. The second step is significant for calculating the relic density of stau at the BBN era, and hence we will discuss it in detail in latter.

3.4.2 The exchange processes and Lagrangian for describing them

After the freeze-out of the total number density of stau and neutralino, each of them is exchanged through the following processes

$$\tilde{\tau}\gamma \longleftrightarrow \tilde{\chi}_1^0\tau, \quad \tilde{\chi}_1^0\gamma \longleftrightarrow \tilde{\tau}\tau. \tag{3-4-9}$$

These processes Eq. (3-4-9) are described by the Lagrangian

$$\mathcal{L} = \tilde{\tau}^*\overline{\tilde{\chi}_1^0}(g_L P_L + g_R P_R)\tau - ie(\tilde{\tau}^*(\partial\tilde{\tau}) - (\partial_\mu\tilde{\tau}^*)\tilde{\tau})A^\mu + \text{h.c.}, \tag{3-4-10}$$

where e is the electromagnetic coupling constant, and $l \in \{e.\mu\}$. g_L and g_R are the coupling constants defined by Eq. (3-1-5).

The evolution of the stau number density is governed only by the exchange processes (Eq. (3-4-9)) after the freeze-out of the total relic density of stau and neutralino. When we calculate it, we should pay attention to two essential points relevant to the exchange processes.

One is the competition between the interaction rate of the exchange processes and the Hubble expansion rate, since when these interaction rates get smaller than the Hubble expansion rate, the relic density of stau would be frozen out. The other is whether tau leptons are in the thermal bath or not. The interaction rate of the exchange processes strongly depends on the number density of tau leptons. When tau leptons are in the thermal bath, the number density ratio between stau and neutralino are given by the thermal ratio,

$$\frac{n_{\tilde{\tau}}}{n_{\tilde{\chi}_1^0}} \simeq \frac{e^{-m_{\tilde{\tau}}/T}}{e^{-m_{\tilde{\chi}_1^0}/T}} = \exp\left(-\frac{\delta m}{T}\right), \tag{3-4-11}$$

through the exchange processes. On the contrary, once tau leptons decouple from the thermal bath, the ratio cannot reach this value. To calculate the relic density of stau, we have to comprehend the temperature of tau lepton decoupling.

To see whether tau leptons are in the thermal bath or not, we consider the Boltzmann equation for its number density,

$$\begin{aligned} &\frac{dn_\tau}{dt} + 3Hn_\tau = -\langle\sigma v\rangle\left[n_\tau n_X - n_\tau^{eq}n_X^{eq}\left(\frac{n_Y n_Z}{n_Y^{eq}n_Z^{eq}}\right)\right] - \langle\Gamma\rangle\left[n_\tau - n_\tau^{eq}\left(\frac{n_X n_Y \ldots}{n_X^{eq}n_Y^{eq}\ldots}\right),\right] \\ &\langle\sigma v\rangle = \sum_{X,Y,Z}\langle\sigma v\rangle_{\tau X\leftrightarrow YZ}, \quad \langle\Gamma\rangle = \sum_{X,Y,\ldots}\langle\Gamma\rangle_{\tau\leftrightarrow XY\ldots}, \end{aligned} \tag{3-4-12}$$

where indices $X, Y,$ and$Z$ denote the SM particles, and $\langle\Gamma\rangle$ represents the thermal averaged decay rate of tau lepton. When the SM particles X, Y,and Z are in the thermal equilibrium, $(n_Y)n_Z)/(n_Y)^{eq}n_Z^{eq}) = (n_X)n_Y)\cdots/(n_X)^{eq}n_Y^{eq}\cdots) = 1$, and hence tau leptons are sufficiently produced through the inverse annihilation and/or the inverse decay processes as long as these interaction rates are larger than the Hubble expansion rate. Therefore, whether tau leptons are in the thermal bath or not

can be distinguished by comparing the Hubble expansion rate H with the inverse annhilation rate of tau lepton $\langle\sigma v\rangle n_X^{eq}$, and the inverse decay rate of tau lepton $\langle\Gamma\rangle$. In other words, the inequality expression

$$\langle\sigma v\rangle n_X^{eq} > H \quad \text{and/or} \langle\Gamma\rangle > H \tag{3-4-13}$$

indicates that tau leptons are in the thermal bath. Fig.3.8 shows $\langle\Gamma\rangle n_X^{eq}, \langle\Gamma\rangle$, and H as a function of the thermal bath temperature. As shown in Fig.3.8, the inverse decay rate of tau lepton is much larger than the Hubble expansion rate. Thus, we can conclude that tau leptons remain in the thermal bath still at the beginning of the BBN.

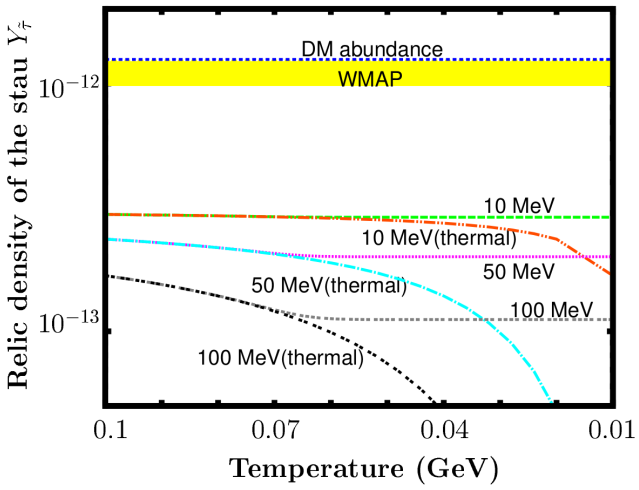

Figure 3.8: The evolution of the number density of negative charged stay. Each line attached [δm] shows the actual evolution of the number density of stau, while the one atattched [δm(thermal)] shows its evolution under the equilibrium determined given by Eq. (3-4-11) and the total relic abundance. Yellow band represents the allowed region from the WMAP observation at the 2 σ level.

3.4.3 Calculation of the number density ratio of stau and neutralino

The right-hand side of the Boltzmann equations (Eqs.(3-4-1), (3-4-2) and (3-4-3)) depends only on temperature, and hence it is convenient to use temperature T instead of time t as independent variable. To do this, we reformulate the Boltzmann equations by using the ratio of the number density to the entropy density s :

$$Y_i = \frac{n_i}{s}. \tag{3-4-14}$$

Consequently, we obtain the Boltzmann equations for the number density evolution of stau and neutralino

$$\frac{dY_{\tilde{\tau}^-}}{dT} = [3HTg_*(T)]^{-1}\left[3g_*(T) + T\frac{dg_*(T)}{dT}\right]s$$
$$\times\left\{\langle\sigma v\rangle_{\tilde{\tau}^-\gamma\to\tilde{\chi}_1^0\tau^-}Y_{\tilde{\tau}^-}Y_\gamma - \langle\sigma v\rangle_{\tilde{\chi}_1^0\tau^-\to\tilde{\tau}^-\gamma}Y_{\tilde{\chi}_1^0}Y_{\tau^-} + \langle\sigma v\rangle_{\tilde{\tau}^-\tau^+\to\tilde{\chi}_1^0\gamma}Y_{\tilde{\tau}^-}Y_{\tau^+} - \langle\sigma v\rangle_{\tilde{\chi}_1^0\gamma\to\tilde{\tau}^-\tau^+}Y_{\tilde{\chi}_1^0}Y_\gamma\right\} \tag{3-4-15}$$

$$\frac{dY_{\tilde{\tau}^+}}{dT} = [3HTg_*(T)]^{-1}\left[3g_*(T) + T\frac{dg_*(T)}{dT}\right]s$$
$$\times\left\{\langle\sigma v\rangle_{\tilde{\tau}^+\gamma\to\tilde{\chi}_1^0\tau^+}Y_{\tilde{\tau}^+}Y_\gamma - \langle\sigma v\rangle_{\tilde{\chi}_1^0\tau^+\to\tilde{\tau}^+\gamma}Y_{\tilde{\chi}_1^0}Y_{\tau^+} + \langle\sigma v\rangle_{\tilde{\tau}^+\tau^-\to\tilde{\chi}_1^0\gamma}Y_{\tilde{\tau}^-}Y_{\tau^-} - \langle\sigma v\rangle_{\tilde{\chi}_1^0\gamma\to\tilde{\tau}^+\tau^-}Y_{\tilde{\chi}_1^0}Y_\gamma\right\} \tag{3-4-16}$$

$$\frac{dY_{\tilde{\chi}_1^0}}{dT} = [3HTg_*(T)]^{-1}\left[3g_*(T) + T\frac{dg_*(T)}{dT}\right]s$$
$$\times\left\{\langle\sigma v\rangle_{\tilde{\chi}_1^0\tau^-\to\tilde{\tau}^-\gamma}Y_{\tilde{\chi}_1^0}Y_{\tau^-} - \langle\sigma v\rangle_{\tilde{\tau}^-\gamma\to\tilde{\chi}_1^0\tau^-}Y_{\tilde{\tau}^-}Y_\gamma + \langle\sigma v\rangle_{\tilde{\chi}_1^0\gamma\to\tilde{\tau}^-\tau^+}Y_{\tilde{\chi}_1^0}Y_\gamma - \langle\sigma v\rangle_{\tilde{\tau}^-\tau^+\to\tilde{\chi}_1^0\gamma}Y_{\tilde{\tau}^-}Y_{\tau^+}\right.$$
$$\left. + \langle\sigma v\rangle_{\tilde{\chi}_1^0\tau^+\to\tilde{\tau}^+\gamma}Y_{\tilde{\chi}_1^0}Y_{\tau^+} - \langle\sigma v\rangle_{\tilde{\tau}^+\gamma\to\tilde{\chi}_1^0\tau^+}Y_{\tilde{\tau}^+}Y_\gamma + \langle\sigma v\rangle_{\tilde{\chi}_1^0\gamma\to\tilde{\tau}^+\tau^-}Y_{\tilde{\chi}_1^0}Y_\gamma - \langle\sigma v\rangle_{\tilde{\tau}^+\tau^-\to\tilde{\chi}_1^0\gamma}Y_{\tilde{\tau}^+}Y_{\tau^-}\right\} \tag{3-4-17}$$

Here $g_*(T)$ is the relativistic degrees of freedom, and we use

$$s = \frac{2\pi^2}{45}g_*(T)T^3, \quad H = 1.66g_*^{1/2}\frac{T^2}{m_{pl}}. \tag{3-4-18}$$

We obtain the relic density of stau at the BBN era by integrating these equations from T_f to the temperature for beginning the BBN under the initial condition of the total number density of stau and neutralino. These equations make it clear that if the tau number density is out of the equilibrium, the ratio between those of stau and neutralino does not satisfy the Eq. (3-4-11).

,

3.4.4 Long-lived stau and BBN

We numerically calculate the primordial abundances of light elements including ^{4}He spallation processes and $\tilde{\tau}$ catalyzed nuclear fusion. Then we can search for allowed regions of the parameter space to fit observational light element abundances.

So far it has been reported that there is a discrepancy between the theoretical value of ^{7}Li abundance predicted in the standard BBN (SBBN) and the observational one. This is called ^{7}Li problem. SBBN predicts the ^{7}Li to H ratio to be $\mathrm{Log}_{10}(^7\mathrm{Li/H}) = -9.35 \pm 0.06$ when we adopt a recent value of baryon to photon ratio $\eta = (6.225 \pm 0.170) \times 10^{-10}$ (68% C.L.) reported by the WMAP satellite [72], and experimental data of the rate for the ^{7}Li or ^{7}Be production through $^3\mathrm{He} + {}^4\mathrm{He} \to {}^7\mathrm{Be} + \gamma$ [75] (^{7}Li is produced from ^{7}Be by its electron capture, $^7\mathrm{Be} + e^- \to {}^7\mathrm{Li} + \nu_e$ at a later epoch). On the other hand, the primordial ^{7}Li abundance is observed in metal-poor halo stars as absorption lines [64]. Recent observationally-inferred value of the primordial ^{7}Li to hydrogen ratio is $\mathrm{Log}_{10}(^7\mathrm{Li/H}) = -9.63 \pm 0.06$ [119] for a high value, and $\mathrm{Log}_{10}(^7\mathrm{Li/H}) = -9.90 \pm 0.09$ [120] for a low value. (See also Refs. [74, 121, 122] for another values.) Therefore there is a discrepancy at more than three sigma between theoretical and observational values even when we adopt the high value of [119]. This discrepancy can be hardly attributed to the correction of the cross section of nuclear reaction [123, 124]. Even if we consider nonstandard astrophysical models such as those including diffusion effects [125, 126], it might be difficult to fit all of the data consistently [127].

In Figs. 3.4.4 and 3.4.4, we plot the allowed parameter regions which are obtained by comparing the theoretical values to observational ones for the high and low ^{7}Li/H, respectively. Vertical axis is the yield value of $\tilde{\tau}$ at the time of the formation of the bound states with nuclei, $Y_{\tilde{\tau}} = n_{\tilde{\tau}}/s$ (s is the entropy density), and horizontal axis is the mass difference of $\tilde{\tau}$ and $\tilde{\chi}_1^0$. We have adopted following another observational constraints on the light element abundances: an upper bound on the ^{6}Li to ^{7}Li ratio, $^6\mathrm{Li}/^7\mathrm{Li} < 0.046 + 0.022$ [121], the deuteron to hydrogen ratio, D/H=$(2.80 \pm 0.20) \times 10^{-5}$ [128], and an upper bound on the ^{3}He to deuteron ratio, $^3\mathrm{He/D} < 0.87 + 0.27$ [129].

The solid line (orange line) denotes a theoretical value of the thermal relic abundance for staus [53] while keeping observationally-allowed dark matter density $\Omega_{\mathrm{DM}}h^2 = 0.11 \pm 0.01$ (2 σ) [72] as total

$\chi_1^0 + \tilde{\tau}$ abundance. For reference, we also plot the observationally-allowed dark matter density in the figures by a horizontal band.

At around $\delta m \sim 0.1$ GeV, we find that ^{7}Li/H can be fitted to the observational value without conflicting with the other light element abundances. [1] As shown in Fig. 3.4.4, it should be impressive that the relic density is consistent with the allowed region at $Y_{\tilde{\tau}} = 2 \times 10^{-13}$ at 3 σ in case of the high value of ^{7}Li/H in [119].

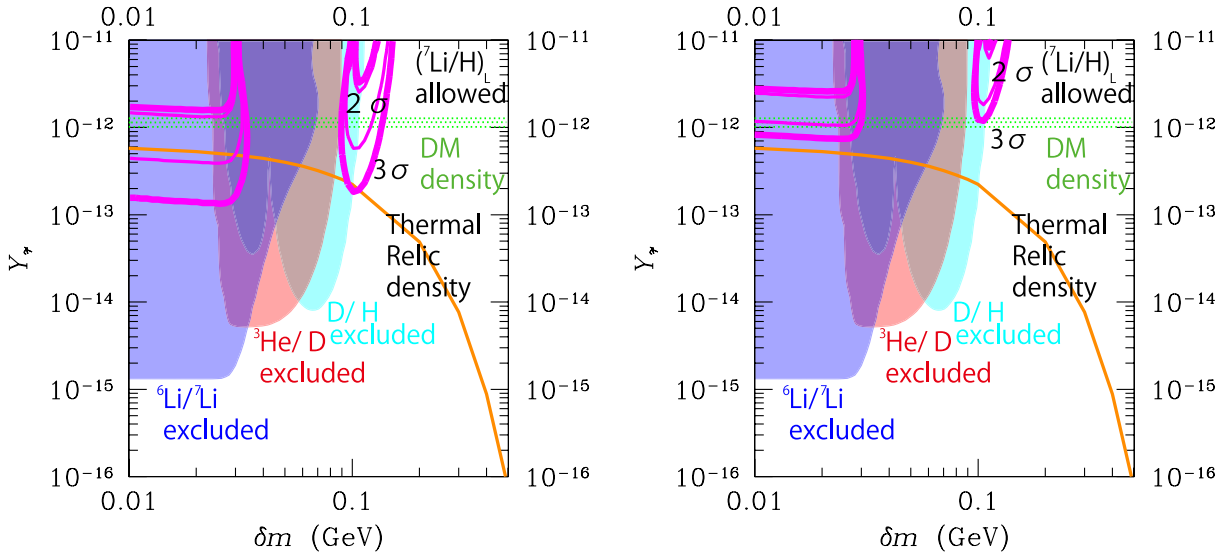

Figure 3.9: Left Panel: Allowed regions from observational light element abundances at 2 σ. Here we have adopted the higher value of the observational ^{7}Li/H in [119] denoted by $(^7\mathrm{Li/H})_\mathrm{H}$, and have plotted both the 2σ (thin line) and 3σ (thick line) only for ^{7}Li/H. The horizontal band means the observationally-allowed dark matter density. We have adopted $m_{\tilde{\tau}} = 350$ GeV, $\sin\theta_\tau = 0.8$, and $\gamma_\tau = 0$, respectively. Right Panel:Same as left panel, but for the lower value of observational ^{7}Li/H reported in [120], which is denoted by $(^7\mathrm{Li/H})_\mathrm{L}$.

[1] See also [30, 38, 55, 57, 130] for another mechanisms to reduce ^{7}Li/H.

Chapter 4

The discovery potential of the CMSSM at the LHC

We have shown the solution of the Li problem and the DM abundance in the MSSM. From now on, we will explain the solusion in the constrained MSSM. Furthermore, we simultaneously explain 125 GeV Higgs boson mass.

In the CMSSM, all of the observables are described by only five parameters. We constrain the five parameters to be consistent with the phenomenological requirements, e.g., the success of the BBN, suitable DM abundance, and 125 GeV Higgs boson mass. Therefore we narrow the parameter space of the CMSSM.

In addition, we give predictions to the anomalous magnetic moment of muon, branching fractions of the B-meson rare decays, the direct detection of the neutralino dark matter, and the number of SUSY particles produced in 14 TeV run at the LHC experiment in the allowed region. We compare these predictions with current bounds, and thus we show the predictability of this scenario.

4.1 Constraints

In this section, we start our discussion to briefly review the CMSSM and show our constraints to derive the allowed region of the parameter space in the CMSSM.

The CMSSM is described by four parameters and a sign,

$$m_0, M_{1/2}, A_0, \tan\beta, \mathrm{sign}(\mu), \tag{4-1-1}$$

where the first three parameters are the universal scalar mass, the universal gaugino mass, and the universal trilinear coupling at the scale of grand unification, respectively. Here, $\tan\beta$ is the ratio of the vacuum expectation values of two Higgs bosons, and μ is the supersymmetric Higgsino mass parameter. In the CMSSM, we describe all observables by these parameters, and, hence, we can derive the favored parameter space by putting the experimental/observational constraints on the calculated observables.

From now on, we explain in more detail our constraints and how to apply those to our numerical calculations. The first requirement comes from the Higgs boson mass. The latest reports on its mass m_h are

$$m_h = 125.8 \pm 0.4(\mathrm{stat}) \pm 0.4(\mathrm{syst})\ \mathrm{GeV}, \tag{4-1-2}$$

by the CMS Collaboration [91], and

$$m_h = 125.2 \pm 0.3(\mathrm{stat}) \pm 0.6(\mathrm{syst})\ \mathrm{GeV}, \tag{4-1-3}$$

by the ATLAS Collaboration [92]. It is known that the Higgs boson mass calculated by each public code fluctuates by about ± 3 GeV [93, 94, 95, 96]. Taking into account these uncertainties, we apply

a more conservative constraint as

$$m_h = 125.0 \pm 3.0 \text{ GeV}. \tag{4-1-4}$$

The second constraint comes from the observation for the relic abundance of dark matter. The WMAP satellite reported the value at the 3 σ level [18],

$$0.089 \leq \Omega_{\rm DM} h^2 \leq 0.136. \tag{4-1-5}$$

In most of the CMSSM parameter space, the relic abundance of the neutralino LSP is overabundant against the measured value. The correct dark matter abundance requires unique parameter space where the bino-like neutralino LSP and the stau NLSP are degenerate in mass so that the coannihilation mechanism works well [24, 25].

The third and fourth constraints are required from solving the lithium-7 problem. The stau NLSP is long-lived if the mass difference is smaller than the mass of the tau lepton [28, 29]. In the case where the stau survives until the BBN epoch, the lithium-7 density can be reduced to the measured value with the exotic nuclear reactions induced by the stau. As the third condition, we impose the mass difference δm to be

$$\delta m \equiv m_{\tilde{\tau}_1} - m_{\tilde{\chi}_1^0} \leq 0.1 \text{ GeV}, \tag{4-1-6}$$

where $m_{\tilde{\tau}_1}$ and $m_{\tilde{\chi}_1^0}$ are the masses of the stau NLSP and the neutralino LSP, respectively. With this mass difference, the stau NLSP is sufficiently long-lived so that it can survive until the BBN era [40, 53, 58]. In our numerical calculation, we use the pole mass of the top quark as an input which involves an uncertainty of $\mathcal{O}(1)$ GeV. It is expected that the SUSY spectrum also includes the same order of uncertainties. For this reason, in the numerical results in the next section, we show also the case of

$$\delta m \leq 1 \text{ GeV} \tag{4-1-7}$$

to make a more conservative prediction of the CMSSM parameters.[1]

The forth constraint is the upper bound on the mass of the neutralino LSP,

$$m_{\tilde{\chi}_1^0} \leq 450 \text{ GeV}. \tag{4-1-8}$$

This upper bound is derived from the requirement of the abundances of both dark matter and light elements.

We showed in Ref. [58] that a yield value of the negatively charged stau $Y_{\tilde{\tau}} = n_{\tilde{\tau}}/s$ (s is the entropy density) must be larger than a minimum value

$$Y_{\tilde{\tau},\rm m} = 1.0 \times 10^{-13} \tag{4-1-9}$$

to obtain the appropriate abundance of light elements, mainly, that of lithium 7, as

$$Y_{\tilde{\tau},m} \leq Y_{\tilde{\tau}}. \tag{4-1-10}$$

At the same time, the abundance of stau is bound from above by the abundance of dark matter. From Eq.(4-1-5), we obtain the following bound as

$$\frac{m_{\tilde{\chi}_1^0} n_{\rm DM} h^2}{\rho_c} \leq 0.136. \tag{4-1-11}$$

[1] In a precise sense, a too small mass difference makes the stau too long-lived. If the stau lives long, sufficient to form a bound state with helium, the stau converts it into other nuclei, a triton (or a deuteron) and neutron(s). Those reactions make the number densities of the converted nuclei too large compared with those of the observations [58]. The number densities of these nuclei, therefore, become inconsistent with the observed values through those reactions, and the too small mass difference is not allowed. This is, however, considerably relaxed by introducing a tiny lepton flavor violation [60].

Here, $n_{\rm DM}$ is today's number density of the dark matter, $\rho_{\rm c}$ is the critical density of the Universe, $\rho_{\rm c} = 1.054 \times 10^{-5}$ GeV cm^{-3}, and h is the scale factor for the Hubble expansion rate, $h = 0.710$. We express $n_{\rm DM}$ by using the $Y_{\tilde{\tau}}$ to be

$$n_{\rm DM} = 2s_0(1 + e^{\delta m/T_{\rm f}})Y_{\tilde{\tau}}. \tag{4-1-12}$$

Here, s_0 is today's entropy density, $s_0 = 2889.2$ cm^{-3}, and T_f is the freeze-out temperature for the exchange process between the stau and the neutralino and given by

$$T_{\rm f} \simeq \frac{m_\tau - \delta m}{25}. \tag{4-1-13}$$

Here, $m_\tau = 1.777$ GeV and we took $\delta m = 0.1$ GeV as a reference value. Using Eqs.(4-1-9)-(4-1-12), we obtain the lower and upper bounds for the yield value of the stau as follows:

$$1.0 \times 10^{-13} \leq Y_{\tilde{\tau}} \leq \frac{\rho_c}{2(1 + e^{\delta m/T_{\rm f}})s_0 h^2} \frac{0.136}{m_{\tilde{\chi}_1^0}}. \tag{4-1-14}$$

From the equation, we put the following bound as

$$m_{\tilde{\chi}_1^0} \leq 450 \text{ GeV} \tag{4-1-15}$$

on the mass of the neutralino.

4.2 Allowed region in the CMSSM

In this section, we show the allowed region in the CMSSM parameter space by imposing the constraints explained in Sec. 4.1. Throughout this paper, we take $\tan\beta = 10,\ 20$, and 30 as illustrating examples. In the case of the $\tan\beta \lesssim 10$, the Higgs boson mass hardly reaches 125 GeV because its tree-level mass is proportional to $|\cos 2\beta|$ and radiative corrections are not large enough. On the other hand, in the case of $\tan\beta \gtrsim 30$, the dark matter abundance lowers the observational value. This is because the annihilation rates are enhanced by large $\tan\beta$. As is shown in Eq. (4-1-8), the mass of the neutralino LSP is bound from above and cannot compensate the small number density. Thus, it is expected that most of the allowed parameter space is obtained in this range of $\tan\beta$. We calculate the SUSY spectrum, the DM abundance, and the other observables using micrOMEGAs [90] implementing SPheno [97, 98] and the lightest Higgs mass using FeynHiggs [99, 100, 101, 102].

4.2.1 A_0 - m_0 plane

In Fig. 4.1, we show the allowed region in the m_0-A_0 plane for $\tan\beta = 10,\ 20$, and 30 from top to bottom and $\delta m \leq 1$ and 0.1 GeV in the left and right panels, respectively. Color represents $M_{1/2}$.

Notably, one can see that A_0 and m_0 have an almost linear relation for fixed $M_{1/2}$. The relations can be parametrized as

$$m_0 = \begin{cases} (-5.5 \times 10^{-3} A_0 + 5.15)\tan\beta + 67.67 \\ \text{for lower line,} \\ (-5.5 \times 10^{-3} A_0 + 4.65)\tan\beta + 140.67 \\ \text{for upper line,} \end{cases} \tag{4-2-1}$$

for $\tan\beta \ni (10, 20, 30)$. These linear relations come from the tight degeneracy in mass between the stau and the neutralino. We explain the linear relation as follows. First, we note that the signs of μ and A_0 are opposite from each other due to obtaining the large Higgs boson mass, as we will explain later. In this scenario, we choose $\mu > 0$ and $A_0 < 0$. For a fixed $m_{\tilde{\chi}_1^0}$, in response to an increasing m_0, the mass of the lighter stau is also increased. In order to keep the mass difference smaller than 1 GeV (0.1 GeV), $|A_0|$ has to be increased also. Increasing of $|A_0|$ makes a nondiagonal element of

the stau mass matrix large, and, hence, the mass eigenvalue of the lighter stau is decreased after diagonalization to be within the small mass difference. As a result, the linear behavior in the A_0-m_0 plane is found.

One can see in Fig. 4.1 that m_0 in the allowed region increases as $\tan\beta$ increases. This is because the soft masses of the staus are decreased more for larger $\tan\beta$ in the renormalization group (RG) running due to the tau Yukawa couplings. The terms with a tau Yukawa coupling in RG Equation (RGE) decrease the soft masses in the running [103]. These become significant when $\tan\beta$ is large because the tau Yukawa coupling is proportional to $1/\cos\beta$. Thus, a larger m_0 is required for a larger $\tan\beta$ to obtain the stau mass satisfying Eqs. (4-1-6) or (4-1-7).

The upper and lower edges of the allowed region in all panels of Fig. 4.1 are determined by the constraints of the correct abundances of dark matter and the light elements. This can be understood as follows. Since the dark matter abundance depends on the neutralino LSP mass as shown in Eq. (4-1-5), the dark matter abundance gives the lower bound on the neutralino mass. On the other hand, the light element's abundance gives the upper bound as shown in Eq. (4-1-8). The bounds for the lighter stau mass are nearly the same as that for the neutralino mass due to the tight degeneracy. Therefore, once A_0 is fixed, m_0 can vary in a range that satisfies the bound for the lighter stau mass. Thus, the upper and lower edges are determined by the constraints.

On the other hand, the right side of the allowed region is determined by the lower bound on the Higgs boson mass. We can see from the left panel of Fig. 4.2 that the Higgs boson mass reaches 122 GeV. The mass squared of the Higgs boson with one-loop corrections is given by

$$\begin{aligned} m_h^2 &= m_Z^2 \cos^2 2\beta \\ &\quad + \frac{3m_t^4}{16\pi^2 v^2}\left[\log\left(\frac{m_{\tilde{t}}^2}{m_t^2}\right) + \frac{X_t^2}{m_{\tilde{t}}^2}\left(1 - \frac{X_t^2}{12m_{\tilde{t}}^2}\right)\right], \\ &\quad (X_t = A_t - \mu\cot\beta, \quad m_{\tilde{t}} = \sqrt{m_{\tilde{t}_1} m_{\tilde{t}_2}}), \end{aligned} \tag{4-2-2}$$

where the first line represents the tree-level mass square, and the second one is the one-loop corrections [11, 10, 9, 12]. The tree-level contribution is simply given by the Z-boson mass m_Z, while the radiative corrections are given by the masses of the top m_t, the lighter/heavier stop $m_{\tilde{t}_{1/\tilde{t}_2}}$, the stop mixing parameter X_t, and the vacuum expectation values of the Higgs bosons, $v = \sqrt{v_u^2 + v_d^2}$; here, v_u and v_d are the vacuum expectation values of up-type and down-type Higgs bosons, respectively. The radiative corrections are sensitive to the stop mixing parameter. As is well known, the second term in the bracket decreases quadratically from its maximum at

$$|X_t| = \sqrt{6} m_{\tilde{t}}. \tag{4-2-3}$$

To obtain the maximum value of $|X_t|$, the signs of μ and A_0 have to be opposite each other, and we choose $\mu > 0$ and $A_0 < 0$ in this paper. The right panel of Fig. 4.2 shows $|X_t|/\sqrt{6}m_{\tilde{t}}$ in the allowed region for $\tan\beta = 20$ and $\delta m \leq 1$ GeV. It can be seen that $|X_t|$ is smaller than $\sqrt{6}m_{\tilde{t}}$ at the right side edge, and, hence, the one-loop corrections are not so large that m_h is pushed up to the lower bound. Similarly, the left side edge is also determined by the Higgs boson mass bound. The value of $|X_t|/\sqrt{6}m_{\tilde{t}}$ gradually becomes large as $|A_0|$ increases. At a large $(|A_0|, m_0)$ point, the value of $|X_t|/\sqrt{6}m_{\tilde{t}}$ is equal to 1, and, therefore, m_h receives the maximal loop correction. In the region where $|X_t|/\sqrt{6}m_{\tilde{t}} > 1$, the loop corrections to m_h are smaller and m_h decreases from the maximal value. Therefore, m_h is smaller than 122 GeV again at the left side edge, as can be seen in the right panel of Fig. 4.2.

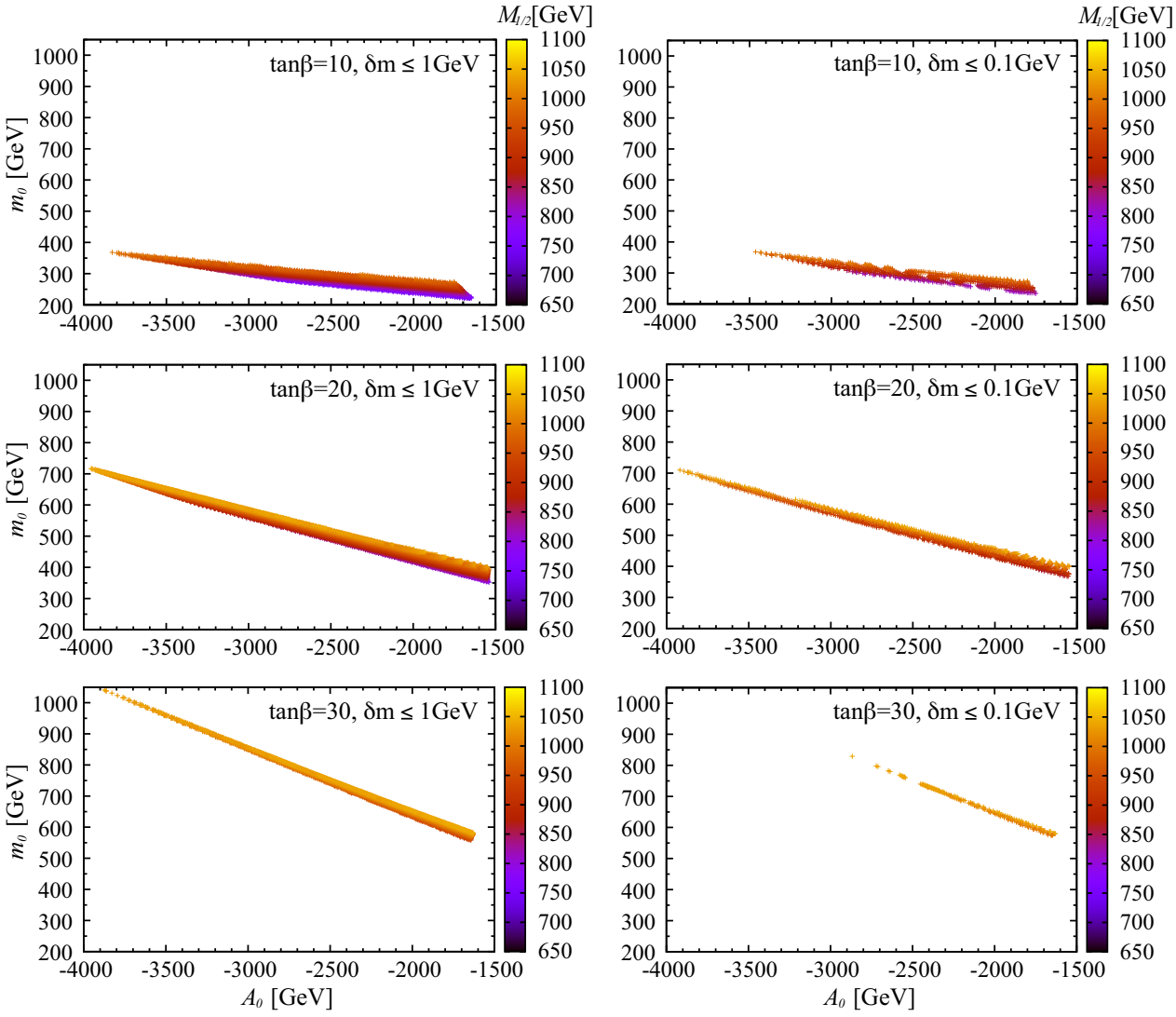

Figure 4.1: The allowed region in the A_0-m_0 plane. We fix $\tan\beta$ to 10, 20, and 30 from top to bottom and $\delta m \leq 1$ and 0.1 GeV from left to right, respectively. A gradation of colors represents $M_{1/2}$. Light color indicates large value, and dark color indicates small value.

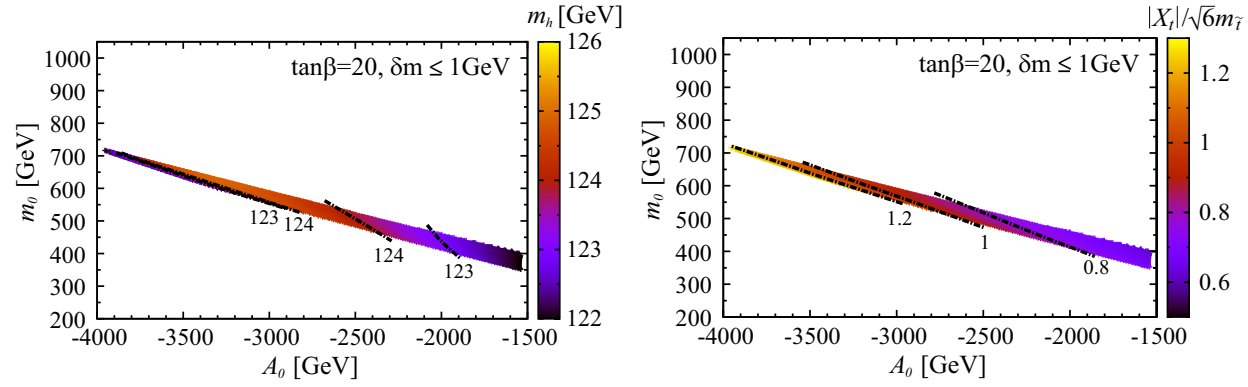

Figure 4.2: Left panel:the value of the Higgs boson mass. Right panel: the ratio of $|X_t|$ to $\sqrt{6}m_{\tilde{t}}$. A gradation of colors represents each value. Light color indicates large value and dark color indicates small value. We fix $\tan\beta$ to 20 and $\delta m \leq 1$ GeV in each figure.

4.2.2 m_0 - $M_{1/2}$ plane

We show in Fig. 4.3 the allowed region in the m_0-$M_{1/2}$ plane for $\tan\beta = 10,\ 20$, and 30 from top to bottom and $\delta m \leq 1$ and 0.1 GeV in the left and right panels, respectively. Color and the contours represent A_0. Figure 4.4 shows the Higgs boson mass in the left panel and the relic abundance of the dark matter in the right panel by color on the allowed region. We fix $\tan\beta$ to 20 and $\delta m \leq 1$ GeV in the panels.

In Fig. 4.3, it can be seen that $|A_0|$ gets larger as m_0 gets larger while it is slightly dependent on $M_{1/2}$. This is because the lighter stau mass is mainly determined by m_0 and A_0 as explained in Sec. 4.2.1. In the figure, we obtain $m_h \simeq 126$ GeV, at $(m_0, M_{1/2}) = (350, 1000)$ GeV for $\tan\beta = 10$, $(640, 1050)$ GeV for $\tan\beta = 20$, and $(800, 1050)$ GeV for $\tan\beta = 30$, respectively. These points are located at the middle of m_0 and the upper edge of $M_{1/2}$ in the allowed region. The value of $|X_t|$ is equal to $\sqrt{6}m_{\tilde{t}}$ at these points, and, hence, m_h receives the large loop corrections. Furthermore, the logarithmic term in Eq. (4-2-2) becomes large as $M_{1/2}$ increases since the stops become heavy, as we show later in Fig. 4.6. Thus, the Higgs boson mass is pushed up to 126 GeV. The Higgs boson mass decreases as the parameters deviate from these points. In the left panel of Fig. 4.4, it is clearly seen that the lower bound on the Higgs boson mass determines the left and right edges in the allowed region. Since $|A_0|$ is small at the left edge, the value of $|X_t|$ is smaller than $\sqrt{6}m_{\tilde{t}}$. Therefore, m_h receives a small one-loop correction. On the contrary, $|A_0|$ is large at the right edge, and $|X_t|$ is larger than $\sqrt{6}m_{\tilde{t}}$. This means that m_h receives a small one-loop correction, as we explained in the previous subsection.

Note that the minimum value of $M_{1/2}$ in the allowed region is different in each panel. The minimum value is determined by the lower bound on the relic abundance of the dark matter. In the right panel of Fig. 4.4, we can see that the neutralino relic abundance reaches the lower bound at the bottom edge of the allowed region.[2] The minimum value of $M_{1/2}$ becomes large as $\tan\beta$ increases and/or the mass difference becomes small.

The $\tan\beta$ dependence on the relic abundance is understood as follows. In the favored parameter region, the stau NLSP consists mostly of the right-handed stau. Then the dominant contribution to the total coannihilation rate of the dark matter is the stau-stau annihilation into tau leptons via Higgsino exchange for large $\tan\beta$ [104]. The interactions of the stau-tau lepton Higgsino is proportional to $\tan\beta$, and so the large $\tan\beta$ leads the large coannihilation rate of the dark matter. Larger $\tan\beta$, therefore, makes the relic abundance smaller.

The dependence of the relic number density on the mass difference is understood in terms of the ratio of the number density of the stau to the neutralino. At the freeze-out of the total number of all SUSY particles, the ratio is proportional to $e^{-\delta m/T_f^{\rm total}}$. Since the freeze-out temperature $T_f^{\rm total}$ is almost the same for $\delta m = 0.1$ and 1 GeV as long as $m_{\tilde{\chi}_1^0}$ is fixed, the stau number density is relatively large for $\delta m = 0.1$ GeV. This leads to a larger total coannihilation rate and, hence, the relic number density of the neutralino is reduced. Such a reduction of the number density can be compensated by increasing the neutralino mass. Thus, the minimum value of $M_{1/2}$ should be larger for larger $\tan\beta$ and smaller δm to meet the lower bound for the dark matter abundance.

On the other hand, the maximum value of $M_{1/2}$ is fixed from the upper bound in Eq. (4-1-8). Note that the upper bound is derived by the fact that the large number density of the stau is required to reduce the lithium-7 to the measured abundance. This requirement forbids a too large mass of the neutralino. As there is a relation between the neutralino mass and $M_{1/2}$, i.e., $m_{\tilde{\chi}_1^0} \simeq 0.43 M_{1/2}$, the upper bound of $M_{1/2}$ is estimated by the neutralino mass and is fixed to be 1.1 TeV in the present paper.

We emphasize here that the maximum value of $M_{1/2}$ in the allowed region is unique in the parameter space. If we do not take into account the lithium-7 problem, a heavier neutralino or $M_{1/2}$ is allowed, and, hence, the resultant range of $M_{1/2}$ is wider.

[2] In the panel, we see moderate stripes on the allowed region. These stripes result from the loss accuracy of the numerical calculation. We are not able to collect all data with the mass difference within 0.1 GeV. If we collect all data, these stripes are not on the allowed region.

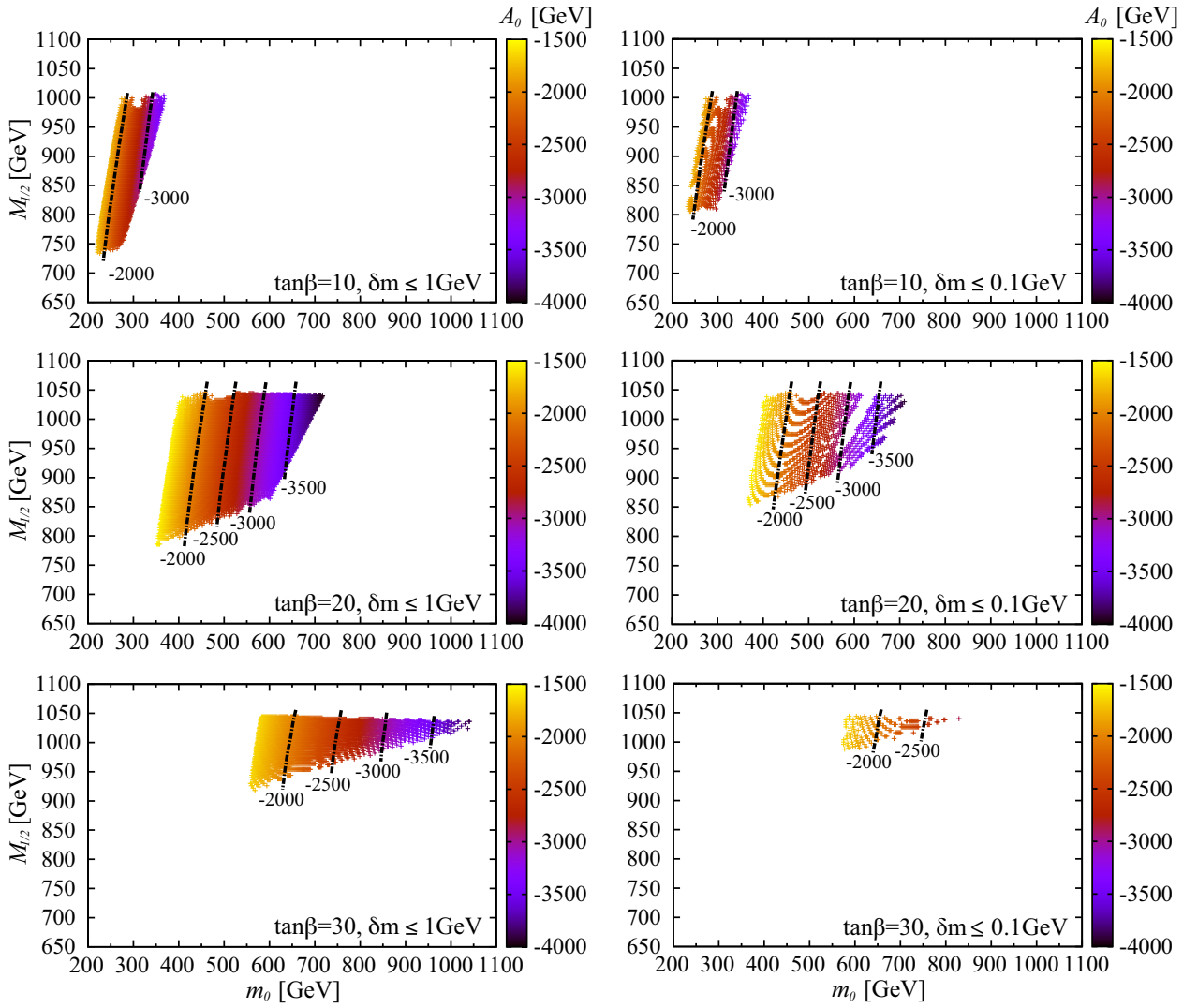

Figure 4.3: The allowed parameter region in the m_0-$M_{1/2}$ plane. We fix $\tan\beta$ to 10, 20, and 30 from top to bottom and $\delta m \leq 1$ and 0.1 GeV from left to right, respectively. A gradation of colors represents A_0. Light color indicates large value and dark color indicates small value.

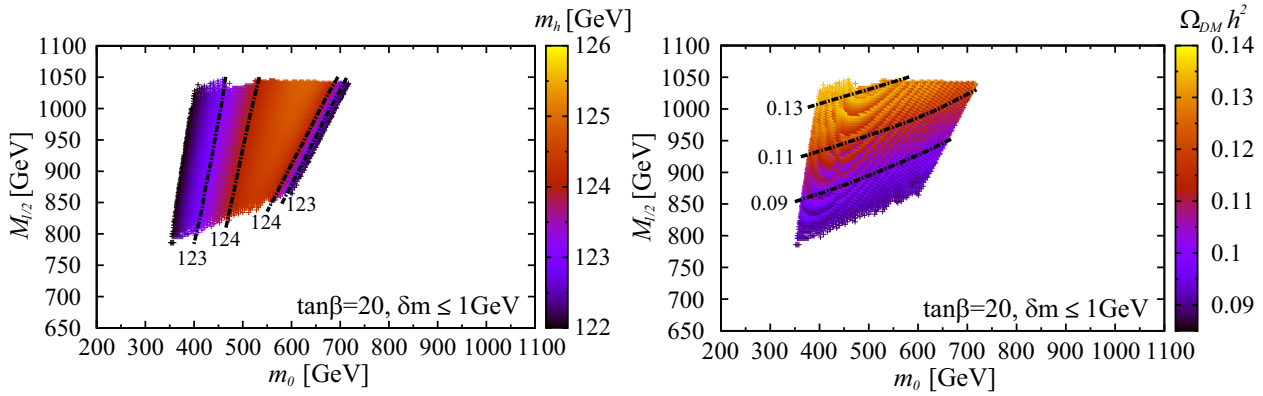

Figure 4.4: Left panel:the value of the Higgs boson mass. Right panel: the value of the relic abundance of the dark matter. A gradation of colors represents each value. Light color indicates large value and dark color indicates small value. We fix $\tan\beta$ to 20 and $\delta m \leq 1$ GeV in each figure.

4.3 SUSY spectrum, $(g-2)_\mu$, B-meson rare decays, and dark matter detection

In this section, we show our predictions for the SUSY spectrum, the muon anomalous magnetic moment, rare decays of B mesons, and the dark matter direct detections. We calculate the mass spectrum of SUSY particles by using SPheno [97, 98] and that of the Higgs boson by using Feyn-Higgs [99, 100, 101, 102].

4.3.1 Spectra of SUSY particles with current limits

We show the mass spectra of the SUSY particles in the allowed region. Figure 4.5 shows the masses of the gluino and the first and second generation squarks with respect to the lightest neutralino mass. From top to bottom, $\tan\beta$ is varied with 10, 20, and 30, and in the left and right panels $\delta m \leq 1$ and 0.1 GeV. Similarly, the masses of the stop and sbottom are shown in Fig. 4.6, those of the neutralino, slepton and the heavier Higgs in Figs. 4.7, 4.8, and 4.9, respectively. Note that in all of the figures we have excluded the region with $m_{\tilde{\chi}_1^0}(\simeq m_{\tilde{\tau}_1}) \lesssim 339$ GeV, which is the direct bound on the long-lived CHAMP at the LHC [105]. We explain the behaviors of these figures in the following subsections.

Gluino, neutralinos and heavy Higgs boson masses

In the CMSSM, the gluino mass parameters M_3 is related to the bino and the wino mass parameter M_1 and M_2 at one-loop RGE as follows:

$$M_3 = \frac{\alpha_s}{\alpha}\sin^2\theta_W M_2 = \frac{3}{5}\frac{\alpha_s}{\alpha}\cos^2\theta_W M_1. \tag{4-3-1}$$

From this relation, we can obtain the ratio

$$M_3 : M_2 : M_1 \simeq 6 : 2 : 1 \tag{4-3-2}$$

around the TeV scale. We can see that $m_{\tilde{g}}$ is nearly 6 times larger than $m_{\tilde{\chi}_1^0}$ in Fig. 4.5, and $m_{\tilde{\chi}_2^0}$ is about twice as large as that in Fig. 4.7. This means that the second lightest neutralino is almost the neutral wino. On the other hand, $m_{\tilde{\chi}_3^0}$ and $m_{\tilde{\chi}_4^0}$ extend above 1 TeV because these consist of the neutral Higgsinos. Their masses are given by a μ parameter that is sensitive to m_0 for fixed $m_{\tilde{\chi}_1^0}$. The modulus $|\mu|$ is determined by the EWSB conditions. At tree level, the corresponding formula for the correct EWSB reads

$$|\mu|^2 = \frac{1}{2}\left[\tan 2\beta\left(M_{H_u}^2\tan\beta - M_{H_d}^2\cot\beta\right) - m_Z^2\right], \tag{4-3-3}$$

where M_{H_d} and M_{H_u} are the down-type and up-type Higgs soft SUSY breaking masses. For $\tan\beta \gg 1$, Eq. (4-3-3) is approximated as follows :

$$|\mu|^2 \simeq -M_{H_u}^2. \tag{4-3-4}$$

The soft mass $M_{H_u}^2$ is sensitive to m_0. The approximate solution of the one-loop RGE for $M_{H_u}^2$ is given by

$$\begin{aligned} m_{H_u}^2 \simeq & -3.5\times 10^3\cot^2\beta m_0'^2 \\ & + 87\cot\beta M_{1/2}m_0' - 2.8M_{1/2}^2, \end{aligned} \tag{4-3-5}$$

where $m_0' \equiv m_0 - b$, and b is defined as $b \simeq 5.15\tan\beta + 67.67$(for the lower line) and $4.65\tan\beta + 140.67$(for the upper line) given by Eq. (4-2-1). Therefore, $m_{\tilde{\chi}_3^0}$ and $m_{\tilde{\chi}_4^0}$ become large with increasing m_0.

Meanwhile, the mass of the CP-odd Higgs boson m_A is given by

$$m_A^2 \simeq |\mu|^2. \tag{4-3-6}$$

Thus, the masses of the heavy Higgs boson and the CP-odd Higgs boson are determined by $|\mu|$, and these are close to $m_{\tilde{\chi}_3^0}$ and $m_{\tilde{\chi}_4^0}$ as shown in Figs. 4.7 and 4.9.

First and second generation squarks and sleptons masses

For the first and second generation squarks and sleptons, the effects of the corresponding Yukawa couplings are negligible in RG evolutions of their soft masses. The soft SUSY breaking masses are parametrized up to the one-loop order as [103]

$$m^2_{\tilde{q}_L} \simeq m_0^2 + 4.7M^2_{1/2}, \tag{4-3-7a}$$
$$m^2_{\tilde{q}_R} \simeq m_0^2 + 4.3M^2_{1/2}, \tag{4-3-7b}$$
$$m^2_{\tilde{e}_L} \simeq m_0^2 + 0.5M^2_{1/2}, \tag{4-3-7c}$$
$$m^2_{\tilde{e}_R} \simeq m_0^2 + 0.1M^2_{1/2}. \tag{4-3-7d}$$

Note that the slepton masses are sensitive to m_0 in Fig. 4.8, while the squark masses are insensitive to m_0 in Fig. 4.5. As shown in Fig. 4.3, m_0 is smaller than $M_{1/2}$ in most of the allowed region. Then, in Eqs. (4-3-7a) and (4-3-7b), the second term is dominant, and, hence, we approximate these equations more roughly as follows:

$$\begin{aligned} m_{\tilde{q}_L} &\simeq 2.2M_{1/2}, \\ m_{\tilde{q}_R} &\simeq 2.1M_{1/2}. \end{aligned} \tag{4-3-8}$$

These relations can be clearly seen in Fig. 4.5. The relations lead to the fact that the first and the second generation squarks are always lighter than the gluino, which results in the production cross sections of the squarks are larger than that of the gluino. Meanwhile, in Eqs. (4-3-7c) and (4-3-7d), the contributions to the soft masses from the first term are comparable to those of the second term. Therefore, the slepton masses are sensitive to m_0.

One can see in Fig. 4.5 that the masses of the gluino, sup, and sdown are below 2300 GeV for $\tan\beta = 10,\ 20$, and 30. This light spectrum is the direct consequence of the constraint on the lithium-7 abundance, and, hence, on the neutralino mass. The parameter $M_{1/2}$ is bound below 1.1 TeV. As we will discuss in Sec.4.4, such light spectrum is, indeed, in the range of the 14 TeV run at the LHC, and the order of $100 - 1000$ SUSY events can be expected with luminosity of 100 fb^{-1}.

Stop mass spectra

Figure 4.6 shows the masses of the stops. Unlike in the case of the other sfermions, the distributions of the stop masses are in nonlinear relation. The spread of the distributions in the lightest neutralino mass-stop mass plane is understood as follows.

The masses of the stops in the mass eigenstate are given by

$$\begin{aligned} m^2_{\tilde{t}_1,\tilde{t}_2} \simeq& \frac{1}{2}\left(m^2_{Q_3} + m^2_{U_3}\right) \\ & \mp \frac{1}{2}\sqrt{(m^2_{Q_3} - m^2_{U_3})^2 + 4(m^2_{\tilde{t}_{LR}})^2}, \end{aligned} \tag{4-3-9a}$$
$$m^2_{\tilde{t}_{LR}} = m_t(A_t - \mu\cot\beta), \tag{4-3-9b}$$

where m_{Q_3} and m_{U_3} are the soft SUSY breaking masses, and A_t is the stop trilinear coupling. In Eq. (4-3-9a), the first term is dominant, and it is a decreasing function of m_0^2 because of the top and bottom Yukawa couplings. Meanwhile, the second term in Eq. (4-3-9a) is an increasing function of m_0^2. This is because the dominant term in the square root is $m^2_{\tilde{t}_{LR}}$ involving A_t, and the coupling A_t is proportional to m_0 due to the relation between A_0 and m_0 in Eq. (4-2-1). Hence, for a fixed lightest neutralino mass, stop masses are not simply determined as a function of the lightest neutralino mass; rather, they are spread depending on the m_0^2.

The ATLAS Collaboration gives the bound for the stop mass from the direct stop search at the 8 TeV LHC run [106]. Note that our results of the stop mass are safely above the bound.

We can see in Fig.4.6 that the mass of the lighter stop can be relatively light, 700 to 1400 GeV for 330 to 450 GeV of the lighter stau, respectively. Again, these light spectra come from the bound

on $M_{1/2}$. The mass degeneracy between the stau and the neutralino correlates m_0, A_0, μ, and $\tan\beta$ with $M_{1/2}$ and sets the scale of the SUSY spectrum. As we will see in Sec. 4.4, the production cross sections of such light stop are large and comparable to those of sup and sdown.

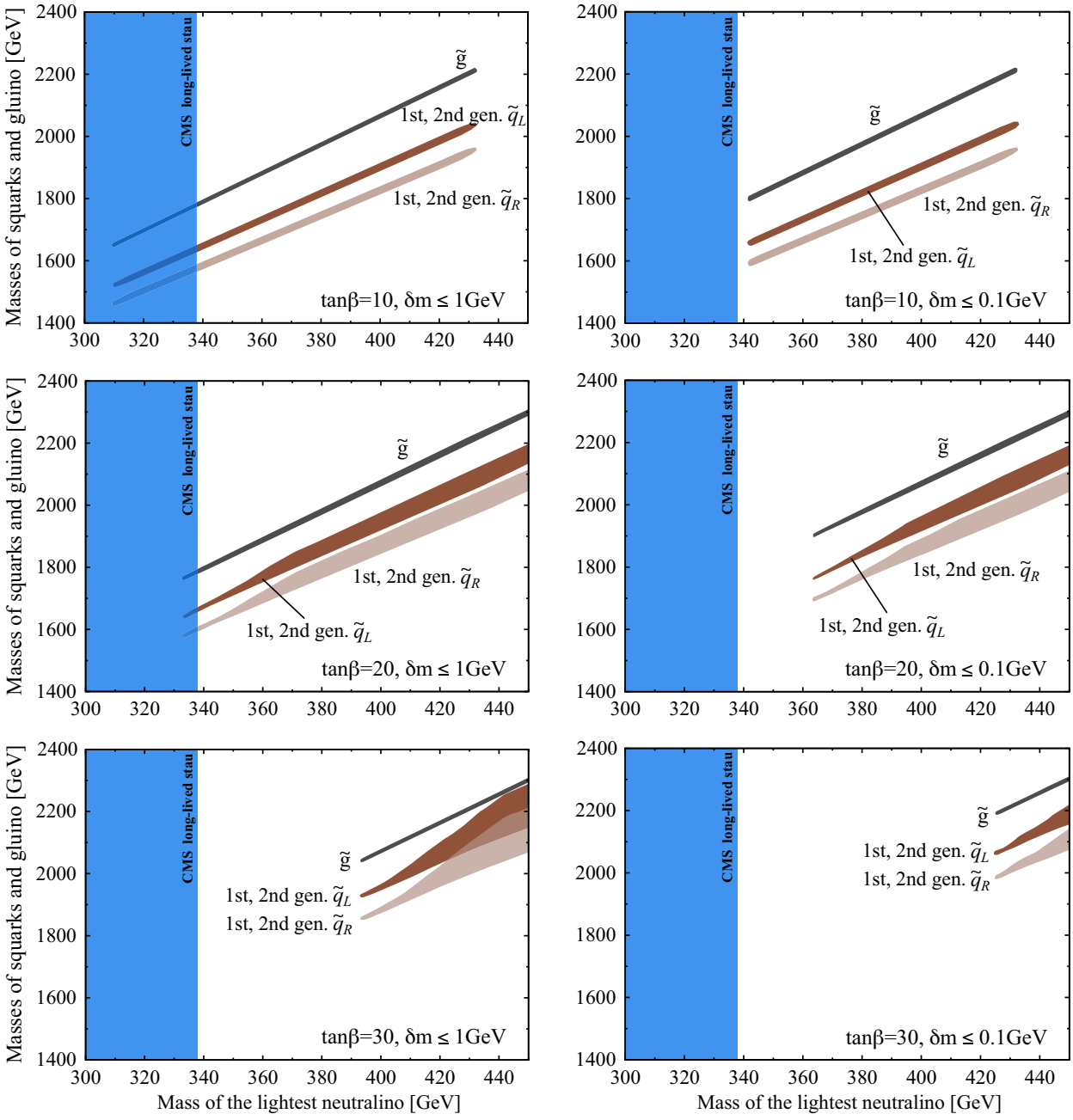

Figure 4.5: The mass spectra of the gluino and the first and second generation squarks. The horizontal axis represents the mass of the LSP neutralino. We fix $\tan\beta$ to 10, 20, and 30 from top to bottom and $\delta m \leq 1$ and 0.1 GeV from left to right, respectively. We have excluded the region with $m_{\tilde{\chi}_1^0} (\simeq m_{\tilde{\tau}_1}) \lesssim 339$ GeV, which is the direct bound on the long-lived CHAMP at the LHC [105].

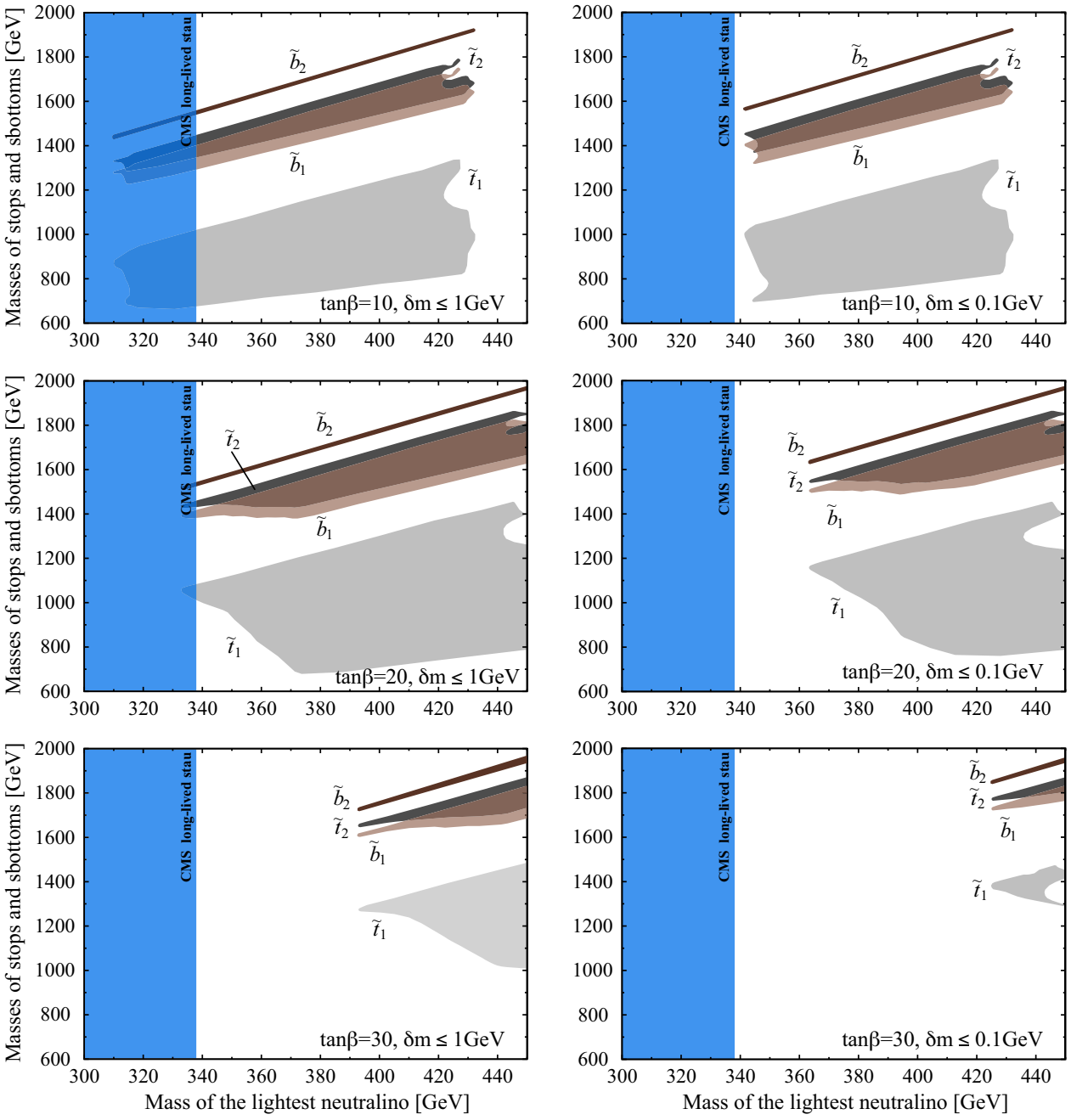

Figure 4.6: The mass spectra of the stop and the sbottom. The horizontal axis expresses the mass of the LSP neutralino. We fix $\tan\beta$ to 10, 20, and 30 from top to bottom and $\delta m \leq 1$ and 0.1 GeV from left to right, respectively. We have excluded the region with $m_{\tilde{\chi}_1^0}(\simeq m_{\tilde{\tau}_1}) \lesssim 339$ GeV, which is the direct bound on the long-lived CHAMP at the LHC [105].

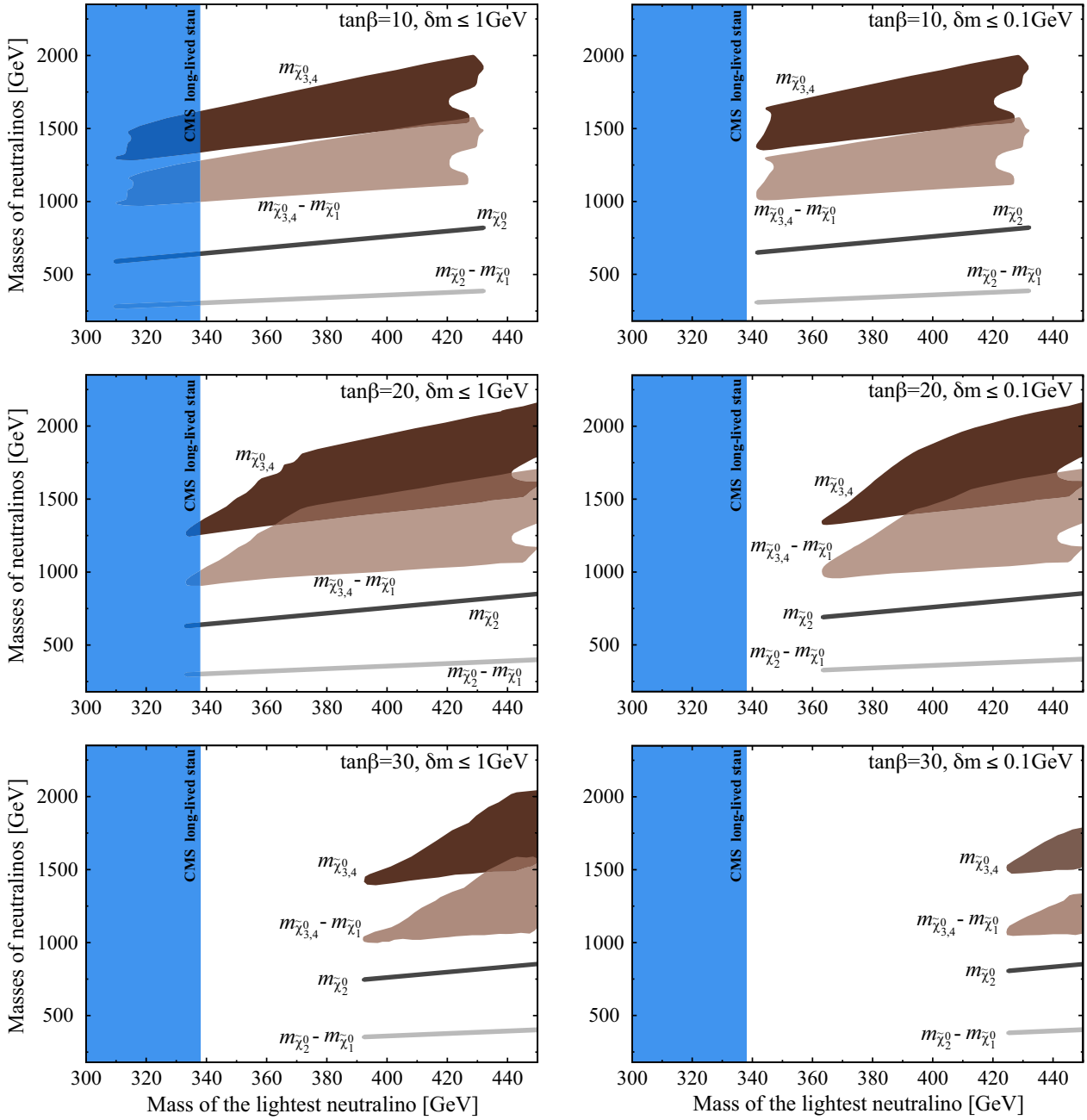

Figure 4.7: The mass spectra of the neutralino. The horizontal axis represents the mass of the LSP neutralino. We fix $\tan\beta$ to 10, 20, and 30 from top to bottom and $\delta m \leq 1$ and 0.1 GeV from left to right, respectively. We have excluded the region with $m_{\tilde{\chi}^0_1}(\simeq m_{\tilde{\tau}_1}) \lesssim 339$ GeV, which is the direct bound on the long-lived CHAMP at the LHC [105].

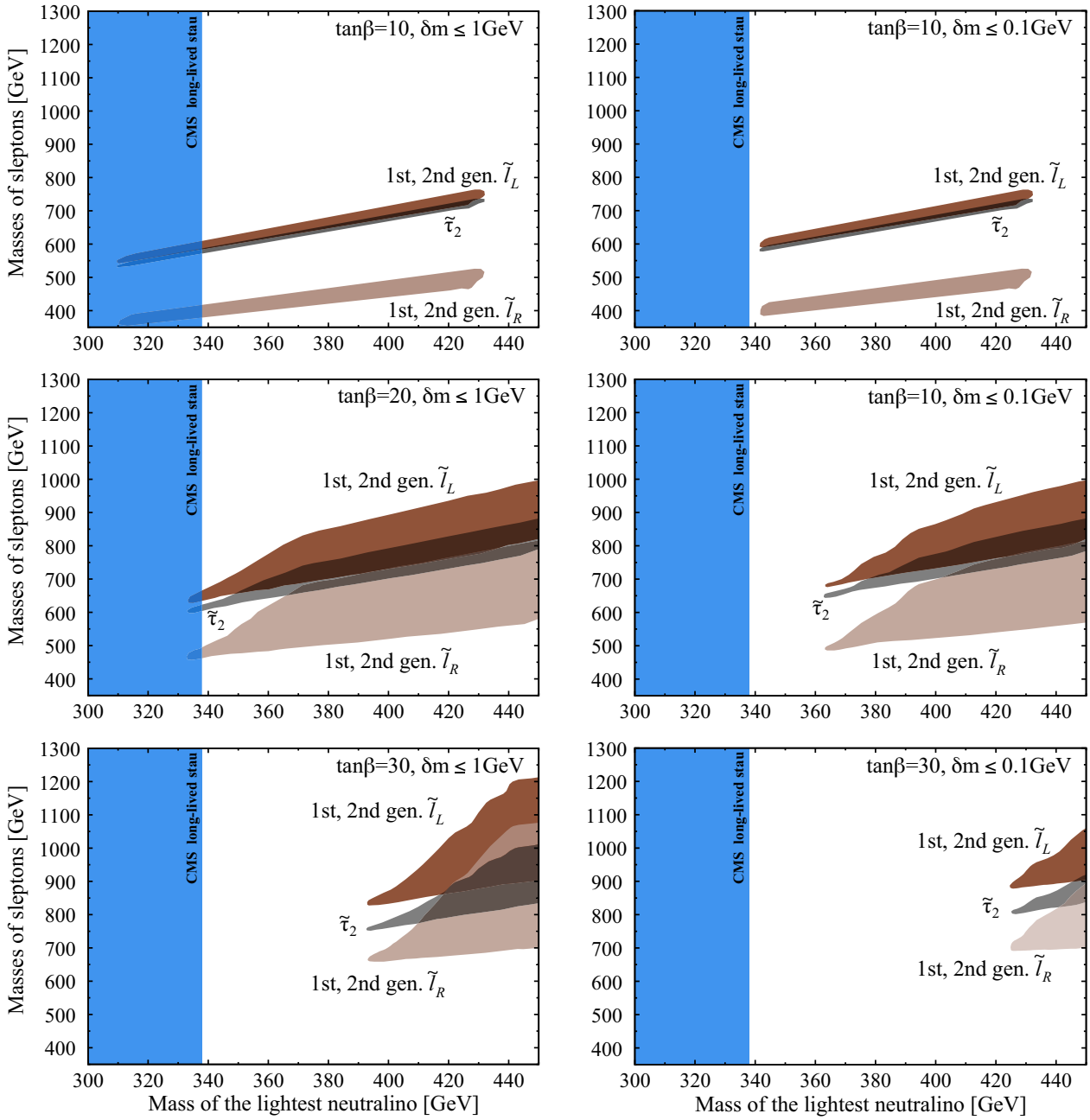

Figure 4.8: The mass spectra of the slepton. The horizontal axis represents the mass of the LSP neutralino. We fix $\tan\beta$ to 10, 20, and 30 from top to bottom and $\delta m \leq 1$ and 0.1 GeV from left to right, respectively. We have excluded the region with $m_{\tilde{\chi}_1^0} (\simeq m_{\tilde{\tau}_1}) \lesssim 339$ GeV, which is the direct bound on the long-lived CHAMP at the LHC [105].

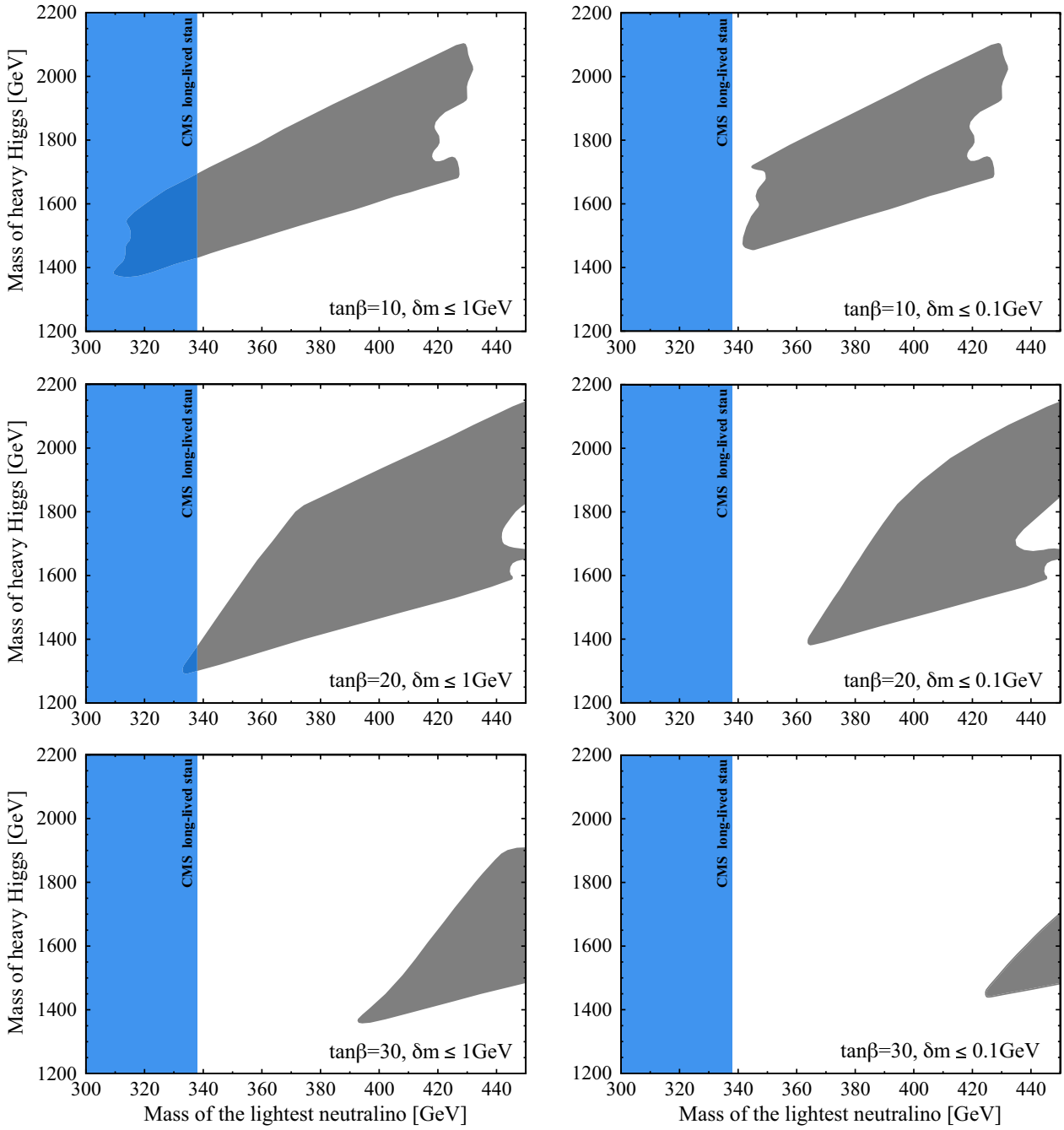

Figure 4.9: The mass spectra of the heavy Higgs boson. The horizontal axis represents the mass of the LSP neutralino. We fix $\tan\beta$ to 10, 20, and 30 from top to bottom and $\delta m \leq 1$ and 0.1 GeV from left to right, respectively. We have excluded the region with $m_{\tilde{\chi}_1^0}(\simeq m_{\tilde{\tau}_1}) \lesssim 339$ GeV, which is the direct bound on the long-lived CHAMP at the LHC [105].

N	$f_{T_u}^{(N)}$	$f_{T_d}^{(N)}$	$f_{T_s}^{(N)}$
p	0.0153	0.0191	0.0447
n	0.011	0.0273	0.0447

Table 4.1: The mass fraction of light quarks in a proton p and a neutron n [90, 113].

4.3.2 Muon $g-2$

We show the muon anomalous magnetic moment, $(g-2)_\mu$, in the allowed region. The latest results on $(g-2)_\mu$ have reported that there is a 3.3σ deviation between the SM prediction and the experimental data [107, 108, 109]:

$$\delta a_\mu = a_\mu^{\rm exp} - a_\mu^{\rm SM} = (26.1 \pm 8.0) \times 10^{-10}, \tag{4-3-10}$$

where $a_\mu \equiv (g-2)_\mu/2$.

For a fixed $\tan\beta$, lighter SUSY particles yield larger contributions. The masses are light as m_0 and $M_{1/2}$ are small. The small m_0 is, however, excluded by the constraint on the Higgs boson mass as shown in Sec. 4.2.2. The sizable contributions to δa_μ are obtained in the regions of small $M_{1/2}$. When we take into account $\delta m \leq 1$ and 0.1 GeV, the dominant SUSY contributions come from the smuon-bino like neutraino loop and the muon sneutrino-charged Higgsino loop. Since we took $\mu > 0$, both contributions are positive. In Fig. 4.10, the SUSY contributions in the allowed region are shown for $\delta m \leq 1$ and 0.1 GeV in the top and bottom panel, respectively. In the panels, $\tan\beta$ is taken to be 10, 20, and 30. It should be noted that the muon anomalous magnetic moment is consistent with current measurements within 3σ levels in this scenario.

4.3.3 Rare decays of B mesons

We show that the branching ratios of $B_s \to \mu^+\mu^-$ and $B \to X_s\gamma$ are consistent with the experimental results.

The evidence for the decay $B_s \to \mu^+\mu^-$ has been discovered by the LHCb Collaboration [110] and the CMS collaboration [111]. The branching ratio has been measured as

$$\mathrm{BR}(B_s \to \mu^+\mu^-) = (3.0^{+1.0}_{-0.9}) \times 10^{-9} \tag{4-3-11}$$

by the CMS Collaboration, and

$$\mathrm{BR}(B_s \to \mu^+\mu^-) = 2.9^{+1.1}_{-1.0}(\mathrm{stat}^{+0.3}_{-0.1}(\mathrm{syst})) \times 10^{-9} \tag{4-3-12}$$

by the LHCb Collaboration. It is also reported by Ref. [112] that the other important rare decay $B \to X_s\gamma$ is strongly suppressed as

$$\mathrm{BR}(B \to X_s\gamma) = (3.43 \pm 0.21 \pm 0.07) \times 10^{-4}. \tag{4-3-13}$$

Figure 4.11 shows the branching ratios of the two rare decays for $\delta m \leq 1$ GeV. The top panel is for $B_s \to \mu^+\mu^-$ and the bottom is for $B_s \to X_s\gamma$. We apply the experimental value reported by the CMS Collaboration in the top panel[111]. One can see that the branching ratios are within the 3σ in our allowed region, and, hence, are consistent with the experiments.

4.3.4 Direct detection of neutralino dark matter

One of the promising approaches to the neutralino dark matter is its direct detection. The scenario we are discussing can be examined by the direct detection measurements combining other measurements for the Higgs boson and the neutralino LSP.

The spin-independent (SI) scatterings are given by the Higgs and squark exchanges. The squark exchange contributions are suppressed by heavy masses of squarks $m_{\tilde{q}}^{-4}$, where $m_{\tilde{q}} \simeq 2$TeV in the

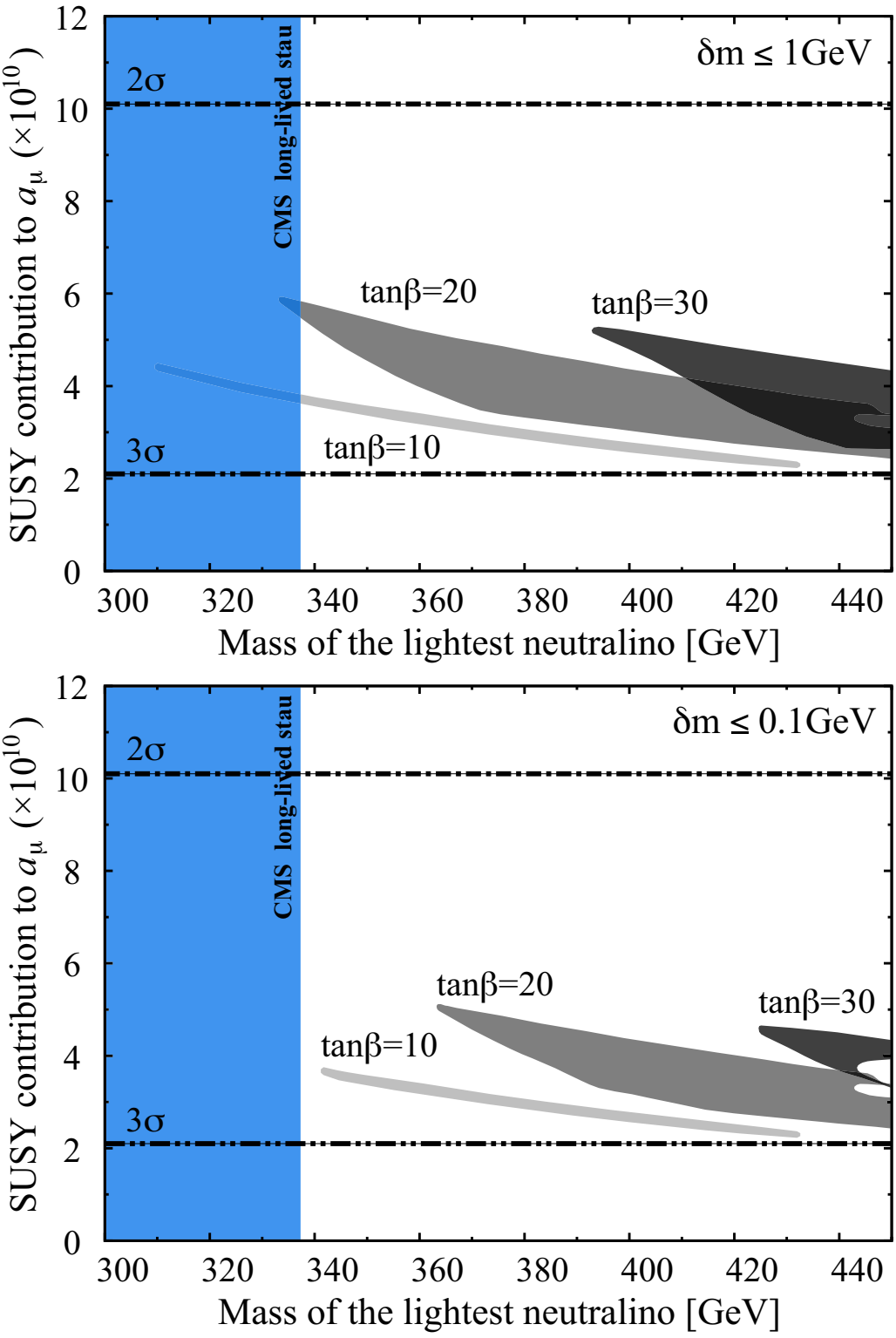

Figure 4.10: The allowed values of δa_μ for the neutralino mass. The upper and lower figures show the results corresponding to the cases of $\delta m \leq 1$ GeV and $\delta m \leq 0.1$ GeV, respectively. We have excluded the region with $m_{\tilde{\chi}_1^0} (\simeq m_{\tilde{\tau}_1}) \lesssim 339$ GeV, which is the direct bound on the long-lived CHAMP at the LHC [105].

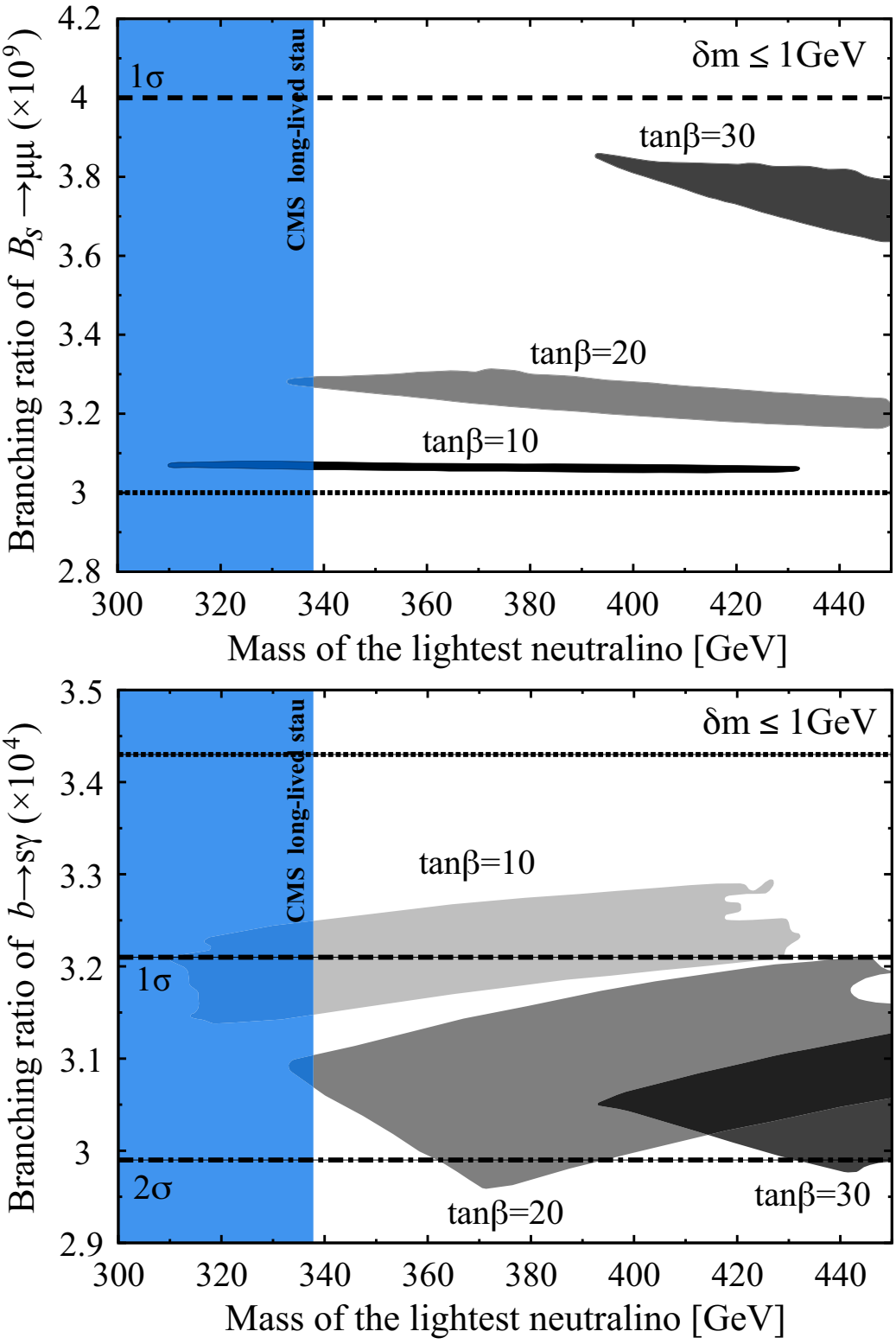

Figure 4.11: The branching ratios of the decay processes of $B_s \to \mu^+\mu^-$ and $B \to X_s\gamma$. We fix $\tan\beta$ to 10, 20, and 30, and $\delta m \leq 1$ GeV. The experimental values are indicated with the horizontal dotted lines. We apply the experimental value reported by the CMS Collaboration in the top panel[111]. We have excluded the region with $m_{\tilde{\chi}_1^0} (\simeq m_{\tilde{\tau}_1}) \lesssim 339$ GeV, which is the direct bound on the long-lived CHAMP at the LHC [105].

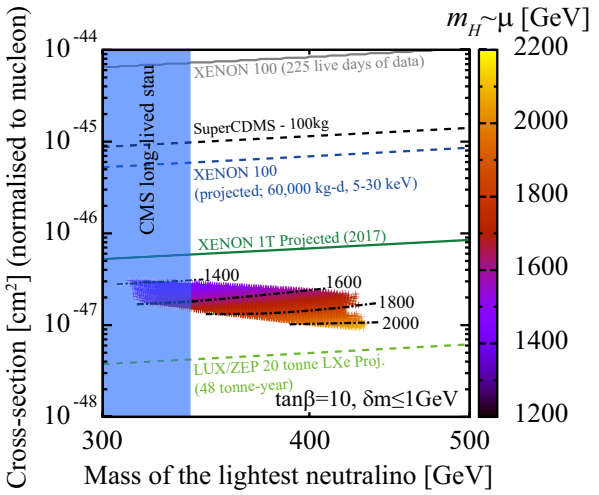

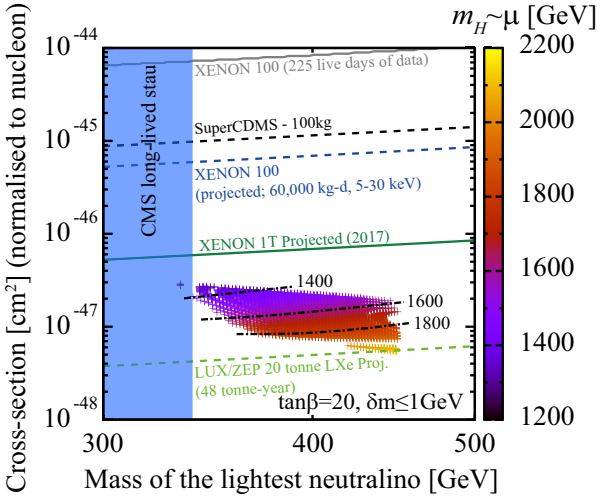

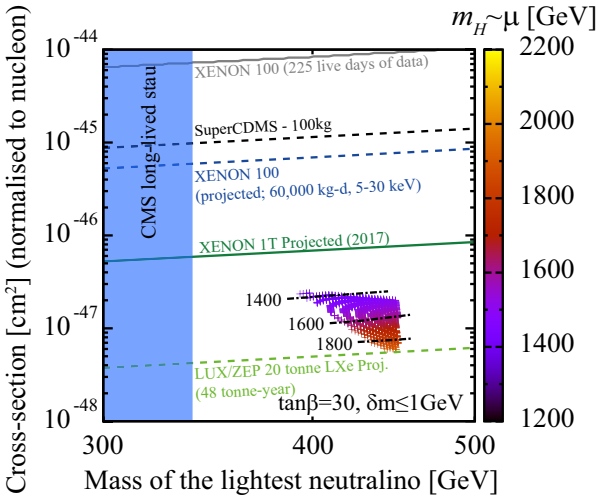

Figure 4.12: Scatter plots of a SI neutralino-nucleon cross section as a function of the mass of the neutralino dark matter. Each curve is shown for the current and future limits. A gradation of colors corresponds to the mass of the heavy Higgs boson. We have excluded the region with $m_{\tilde{\chi}_1^0}(\simeq m_{\tilde{\tau}_1}) \lesssim 339$ GeV, which is the direct bound on the long-lived CHAMP at the LHC [105].

scenario (see Fig. 4.5), and, hence, the SI scattering is dominated by the Higgs exchange contributions. In order to examine the scenario, we have to analyze the dependence of the SI scatterings on the measurements for the Higgs boson and neutralinos. The SI scattering cross section of the neutralino and target nucleon (T) is given by [114]

$$\sigma_{\rm SI} = \frac{4}{\pi}\Big(\frac{m_{\tilde{\chi}_1^0} m_T}{m_{\tilde{\chi}_1^0} + m_T}\Big)^2 (n_p f_p + n_n f_n)^2, \tag{4-3-14}$$

where m_T is the mass of the target nucleus. The symbol $n_p(n_n)$ is the number of protons (neutrons) in the target nucleus, and the effective coupling of the neutralino to a proton f_p is given as

$$\begin{aligned} f_p &= \sum_q f_q \langle p|\bar{q}q|p\rangle \\ &= \sum_{q=u,d,s} \frac{f_q}{m_q} m_p f_{T_q}^{(p)} + \frac{2}{27} f_{T_G} \sum_{q=c,b,t} \frac{f_q}{m_q} m_p, \end{aligned} \tag{4-3-15}$$

where $f_{Tq}^{(p)} \equiv \langle p|m_q \bar{q}q|p\rangle/m_p$ is the mass fraction of light quarks in a proton (listed in Table I), and $f_{T_G} = 1 - \sum_{u,d,s} f_{T_q}^{(p)}$. For the neutron, f_n is derived in the same manner. The effective coupling of the neutralino to quarks f_q is calculated as follows:

$$f_q = m_q \frac{g_2^2}{4 m_W}\Big(\frac{C_{h\tilde{\chi}_1^0\tilde{\chi}_1^0} C_{hqq}}{m_h^2} + \frac{C_{H\tilde{\chi}_1^0\tilde{\chi}_1^0} C_{Hqq}}{m_H^2}\Big). \tag{4-3-16}$$

Here, C_{hqq} and C_{Hqq} are the Yukawa couplings of the lighter and heavier Higgs bosons and quarks (detailed formulas are given in Ref. [114]). For the bino-like neutralino LSP ($M_1 \ll M_2, \mu$), the coupling of the neutralino and the Higgs bosons, $C_{h\tilde{\chi}_1^0\tilde{\chi}_1^0}$ and $C_{H\tilde{\chi}_1^0\tilde{\chi}_1^0}$, is perturbatively calculated as follows:

$$\begin{aligned} C_{h\tilde{\chi}_1^0\tilde{\chi}_1^0} &\simeq \frac{m_Z \sin\theta_W \tan\theta_W}{M_1^2 - \mu^2}[M_1 \sin\beta + \mu\cos\beta], \\ C_{H\tilde{\chi}_1^0\tilde{\chi}_1^0} &\simeq \frac{m_Z \sin\theta_W \tan\theta_W}{M_1^2 - \mu^2}\mu \sin\beta. \end{aligned} \tag{4-3-17}$$

In the scenario, the mass of the heavier CP-even Higgs boson is much larger than the mass of the lighter Higgs boson (see Fig. 4.9), and, therefore, the contribution from the H exchange is negligible.

Figure 4.12 shows the SI scattering cross section in the allowed region as a function of the mass of the neutralino dark matter for $\delta m \leq 1$ GeV, and $\tan\beta$ is taken to be 10, 20, and 30 from the upper panel to the lower one. The curves represent the current limit [115] and future limit [116, 117]. The colors correspond to the mass of the heavier CP-even Higgs boson.

In Fig. 4.12, we can see that the SI scattering cross section is smaller as $\tan\beta$ and/or the neutralino mass is larger. Such behavior can be easily understood by Eq.(4-3-17). We can also see from the contour lines that the lighter mass of the heavy Higgs boson leads to larger SI cross sections for all $\tan\beta$. This is understood as follows. The mass of the heavy Higgs boson is determined by the condition of the radiative electroweak symmetry breaking in the scenario and is almost equal to $m_H \simeq \mu$ (see the discussion in Sec. 4.3.1). As is given in Eq. (4-3-17), a smaller μ makes the neutralino mixing value larger, and, hence, large couplings between the neutralino dark matter and the Higgs bosons are obtained. Thus a clear correlation of the mass of the heavy Higgs boson and the cross section appears.

In the end, one can see that future direct detection experiments will reach the sensitivity to detect the neutralino dark matter in the scenario. The mass of the heavy Higgs boson can be estimated from the measurements of the cross section and the mass of the neutralino at the direct detection and the LHC experiments. Thus the interplay of both experiments will play important roles to examine our scenario.

4.4 Direct search at the LHC

Here we show the expected number of events of the long-lived stau and the neutralino at the LHC experiment with center-of-mass energy 14 TeV and luminosity 100 fb^{-1} and discuss the feasibility of the verification of the scenario.

We choose 12 sets of the CMSSM parameters in the allowed region for $\tan\beta = 10,\ 20$, and 30. The parameters of the sample points and the mass spectrum of the SUSY particles are shown in Tables 4.2, 4.8, and 4.14. These points correspond to the mass of the neutralino, 350, 375, 400, and 425 GeV for $\tan\beta = 10$, 350, 375, 400, 425, and 450 GeV for $\tan\beta = 20$, and 400, 425, and 450 GeV for $\tan\beta = 30$, respectively. We calculate the branching ratios and the pair production cross sections of the SUSY particles with CalcHEP 3.4 [118] implementing SPheno [97, 98]. The branching ratios are shown in Tables 4.3, 4.4, 4.9, 4.10, 4.15, and 4.16. The first column is the parent particles and the second one is the final states. The production cross sections of the SUSY particles are shown in Tables 4.5, 4.6, 4.11, 4.12, 4.17, and 4.18. The first column $\sigma(a, b)$ is the production cross sections of particles a and b from p-p collision with the center-of-mass energy 14TeV. The last rows of Tables 4.6, 4.12, and 4.18, σ (all SUSY) is the sum of the production cross sections of SUSY particles.

Using the numbers given in the tables, we calculate the number of the stau from SUSY cascade decays and direct productions. The branching fraction of the cascade decays of a SUSY particle $\tilde{\psi}$ to the stau is denoted as $\mathrm{BR}(\tilde{\psi} \to \tilde{\tau}_1)$. The symbol $\sigma(\tilde{\psi})$ represents the sum of the cross sections of the SUSY particles. Then, the effective total production cross section of the stau is

$$\sigma(\tilde{\tau}_1^{(*)}) = \sum_{\tilde{\psi}}^{\text{all SUSY}} \sigma(\tilde{\psi}) \times \mathrm{BR}(\tilde{\psi} \to \tilde{\tau}_1^{(*)}). \tag{4-4-1}$$

Since the long-lived staus penetrate the LHC detectors, the number of missing energy events is calculated as follows:

$$N(\tilde{\chi}_1^0) = \left\{\sigma(\text{all SUSY}) - \sigma(\tilde{\tau}_1) - \sigma(\tilde{\tau}_1^*)\right\} \times \mathcal{L}_{\text{int}}, \tag{4-4-2}$$

where $\mathcal{L}_{\text{int}}$ is the integrated luminosity. Assuming the integrated luminosity is $\mathcal{L}_{\text{int}} = 100\text{fb}^{-1}$, the expected number of staus and neutralinos is 1570 and 7200 for $m_{\tilde{\tau}_1} = 350$ GeV and 490 and 2100 for $m_{\tilde{\tau}_1} = 425$ GeV for $\tan\beta = 10$ (see Table 4.7), 4270 and 3680 for $m_{\tilde{\tau}_1} = 350$ GeV and 790 and 940 for $m_{\tilde{\tau}_1} = 450$ GeV for $\tan\beta = 20$ (see Table 4.13), 1810 and 1210 for $m_{\tilde{\tau}_1} = 400$ GeV and 790 and 590 for $m_{\tilde{\tau}_1} = 450$ GeV for $\tan\beta = 30$ (see Table 4.19), respectively. Since the stau is very long-lived in our scenario, it penetrates the detectors leaving the charged tracks. One can expect that such long-lived stau can be identified easily, and its mass as well as the production cross section of relatively lighter sup and sdown will be measured. Thus, the number of the events will be sufficient to compare the predictions with measurements.[3]

In Tables 4.6, 4.12, and 4.18, one can see that the production cross sections of the stops are comparable to those of gluino and light squarks. Those are obtained as 5.57 fb for $m_{\tilde{\tau}_1} = 350$ GeV and 1.76 fb for $m_{\tilde{\tau}_1} = 425$ GeV for $\tan\beta = 10$; 4.40 fb for $m_{\tilde{\tau}_1} = 350$ GeV and 2.66 fb for $m_{\tilde{\tau}_1} = 450$ GeV for $\tan\beta = 20$; 0.47 fb for $m_{\tilde{\tau}_1} = 400$ GeV and 1.24 fb for $m_{\tilde{\tau}_1} = 450$ GeV for $\tan\beta = 30$. It is important to emphasize here that such production cross sections of stops are the results of our constraint that leads to a relatively heavy SUSY spectrum.

The predictions presented here are based on the CMSSM framework by requiring the constraints on the relic abundance of lithium-7, dark matter, and Higgs mass. In this scenario, the masses, hence, the production cross sections, of the sup, sdown, and gluino have clear relations with that of the stau. Such relations enable us to examine our scenario. Therefore, the early discovery of the long-lived stau and the light stop at the 14 TeV run is the important prediction in our scenario.

[3]The efficiency to identify the stau and the neutralino with 350 and 450 GeV is about $\mathcal{O}(10)\%$ in Ref. [105]. Thus, it is possible to examine our scenario with $\mathcal{L}_{\text{int}} = 100$ fb^{-1}. Detailed simulation is beyond the scope of this paper and is left for our future work.

Input parameters	Point 1 (GeV)	Point 2 (GeV)	Point 3 (GeV)	Point 4 (GeV)
$M_{1/2}$	822.0	878.0	934.0	990.0
m_0	266.0	285.0	302.0	325.0
A_0	-2264.5	-2418.7	-2540.6	-2759.9
Particle				
h	123.7	124.1	124.4	124.8
H	1581.7	1684.0	1777.8	1895.9
A	1582.3	1684.5	1778.2	1896.4
$H^{\pm}$	1584.6	1686.7	1780.3	1898.4
$\tilde{g}$	1823.0	1937.7	2052.0	2165.8
$\tilde{\chi}_1^{\pm}$	665.2	711.9	758.5	805.2
$\tilde{\chi}_2^{\pm}$	1492.1	1586.7	1672.3	1784.0
$\tilde{\chi}_1^0$	349.6	374.6	399.6	424.8
$\tilde{\chi}_2^0$	665.0	711.7	758.3	805.2
$\tilde{\chi}_3^0$	1488.0	1582.9	1668.5	1780.5
$\tilde{\chi}_4^0$	1491.5	1586.3	1671.8	1783.8
$\tilde{e}_L$	611.3	652.4	692.6	735.5
$\tilde{e}_R$	409.2	437.2	463.9	494.5
$\tilde{\nu}_e$	606.0	647.4	687.9	731.0
$\tilde{\tau}_1$	350.3	375.3	400.1	425.3
$\tilde{\tau}_2$	597.5	637.3	676.6	717.5
$\tilde{\nu}_\tau$	588.7	629.1	668.8	710.1
$\tilde{u}_L$	1678.3	1783.4	1887.6	1992.4
$\tilde{u}_R$	1611.8	1712.0	1811.3	1911.3
$\tilde{d}_L$	1680.0	1785.0	1889.1	1993.8
$\tilde{d}_R$	1604.8	1704.4	1803.1	1902.5
$\tilde{t}_1$	913.8	971.8	1038.7	1075.8
$\tilde{t}_2$	1436.3	1519.6	1605.6	1682.4
$\tilde{b}_1$	1389.9	1475.5	1563.8	1642.3
$\tilde{b}_2$	1583.0	1681.1	1778.6	1875.9

Table 4.2: Input parameters and the mass spectrum of sample points. The value of $\tan\beta$ is fixed to 10 and $\text{sign}(\mu) > 0$. We choose these parameters as the $m_{\tilde{\chi}_1^0}$ is fixed to 350, 375, 400, and 425 GeV, respectively.

Particle	Final states	Point 1 (%)	Point 2 (%)	Point 3 (%)	Point 4 (%)
$\tilde{g}$	$\bar{t}, \tilde{t}_1$	20.7	20.7	20.6	20.9
	$t, \tilde{t}_1^*$	20.7	20.7	20.6	20.9
	$\bar{b}, \tilde{b}_1$	7.4	7.4	7.3	7.3
	$b, \tilde{b}_1^*$	7.4	7.4	7.3	7.3
	$\bar{t}, \tilde{t}_2$	7.1	7.2	7.2	7.2
	$t, \tilde{t}_2^*$	7.1	7.2	7.2	7.2
	$\bar{b}, \tilde{b}_2$	2.6	2.6	2.6	2.5
	$b, \tilde{b}_2^*$	2.6	2.6	2.6	2.5
$\tilde{u}_L$	$d, \tilde{\chi}_1^+$	65.8	65.8	65.7	65.7
	$u, \tilde{\chi}_2^0$	32.9	32.9	32.9	32.9
	$u, \tilde{\chi}_1^0$	1.4	1.4	1.4	1.4
$\tilde{d}_L$	$u, \tilde{\chi}_1^-$	65.6	65.6	65.6	65.6
	$d, \tilde{\chi}_2^0$	32.8	32.8	32.8	32.8
	$d, \tilde{\chi}_1^0$	1.5	1.5	1.5	1.5
$\tilde{t}_1$	$t, \tilde{\chi}_1^0$	80.7	82.7	83.7	86.5
	$b, \tilde{\chi}_1^+$	14.3	12.8	11.8	9.8
	$t, \tilde{\chi}_2^0$	4.9	4.6	4.5	3.7
$\tilde{t}_2$	$Z, \tilde{t}_1$	43.1	42.7	42.1	42.4
	$h, \tilde{t}_1$	30.4	31.2	31.7	32.8
	$b, \tilde{\chi}_1^+$	17.3	17.0	17.1	16.2
	$t, \tilde{\chi}_2^0$	8.2	8.1	8.2	7.8
$\tilde{b}_1$	$W^-, \tilde{t}_1$	73.4	73.8	73.7	75.2
	$t, \tilde{\chi}_1^-$	17.1	16.8	17.0	16.0
	$b, \tilde{\chi}_2^0$	9.1	8.9	8.9	8.4
$\tilde{b}_2$	$b, \tilde{\chi}_1^0$	57.2	58.2	59.5	59.6
	$W^-, \tilde{t}_1$	26.2	24.0	22.1	20.4
	$h, \tilde{b}_1$	6.4	6.8	6.9	7.5
	$Z, \tilde{b}_1$	4.1	4.4	4.5	5.0
	$W^-, \tilde{t}_2$	3.0	3.7	4.3	5.3
	$t, \tilde{\chi}_1^-$	1.6	1.4	1.3	1.1
$\tilde{\nu}_\tau$	$W^+, \tilde{\tau}_1$	62.0	62.7	63.0	63.9
	$\nu_\tau, \tilde{\chi}_1^0$	38.0	37.3	37.0	36.1
$\tilde{\tau}_2$	$Z, \tilde{\tau}_1$	30.0	30.3	30.5	30.9
	$h, \tilde{\tau}_1$	32.2	32.5	32.8	33.2
	$\tau, \tilde{\chi}_1^0$	37.9	37.1	36.8	35.8
$\tilde{\chi}_2^0$	$\bar{\nu}_\tau, \tilde{\nu}_\tau$	11.5	11.4	11.3	11.3
	$\nu_\tau, \tilde{\nu}_*^*$	11.5	11.4	11.3	11.3
	$\bar{\tau}, \tilde{\tau}_2$	9.1	9.3	9.5	9.7
	$\tau, \tilde{\tau}_2^*$	9.1	9.3	9.5	9.7
	$\bar{\nu}_e, \tilde{\nu}_e/\bar{\nu}_\mu, \tilde{\nu}_\mu$	7.1	7.1	7.2	7.1
	$\nu_e, \tilde{\nu}_e^*/\nu_\mu, \tilde{\nu}_\mu^*$	7.1	7.1	7.2	7.1
	$\bar{e}, \tilde{e}/\bar{\mu}, \tilde{\mu}$	6.0	6.2	6.4	6.4
	$e, \tilde{e}^*/\mu, \tilde{\mu}^*$	6.0	6.2	6.4	6.4
	$\bar{\tau}, \tilde{\tau}_1$	2.8	2.4	2.0	1.8
	$\tau, \tilde{\tau}_1^*$	2.8	2.4	2.0	1.8

Table 4.3: Branching ratios of the SUSY particles on the sample points for $\tan\beta = 10$.

Particle	Final states	Point 1 (%)	Point 2 (%)	Point 3 (%)	Point 4 (%)
$\tilde{\chi}_3^0$	$\bar{t}, \tilde{t}_1$	24.7	24.9	24.6	25.8
	$t, \tilde{t}_1^*$	24.7	24.9	24.6	25.8
	$W^-, \tilde{\chi}_1^+$	14.8	14.7	14.9	14.2
	$W^+, \tilde{\chi}_1^-$	14.8	14.7	14.9	14.2
	$Z, \tilde{\chi}_2^0$	13.3	13.2	13.4	12.8
	$Z, \tilde{\chi}_1^0$	4.0	4.0	4.1	3.9
	$h, \tilde{\chi}_2^0$	1.3	1.3	1.3	1.3
$\tilde{\chi}_4^0$	$\bar{t}, \tilde{t}_1$	28.5	28.3	27.8	28.4
	$t, \tilde{t}_1^*$	28.5	28.3	27.8	28.4
	$W^-, \tilde{\chi}_1^+$	12.3	12.4	12.8	12.4
	$W^+, \tilde{\chi}_1^-$	12.3	12.4	12.8	12.4
	$h, \tilde{\chi}_2^0$	11.6	11.8	12.2	11.9
	$h, \tilde{\chi}_1^0$	3.1	3.2	3.3	3.2
	$Z, \tilde{\chi}_2^0$	1.1	1.1	1.1	1.1
$\tilde{\chi}_1^+$	$\bar{\tau}, \tilde{\nu}_\tau$	23.3	23.1	22.7	22.8
	$\nu_\tau, \tilde{\tau}_2^*$	18.0	18.4	18.7	19.2
	$\bar{e}, \tilde{\nu}_e / \bar{\mu}, \tilde{\nu}_\mu$	14.4	14.4	14.5	14.3
	$\nu_e, \tilde{e}_L^* / \nu_\mu, \tilde{\mu}_L^*$	11.9	12.3	12.6	12.7
	$\nu_\tau, \tilde{\tau}_1^*$	5.5	4.7	4.0	3.6
$\tilde{\chi}_2^+$	$\bar{b}, \tilde{t}_1$	51.4	51.5	50.7	52.5
	$h, \tilde{\chi}_1^+$	14.3	14.4	14.6	14.1
	$Z, \tilde{\chi}_1^+$	13.8	13.8	14.0	13.5
	$W^+, \tilde{\chi}_2^0$	14.0	14.0	14.2	13.7
	$W^+, \tilde{\chi}_1^0$	4.5	4.5	4.6	4.5
H	b, b	49.0	48.6	48.4	47.6
	$t, \bar{t}$	19.4	19.4	19.3	19.1
	$\tau, \bar{\tau}$	8.6	8.5	8.5	8.5
	h, h	3.4	3.8	4.2	4.7
	$\tilde{\tau}_1, \tilde{\tau}_2^*$	8.2	8.3	8.2	8.5
	$\tilde{\tau}_1^*, \tilde{\tau}_2$	8.2	8.3	8.2	8.5
A	b, b	50.1	50.1	50.3	49.9
	$t, \bar{t}$	18.8	18.8	18.9	18.8
	$\tau, \bar{\tau}$	8.7	8.8	8.9	8.9
	$\tilde{\tau}_1, \tilde{\tau}_2^*$	9.0	9.1	9.1	9.4
	$\tilde{\tau}_1^*, \tilde{\tau}_2$	9.0	9.1	9.1	9.4
H^+	b, t	72.1	71.9	71.9	71.4
	$\tilde{\tau}_1^*, \tilde{\nu}_\tau$	17.5	17.7	17.6	18.1
	$\bar{\tau}, \nu_\tau$	8.6	8.6	8.7	8.6

Table 4.4: Branching ratios of the SUSY particles on the sample points for $\tan\beta = 10$.

Cross section	Point 1 (fb)	Point 2 (fb)	Point 3 (fb)	Point 4 (fb)
$\sigma(\tilde{u}_L, \tilde{u}_L)$	3.285	2.253	1.554	1.072
$\sigma(\tilde{u}_L, \tilde{u}_R)$	1.856	1.214	0.800	0.528
$\sigma(\tilde{u}_R, \tilde{u}_R)$	3.366	2.332	1.628	1.137
$\sigma(\tilde{d}_L, \tilde{d}_L)$	0.434	0.279	0.181	0.117
$\sigma(\tilde{d}_L, \tilde{d}_R)$	0.220	0.135	0.084	0.052
$\sigma(\tilde{d}_R, \tilde{d}_R)$	0.442	0.288	0.189	0.124
$\sigma(\tilde{u}_L, \tilde{d}_L)$	3.697	2.469	1.657	1.113
$\sigma(\tilde{u}_L, \tilde{d}_R)$	0.625	0.397	0.254	0.163
$\sigma(\tilde{u}_R, \tilde{d}_L)$	0.618	0.392	0.230	0.160
$\sigma(\tilde{u}_R, \tilde{d}_R)$	3.068	2.065	1.400	0.951
$\sigma(\tilde{g}, \tilde{u}_L)$	2.935	1.717	1.016	0.606
$\sigma(\tilde{g}, \tilde{u}_R)$	3.407	2.009	1.199	0.720
$\sigma(\tilde{g}, \tilde{d}_L)$	0.891	0.506	0.290	0.168
$\sigma(\tilde{g}, \tilde{d}_R)$	1.063	0.610	0.354	0.207
$\sigma(\tilde{g}, \tilde{g})$	0.444	0.232	0.123	0.065
$\sigma(\tilde{u}_L, \tilde{u}_L^*)$	0.090	0.051	0.029	0.017
$\sigma(\tilde{u}_L, \tilde{u}_R^*)$	0.257	0.160	0.101	0.063
$\sigma(\tilde{u}_R, \tilde{u}_L^*)$	0.257	0.160	0.101	0.063
$\sigma(\tilde{u}_R, \tilde{u}_R^*)$	0.130	0.076	0.046	0.027
$\sigma(\tilde{d}_L, \tilde{d}_L^*)$	0.063	0.035	0.021	0.011
$\sigma(\tilde{d}_L, \tilde{d}_R^*)$	0.095	0.055	0.032	0.019
$\sigma(\tilde{d}_R, \tilde{d}_L^*)$	0.095	0.055	0.032	0.019
$\sigma(\tilde{d}_R, \tilde{d}_R^*)$	0.094	0.048	0.030	0.019
$\sigma(\tilde{u}_L, \tilde{d}_R^*)$	0.300	0.180	0.104	0.066
$\sigma(\tilde{u}_R, \tilde{d}_L^*)$	0.294	0.176	0.106	0.064
$\sigma(\tilde{u}_L, \tilde{d}_L^*)$	0.040	0.026	0.013	0.007
$\sigma(\tilde{u}_R, \tilde{d}_R^*)$	0.065	0.037	0.022	0.013
$\sigma(\tilde{d}_L, \tilde{u}_L^*)$	0.011	0.006	0.003	0.002
$\sigma(\tilde{d}_R, \tilde{u}_L^*)$	0.081	0.049	0.030	0.018
$\sigma(\tilde{d}_L, \tilde{u}_R^*)$	0.080	0.048	0.029	0.017
$\sigma(\tilde{d}_R, \tilde{u}_R^*)$	0.018	0.010	0.006	0.004
$\sigma(\tilde{g}, \tilde{u}_L^*)$	0.055	0.030	0.016	0.009
$\sigma(\tilde{g}, \tilde{u}_R^*)$	0.066	0.036	0.020	0.011
$\sigma(\tilde{g}, \tilde{d}_L^*)$	0.050	0.025	0.013	0.007
$\sigma(\tilde{g}, \tilde{d}_R^*)$	0.062	0.032	0.016	0.009

Table 4.5: Cross sections of SUSY particles on the sample points for $\tan\beta = 10$. We assume the energy in the center-of-mass system as 14 TeV at the LHC experiment.

Cross section	Point 1 (fb)	Point 2 (fb)	Point 3 (fb)	Point 4 (fb)
$\sigma(\tilde{t}_1, \tilde{t}_1^*)$	5.565	3.637	2.264	1.757
$\sigma(\tilde{t}_2, \tilde{t}_2^*)$	0.186	0.111	0.071	0.046
$\sigma(\tilde{b}_1, \tilde{b}_1^*)$	0.245	0.148	0.089	0.058
$\sigma(\tilde{b}_2, \tilde{b}_2^*)$	0.080	0.046	0.028	0.014
$\sigma(\tilde{\chi}_2^0, \tilde{\chi}_2^0)$	0.106	0.075	0.054	0.038
$\sigma(\tilde{\chi}_1^0, \tilde{\chi}_2^0)$	0.015	0.011	0.008	0.006
$\sigma(\tilde{\chi}_1^0, \tilde{\chi}_1^0)$	0.109	0.083	0.062	0.048
$\sigma(\tilde{\chi}_2^0, \tilde{g})$	0.207	0.132	0.085	0.056
$\sigma(\tilde{\chi}_1^0, \tilde{g})$	0.235	0.157	0.106	0.072
$\sigma(\tilde{\chi}_1^+, \tilde{\chi}_1^-)$	2.406	1.726	1.254	0.922
$\sigma(\tilde{\chi}_1^+, \tilde{\chi}_2^0)$	3.416	2.489	1.834	1.363
$\sigma(\tilde{\chi}_1^-, \tilde{\chi}_2^0)$	1.200	0.849	0.610	0.443
$\sigma(\tilde{\chi}_1^+, \tilde{\chi}_1^0)$	0.025	0.018	0.013	0.010
$\sigma(\tilde{\chi}_1^-, \tilde{\chi}_1^0)$	0.008	0.006	0.004	0.003
$\sigma(\tilde{\chi}_1^+, \tilde{g})$	0.355	0.224	0.143	0.092
$\sigma(\tilde{\chi}_1^-, \tilde{g})$	0.097	0.061	0.039	0.025
$\sigma(\tilde{\tau}_1, \tilde{\tau}_1^*)$	0.853	0.645	0.494	0.381
$\sigma(\tilde{\tau}_1, \tilde{\tau}_2^*)$	0.008	0.005	0.003	0.001
$\sigma(\tilde{\tau}_2, \tilde{\tau}_1^*)$	0.008	0.005	0.003	0.001
$\sigma(\tilde{\tau}_2, \tilde{\tau}_2^*)$	0.187	0.136	0.102	0.076
σ(all SUSY)	43.881	28.767	19.000	13.001

Table 4.6: Cross sections of SUSY particles on the sample points for $\tan\beta = 10$. We assume the energy in the center-of-mass system as 14 TeV at the LHC experiment.

Cross section ×branching ratio	Point 1 (fb)	Point 2 (fb)	Point 3 (fb)	Point 4 (fb)
$\sigma(\tilde{g}) \times \mathrm{BR}(\tilde{g} \to \tilde{\tau}_1)$	0.430	0.235	0.134	0.073
$\sigma(\tilde{g}) \times \mathrm{BR}(\tilde{g} \to \tilde{\tau}_1^*)$	0.430	0.235	0.134	0.073
$\sigma(\tilde{u}_L) \times \mathrm{BR}(\tilde{u}_L \to \tilde{\tau}_1)$	2.394	1.565	1.012	0.678
$\sigma(\tilde{u}_L) \times \mathrm{BR}(\tilde{u}_L \to \tilde{\tau}_1^*)$	2.735	1.692	1.087	0.719
$\sigma(\tilde{d}_L) \times \mathrm{BR}(\tilde{d}_L \to \tilde{\tau}_1)$	1.051	0.661	0.415	0.274
$\sigma(\tilde{d}_L) \times \mathrm{BR}(\tilde{d}_L \to \tilde{\tau}_1^*)$	0.955	0.612	0.388	0.259
$\sigma(\tilde{t}_1) \times \mathrm{BR}(\tilde{t}_1 \to \tilde{\tau}_1)$	0.157	0.093	0.054	0.035
$\sigma(\tilde{t}_1) \times \mathrm{BR}(\tilde{t}_1 \to \tilde{\tau}_1^*)$	0.175	0.101	0.058	0.037
$\sigma(\tilde{t}_2) \times \mathrm{BR}(\tilde{t}_2 \to \tilde{\tau}_1)$	0.011	0.007	0.004	0.003
$\sigma(\tilde{t}_2) \times \mathrm{BR}(\tilde{t}_2 \to \tilde{\tau}_1^*)$	0.013	0.007	0.004	0.003
$\sigma(\tilde{b}_1) \times \mathrm{BR}(\tilde{b}_1 \to \tilde{\tau}_1)$	0.016	0.009	0.005	0.003
$\sigma(\tilde{b}_1) \times \mathrm{BR}(\tilde{b}_1 \to \tilde{\tau}_1^*)$	0.015	0.009	0.005	0.003
$\sigma(\tilde{b}_2) \times \mathrm{BR}(\tilde{b}_2 \to \tilde{\tau}_1)$	0.002	0.001	$\cdots$	$\cdots$
$\sigma(\tilde{b}_2) \times \mathrm{BR}(\tilde{b}_2 \to \tilde{\tau}_1^*)$	0.002	0.001	$\cdots$	$\cdots$
$\sigma(\tilde{u}_L^*) \times \mathrm{BR}(\tilde{u}_L^* \to \tilde{\tau}_1)$	0.083	0.047	0.027	0.017
$\sigma(\tilde{u}_L^*) \times \mathrm{BR}(\tilde{u}_L^* \to \tilde{\tau}_1^*)$	0.072	0.043	0.026	0.016
$\sigma(\tilde{d}_L^*) \times \mathrm{BR}(\tilde{d}_L^* \to \tilde{\tau}_1)$	0.079	0.046	0.027	0.016
$\sigma(\tilde{d}_L^*) \times \mathrm{BR}(\tilde{d}_L^* \to \tilde{\tau}_1^*)$	0.087	0.050	0.028	0.017
$\sigma(\tilde{t}_1^*) \times \mathrm{BR}(\tilde{t}_1^* \to \tilde{\tau}_1)$	0.157	0.093	0.054	0.035
$\sigma(\tilde{t}_1^*) \times \mathrm{BR}(\tilde{t}_1^* \to \tilde{\tau}_1^*)$	0.157	0.093	0.054	0.035
$\sigma(\tilde{t}_2^*) \times \mathrm{BR}(\tilde{t}_2^* \to \tilde{\tau}_1)$	0.012	0.007	0.004	0.002
$\sigma(\tilde{t}_2^*) \times \mathrm{BR}(\tilde{t}_2^* \to \tilde{\tau}_1^*)$	0.011	0.006	0.004	0.002
$\sigma(\tilde{b}_1^*) \times \mathrm{BR}(\tilde{b}_1^* \to \tilde{\tau}_1)$	0.015	0.009	0.005	0.003
$\sigma(\tilde{b}_1^*) \times \mathrm{BR}(\tilde{b}_1^* \to \tilde{\tau}_1^*)$	0.016	0.009	0.005	0.003
$\sigma(\tilde{b}_2^*) \times \mathrm{BR}(\tilde{b}_2^* \to \tilde{\tau}_1)$	0.002	0.001	$\cdots$	$\cdots$
$\sigma(\tilde{b}_2^*) \times \mathrm{BR}(\tilde{b}_2^* \to \tilde{\tau}_1^*)$	0.002	0.001	$\cdots$	$\cdots$
$\sigma(\tilde{\chi}_2^0) \times \mathrm{BR}(\tilde{\chi}_2^0 \to \tilde{\tau}_1)$	0.787	0.559	0.400	0.297
$\sigma(\tilde{\chi}_2^0) \times \mathrm{BR}(\tilde{\chi}_2^0 \to \tilde{\tau}_1^*)$	0.787	0.559	0.400	0.297
$\sigma(\tilde{\chi}_1^+) \times \mathrm{BR}(\tilde{\chi}_1^+ \to \tilde{\tau}_1)$	0.896	0.645	0.464	0.348
$\sigma(\tilde{\chi}_1^+) \times \mathrm{BR}(\tilde{\chi}_1^+ \to \tilde{\tau}_1^*)$	1.036	0.725	0.513	0.380
$\sigma(\tilde{\chi}_1^-) \times \mathrm{BR}(\tilde{\chi}_1^- \to \tilde{\tau}_1)$	0.620	0.430	0.301	0.222
$\sigma(\tilde{\chi}_1^-) \times \mathrm{BR}(\tilde{\chi}_1^- \to \tilde{\tau}_1^*)$	0.536	0.383	0.273	0.203
$\sigma(\tilde{\tau}_2) \times \mathrm{BR}(\tilde{\tau}_2 \to \tilde{\tau}_1)$	0.102	0.067	0.049	0.037
$\sigma(\tilde{\tau}_2^*) \times \mathrm{BR}(\tilde{\tau}_2^* \to \tilde{\tau}_1^*)$	0.102	0.067	0.049	0.037
$\sigma(p \to \tilde{\tau}_1)$	0.428	0.317	0.245	0.190
$\sigma(p \to \tilde{\tau}_1^*)$	0.428	0.317	0.245	0.190
Total : $\sigma(\tilde{\tau}_1)$	7.714	5.153	3.480	2.439
Total : $\sigma(\tilde{\tau}_1^*)$	8.012	5.263	3.543	2.477
Number of produced $\tilde{\tau}_1^{(*)}$				
$N(\tilde{\tau}_1)$	771	515	348	243
$N(\tilde{\tau}_1^*)$	801	526	354	247
Number of produced $\tilde{\chi}_1^0$				
$N(\tilde{\chi}_1^0)$	7203	4711	3097	2108

Table 4.7: Summary of the cross sections and branching ratios and number of the produced staus and neutralinos for $\tan\beta = 10$. We assume the energy in the center-of-mass system as 14 TeV at the LHC experiment. In the estimation of the number of produced staus and neutralinos, we assume the luminosity as 100 fb^{-1}.

Input parameters	Point 5 (GeV)	Point 6 (GeV)	Point 7 (GeV)	Point 8 (GeV)	Point 9 (GeV)
$M_{1/2}$	818.6	878.0	932.8	986.0	1038.0
m_0	452.0	517.7	557.7	601.7	639.7
A_0	-2264.7	-2683.6	-2918.4	-3177.9	-3397.0
Particle					
h	123.8	124.4	124.6	124.8	124.9
H	1494.6	1659.5	1775.7	1894.0	2002.0
A	1495.1	1660.3	1776.5	1895.1	2003.3
$H^{\pm}$	1497.0	1662.0	1778.1	1896.5	2004.6
$\tilde{g}$	1822.4	1945.4	2057.8	2166.7	2272.6
$\tilde{\chi}_1^{\pm}$	665.6	716.3	762.4	807.4	851.2
$\tilde{\chi}_2^{\pm}$	1470.6	1638.9	1753.5	1873.7	1981.4
$\tilde{\chi}_1^0$	349.3	376.3	400.9	425.0	448.5
$\tilde{\chi}_2^0$	665.3	716.1	762.4	807.4	851.2
$\tilde{\chi}_3^0$	1466.8	1635.3	1750.1	1870.5	1978.4
$\tilde{\chi}_4^0$	1469.7	1638.4	1753.1	1873.3	1981.0
$\tilde{e}_L$	709.6	781.6	834.9	890.0	940.6
$\tilde{e}_R$	547.5	614.2	658.7	706.2	748.6
$\tilde{\nu}_e$	749.2	777.4	830.9	886.2	937.0
$\tilde{\tau}_1$	350.3	377.0	401.0	425.6	449.1
$\tilde{\tau}_2$	656.0	713.7	759.3	805.9	849.4
$\tilde{\nu}_\tau$	642.7	701.2	747.4	794.6	838.7
$\tilde{u}_L$	1710.9	1834.4	1942.2	2048.0	2149.7
$\tilde{u}_R$	1646.6	1765.6	1869.0	1970.6	2068.0
$\tilde{d}_L$	1712.6	1835.9	1943.7	2049.4	2151.0
$\tilde{d}_R$	1639.9	1758.3	1861.1	1962.1	2059.0
$\tilde{t}_1$	945.8	936.5	968.6	987.7	1016.3
$\tilde{t}_2$	1432.8	1497.5	1573.1	1641.3	1710.8
$\tilde{b}_1$	1384.6	1452.8	1528.4	1598.2	1669.3
$\tilde{b}_2$	1561.6	1665.8	1760.5	1852.6	1942.0

Table 4.8: Input parameters and the mass spectrum of sample points. The value of $\tan\beta$ is fixed to 20 and sign(μ) > 0. We choose these parameters as the $m_{\tilde{\chi}_1^0}$ is fixed to 350, 375, 400, 425, and 450 GeV, respectively.

Particle	Final states	Point 5 (%)	Point 6 (%)	Point 7 (%)	Point 8 (%)	Point 9 (%)
$\tilde{g}$	$\bar{t}, \tilde{t}_1$	21.4	22.6	22.9	23.3	23.6
	$t, \tilde{t}_1^*$	21.4	22.6	22.9	23.3	23.6
	$\bar{b}, \tilde{b}_1$	8.3	8.4	8.4	8.5	8.5
	$b, \tilde{b}_1^*$	8.3	8.4	8.4	8.5	8.5
	$\bar{t}, \tilde{t}_2$	7.9	8.2	8.3	8.3	8.4
	$t, \tilde{t}_2^*$	7.9	8.2	8.3	8.3	8.4
	$\bar{b}, \tilde{b}_2$	3.3	3.1	3.0	3.0	2.9
	$b, \tilde{b}_2^*$	3.3	3.1	3.0	3.0	2.9
$\tilde{u}_L$	$d, \tilde{\chi}_1^+$	65.8	65.8	65.8	65.8	65.7
	$u, \tilde{\chi}_2^0$	32.8	32.9	32.9	32.9	32.9
	$u, \tilde{\chi}_1^0$	1.4	1.4	1.4	1.4	1.4
$\tilde{d}_L$	$u, \tilde{\chi}_1^-$	65.6	65.6	65.7	65.7	65.7
	$d, \tilde{\chi}_2^0$	32.9	32.9	32.9	32.9	32.9
	$d, \tilde{\chi}_1^0$	1.5	1.5	1.5	1.5	1.5
$\tilde{t}_1$	$t, \tilde{\chi}_1^0$	78.4	86.3	89.4	92.7	94.8
	$b, \tilde{\chi}_1^+$	15.8	10.5	8.3	6.0	4.6
	$t, \tilde{\chi}_2^0$	5.9	3.2	2.4	1.3	0.6
$\tilde{t}_2$	$Z, \tilde{t}_1$	41.7	43.5	43.7	44.1	44.3
	$h, \tilde{t}_1$	29.1	32.0	33.2	34.4	35.3
	$b, \tilde{\chi}_1^+$	19.1	16.0	15.1	14.0	13.4
	$t, \tilde{\chi}_2^0$	9.1	7.7	7.2	6.7	6.4
$\tilde{b}_1$	$W^-, \tilde{t}_1$	69.9	83.7	76.9	78.7	79.8
	$t, \tilde{\chi}_1^-$	19.3	15.9	14.9	13.7	13.0
	$b, \tilde{\chi}_2^0$	10.2	8.4	7.8	7.9	6.8
$\tilde{b}_2$	$W^-, \tilde{t}_1$	44.0	39.7	36.5	33.4	30.9
	$h, \tilde{\chi}_1^0$	31.6	30.2	30.2	29.8	29.7
	$h, \tilde{b}_1$	9.4	12.6	13.8	15.0	15.8
	$Z, \tilde{b}_1$	5.7	7.7	8.5	9.4	9.9
	$W^-, \tilde{t}_2$	3.3	6.6	8.3	10.2	11.7
	$t, \tilde{\chi}_1^-$	2.9	2.1	1.8	1.5	1.3
	$b, \tilde{\chi}_2^0$	1.5	1.1	0.9	0.8	0.7
$\tilde{\nu}_\tau$	$W^+, \tilde{\tau}_1$	81.8	83.0	83.4	83.8	84.0
	$\nu_\tau, \tilde{\chi}_1^0$	18.2	17.0	16.6	16.2	16.0
$\tilde{\tau}_2$	$Z, \tilde{\tau}_1$	41.3	41.8	41.9	42.0	42.0
	$h, \tilde{\tau}_1$	39.0	39.9	40.5	40.9	41.2
	$\tau, \tilde{\chi}_1^0$	19.7	18.3	17.7	14.2	16.8
$\tilde{\chi}_2^0$	$\bar{\tau}, \tilde{\tau}_1$	40.1	45.0	45.0	46.1	46.2
	$\tau, \tilde{\tau}_1^*$	40.1	45.0	45.0	46.1	46.2
	$\bar{\nu}_\tau, \tilde{\nu}_\tau$	7.3	3.6	3.6	2.6	2.5
	$\nu_\tau, \tilde{\nu}^*$	7.3	3.6	3.6	2.6	2.5
	$h, \tilde{\chi}_1^0$	2.5	2.5	2.5	2.5	2.4

Table 4.9: Branching ratios of the SUSY particles on the sample points for $\tan\beta = 20$.

Particle	Final states	Point 5 (%)	Point 6 (%)	Point 7 (%)	Point 8 (%)	Point 9 (%)
$\tilde{\chi}_3^0$	$\bar{t}, \tilde{t}_1$	22.6	26.7	26.7	26.9	27.0
	$t, \tilde{t}_1^*$	22.6	26.7	26.7	26.9	27.0
	$W^-, \tilde{\chi}_1^+$	15.0	12.6	11.6	10.7	10.3
	$W^+, \tilde{\chi}_1^-$	15.0	12.6	11.6	10.7	10.3
	$Z, \tilde{\chi}_2^0$	13.2	11.0	10.1	9.3	8.9
	$Z, \tilde{\chi}_1^0$	4.0	3.3	3.0	2.8	2.7
	$h, \tilde{\chi}_2^0$	1.6	1.4	1.3	1.3	1.2
	$\bar{t}, \tilde{t}_2$	$\cdots$	$\cdots$	1.8	3.1	3.7
	$t, \tilde{t}_2^*$	$\cdots$	$\cdots$	1.8	3.1	3.7
$\tilde{\chi}_4^0$	$\bar{t}, \tilde{t}_1$	27.0	29.8	29.9	30.0	29.9
	$t, \tilde{t}_1^*$	27.0	29.8	29.9	30.0	29.9
	$W^-, \tilde{\chi}_1^+$	12.3	10.7	10.3	9.8	9.5
	$W^+, \tilde{\chi}_1^-$	12.3	10.7	10.3	9.8	9.5
	$h, \tilde{\chi}_2^0$	11.4	9.9	9.6	9.1	8.9
	$h, \tilde{\chi}_1^0$	3.1	2.6	2.5	2.4	2.3
	$Z, \tilde{\chi}_2^0$	1.3	1.2	1.2	1.1	1.1
$\tilde{\chi}_1^+$	$\nu_\tau, \tilde{\tau}_1^*$	79.3	89.1	89.2	91.3	91.5
	$\bar{\tau}, \tilde{\nu}_\tau$	15.0	7.5	7.3	5.4	5.2
	$W^+, \tilde{\chi}_1^0$	3.1	3.2	3.1	3.2	3.2
$\tilde{\chi}_2^+$	$\bar{b}, \tilde{t}_1$	48.4	53.0	53.3	53.9	54.1
	$h, \tilde{\chi}_1^+$	14.2	11.9	11.3	10.6	10.3
	$Z, \tilde{\chi}_1^+$	13.8	11.5	10.9	10.2	9.9
	$W^+, \tilde{\chi}_2^0$	14.0	11.7	11.1	10.4	10.0
	$W^+, \tilde{\chi}_1^0$	4.7	3.9	3.7	3.5	3.4
	$t, \tilde{b}_1^*$	4.8	3.4	5.1	6.8	7.8
	$\nu_\tau, \tilde{\tau}_1^*$	2.1	1.8	1.8	1.7	1.6
	$\bar{\tau}, \tilde{\nu}_\tau$	1.9	1.6	1.5	1.4	1.4
H	b, b	63.3	61.1	60.4	59.6	59.2
	$\tau, \bar{\tau}$	11.6	11.4	11.4	11.3	11.3
	$\tilde{\tau}_1, \tilde{\tau}_2^*$	10.0	11.3	11.7	12.2	12.6
	$\tilde{\tau}_1^*, \tilde{\tau}_2$	10.0	11.3	11.7	12.2	12.6
	$\tilde{\tau}_1^*, \tilde{\tau}_1$	1.9	1.8	1.7	1.6	1.4
	$t, \bar{t}$	1.6	1.6	1.6	1.6	1.6
A	b, b	62.4	60.8	60.2	59.5	59.1
	$\tau, \bar{\tau}$	11.6	11.4	11.3	11.3	11.3
	$\tilde{\tau}_1, \tilde{\tau}_2^*$	11.5	12.7	13.1	13.5	13.7
	$\tilde{\tau}_1^*, \tilde{\tau}_2$	11.5	12.7	13.1	13.5	13.7
	$t, \bar{t}$	1.6	1.5	1.5	1.5	1.5
H^+	b, t	62.9	63.9	64.8	65.2	66.2
	$\tilde{\tau}_1, \tilde{\nu}_\tau$	25.9	24.9	23.9	23.4	22.2
	$\bar{\tau}, \nu_\tau$	10.3	10.5	10.6	10.8	11.0

Table 4.10: Branching ratios of the SUSY particles on the sample points for $\tan\beta = 20$.

Cross section	Point 5 (fb)	Point 6 (fb)	Point 7 (fb)	Point 8 (fb)	Point 9 (fb)
$\sigma(\tilde{u}_L, \tilde{u}_L)$	2.915	1.873	1.277	0.879	0.614
$\sigma(\tilde{u}_L, \tilde{u}_R)$	1.672	1.024	0.668	0.441	0.296
$\sigma(\tilde{u}_R, \tilde{u}_R)$	2.970	1.926	1.327	0.923	0.652
$\sigma(\tilde{d}_L, \tilde{d}_L)$	0.377	0.225	0.144	0.093	0.061
$\sigma(\tilde{d}_L, \tilde{d}_R)$	0.194	0.110	0.068	0.042	0.026
$\sigma(\tilde{d}_R, \tilde{d}_R)$	0.381	0.230	0.149	0.098	0.065
$\sigma(\tilde{u}_L, \tilde{d}_L)$	3.243	2.016	1.335	0.894	0.608
$\sigma(\tilde{u}_L, \tilde{d}_R)$	0.557	0.329	0.208	0.133	0.087
$\sigma(\tilde{u}_R, \tilde{d}_L)$	0.551	0.325	0.205	0.131	0.086
$\sigma(\tilde{u}_R, \tilde{d}_R)$	2.680	1.680	1.124	0.759	0.522
$\sigma(\tilde{g}, \tilde{u}_L)$	2.735	1.506	0.899	0.537	0.330
$\sigma(\tilde{g}, \tilde{u}_R)$	3.156	1.750	1.041	0.633	0.391
$\sigma(\tilde{g}, \tilde{d}_L)$	0.826	0.440	0.252	0.148	0.088
$\sigma(\tilde{g}, \tilde{d}_R)$	0.981	0.527	0.305	0.180	0.109
$\sigma(\tilde{g}, \tilde{g})$	0.440	0.219	0.118	0.065	0.036
$\sigma(\tilde{u}_L, \tilde{u}_L^*)$	0.076	0.040	0.024	0.015	0.007
$\sigma(\tilde{u}_L, \tilde{u}_R^*)$	0.220	0.126	0.078	0.049	0.031
$\sigma(\tilde{u}_R, \tilde{u}_L^*)$	0.220	0.126	0.078	0.049	0.031
$\sigma(\tilde{u}_R, \tilde{u}_R^*)$	0.109	0.060	0.034	0.020	0.013
$\sigma(\tilde{d}_L, \tilde{d}_L^*)$	0.054	0.027	0.016	0.009	0.004
$\sigma(\tilde{d}_L, \tilde{d}_R^*)$	0.080	0.042	0.024	0.014	0.008
$\sigma(\tilde{d}_R, \tilde{d}_L^*)$	0.080	0.042	0.024	0.014	0.008
$\sigma(\tilde{d}_R, \tilde{d}_R^*)$	0.078	0.040	0.023	0.013	0.007
$\sigma(\tilde{u}_L, \tilde{d}_R^*)$	0.254	0.139	0.083	0.050	0.030
$\sigma(\tilde{u}_R, \tilde{d}_L^*)$	0.249	0.136	0.083	0.048	0.029
$\sigma(\tilde{u}_L, \tilde{d}_L^*)$	0.035	0.018	0.010	0.005	0.003
$\sigma(\tilde{u}_R, \tilde{d}_R^*)$	0.056	0.029	0.017	0.009	0.006
$\sigma(\tilde{d}_L, \tilde{u}_L^*)$	0.010	0.005	0.003	0.002	0.001
$\sigma(\tilde{d}_R, \tilde{u}_L^*)$	0.069	0.038	0.023	0.014	0.009
$\sigma(\tilde{d}_L, \tilde{u}_R^*)$	0.069	0.037	0.022	0.014	0.008
$\sigma(\tilde{d}_R, \tilde{u}_R^*)$	0.015	0.008	0.005	0.003	0.002
$\sigma(\tilde{g}, \tilde{u}_L^*)$	0.051	0.025	0.014	0.008	0.004
$\sigma(\tilde{g}, \tilde{u}_R^*)$	0.061	0.030	0.017	0.009	0.005
$\sigma(\tilde{g}, \tilde{d}_L^*)$	0.045	0.021	0.011	0.006	0.003
$\sigma(\tilde{g}, \tilde{d}_R^*)$	0.056	0.027	0.014	0.007	0.004

Table 4.11: Cross sections of SUSY particles on the sample points for $\tan\beta = 20$. We assume the energy in the center-of-mass system as 14 TeV at the LHC experiment.

Cross section	Point 5 (fb)	Point 6 (fb)	Point 7 (fb)	Point 8 (fb)	Point 9 (fb)
$\sigma(\tilde{t}_1, \tilde{t}_1^*)$	4.399	4.704	3.662	3.245	2.655
$\sigma(\tilde{t}_2, \tilde{t}_2^*)$	0.190	0.128	0.085	0.058	0.039
$\sigma(\tilde{b}_1, \tilde{b}_1^*)$	0.252	0.169	0.108	0.074	0.049
$\sigma(\tilde{b}_2, \tilde{b}_2^*)$	0.089	0.050	0.030	0.018	0.011
$\sigma(\tilde{\chi}_2^0, \tilde{\chi}_2^0)$	0.102	0.069	0.049	0.036	0.027
$\sigma(\tilde{\chi}_1^0, \tilde{\chi}_2^0)$	0.014	0.010	0.008	0.006	0.004
$\sigma(\tilde{\chi}_1^0, \tilde{\chi}_1^0)$	0.103	0.075	0.057	0.043	0.034
$\sigma(\tilde{\chi}_2^0, \tilde{g})$	0.202	0.123	0.080	0.053	0.035
$\sigma(\tilde{\chi}_1^0, \tilde{g})$	0.227	0.146	0.099	0.068	0.048
$\sigma(\tilde{\chi}_1^+, \tilde{\chi}_1^-)$	2.459	1.722	1.274	0.939	0.711
$\sigma(\tilde{\chi}_1^+, \tilde{\chi}_2^0)$	3.510	2.505	1.858	1.403	1.076
$\sigma(\tilde{\chi}_1^-, \tilde{\chi}_2^0)$	1.231	0.852	0.616	0.455	0.341
$\sigma(\tilde{\chi}_1^+, \tilde{\chi}_1^0)$	0.023	0.017	0.012	0.009	0.007
$\sigma(\tilde{\chi}_1^-, \tilde{\chi}_1^0)$	0.008	0.005	0.004	0.003	0.002
$\sigma(\tilde{\chi}_1^+, \tilde{g})$	0.344	0.209	0.134	0.087	0.058
$\sigma(\tilde{\chi}_1^-, \tilde{g})$	0.085	0.057	0.036	0.024	0.016
$\sigma(\tilde{\tau}_1, \tilde{\tau}_1^*)$	0.844	0.626	0.484	0.37	0.298
$\sigma(\tilde{\tau}_1, \tilde{\tau}_2^*)$	0.012	0.007	0.005	0.003	0.002
$\sigma(\tilde{\tau}_2, \tilde{\tau}_1^*)$	0.012	0.007	0.005	0.003	0.002
$\sigma(\tilde{\tau}_2, \tilde{\tau}_2^*)$	0.115	0.075	0.055	0.040	0.036
σ(all SUSY)	39.798	26.761	18.387	13.258	8.681

Table 4.12: Cross sections of SUSY particles on the sample points for $\tan\beta = 20$. We assume the energy in the center-of-mass system as 14 TeV at the LHC experiment.

Cross section × branching ratio	Point 5 (fb)	Point 6 (fb)	Point 7 (fb)	Point 8 (fb)	Point 9 (fb)
$\sigma(\tilde{g}) \times \mathrm{BR}(\tilde{g} \to \tilde{\tau}_1)$	1.129	0.464	0.231	0.111	0.062
$\sigma(\tilde{g}) \times \mathrm{BR}(\tilde{g} \to \tilde{\tau}_1^*)$	1.129	0.464	0.231	0.111	0.062
$\sigma(\tilde{u}_L) \times \mathrm{BR}(\tilde{u}_L \to \tilde{\tau}_1)$	3.391	1.779	1.161	0.733	0.284
$\sigma(\tilde{u}_L) \times \mathrm{BR}(\tilde{u}_L \to \tilde{\tau}_1^*)$	11.021	7.023	4.600	3.066	1.195
$\sigma(\tilde{d}_L) \times \mathrm{BR}(\tilde{d}_L \to \tilde{\tau}_1)$	4.349	2.704	1.735	1.136	0.750
$\sigma(\tilde{d}_L) \times \mathrm{BR}(\tilde{d}_L \to \tilde{\tau}_1^*)$	1.342	0.687	0.439	0.272	0.179
$\sigma(\tilde{t}_1) \times \mathrm{BR}(\tilde{t}_1 \to \tilde{\tau}_1)$	0.204	0.103	0.060	0.029	0.011
$\sigma(\tilde{t}_1) \times \mathrm{BR}(\tilde{t}_1 \to \tilde{\tau}_1^*)$	0.755	0.544	0.330	0.207	0.106
$\sigma(\tilde{t}_2) \times \mathrm{BR}(\tilde{t}_2 \to \tilde{\tau}_1)$	0.020	0.008	0.005	0.003	0.002
$\sigma(\tilde{t}_2) \times \mathrm{BR}(\tilde{t}_2 \to \tilde{\tau}_1^*)$	0.067	0.037	0.022	0.013	0.007
$\sigma(\tilde{b}_1) \times \mathrm{BR}(\tilde{b}_1 \to \tilde{\tau}_1)$	0.053	0.029	0.017	0.010	0.006
$\sigma(\tilde{b}_1) \times \mathrm{BR}(\tilde{b}_1 \to \tilde{\tau}_1^*)$	0.036	0.018	0.008	0.004	0.002
$\sigma(\tilde{b}_2) \times \mathrm{BR}(\tilde{b}_2 \to \tilde{\tau}_1)$	0.008	0.004	0.002	0.001	0.001
$\sigma(\tilde{b}_2) \times \mathrm{BR}(\tilde{b}_2 \to \tilde{\tau}_1^*)$	0.010	0.005	0.002	0.001	0.001
$\sigma(\tilde{u}_L^*) \times \mathrm{BR}(\tilde{u}_L^* \to \tilde{\tau}_1)$	0.321	0.184	0.111	0.069	0.041
$\sigma(\tilde{u}_L^*) \times \mathrm{BR}(\tilde{u}_L^* \to \tilde{\tau}_1^*)$	0.099	0.047	0.028	0.017	0.010
$\sigma(\tilde{d}_L^*) \times \mathrm{BR}(\tilde{d}_L^* \to \tilde{\tau}_1)$	0.107	0.049	0.028	0.015	0.009
$\sigma(\tilde{d}_L^*) \times \mathrm{BR}(\tilde{d}_L^* \to \tilde{\tau}_1^*)$	0.348	0.191	0.111	0.065	0.037
$\sigma(\tilde{t}_1^*) \times \mathrm{BR}(\tilde{t}_1^* \to \tilde{\tau}_1)$	0.755	0.544	0.330	0.207	0.106
$\sigma(\tilde{t}_1^*) \times \mathrm{BR}(\tilde{t}_1^* \to \tilde{\tau}_1^*)$	0.204	0.103	0.060	0.029	0.011
$\sigma(\tilde{t}_2^*) \times \mathrm{BR}(\tilde{t}_2^* \to \tilde{\tau}_1)$	0.064	0.035	0.021	0.013	0.007
$\sigma(\tilde{t}_2^*) \times \mathrm{BR}(\tilde{t}_2^* \to \tilde{\tau}_1^*)$	0.019	0.008	0.005	0.003	0.002
$\sigma(\tilde{b}_1^*) \times \mathrm{BR}(\tilde{b}_1^* \to \tilde{\tau}_1)$	0.037	0.018	0.009	0.004	0.002
$\sigma(\tilde{b}_1^*) \times \mathrm{BR}(\tilde{b}_1^* \to \tilde{\tau}_1^*)$	0.053	0.029	0.017	0.010	0.006
$\sigma(\tilde{b}_2^*) \times \mathrm{BR}(\tilde{b}_2^* \to \tilde{\tau}_1)$	0.010	0.005	0.002	0.001	0.001
$\sigma(\tilde{b}_2^*) \times \mathrm{BR}(\tilde{b}_2^* \to \tilde{\tau}_1^*)$	0.008	0.004	0.002	0.001	0.001
$\sigma(\tilde{\chi}_2^0) \times \mathrm{BR}(\tilde{\chi}_2^0 \to \tilde{\tau}_1)$	2.379	1.742	1.276	0.961	0.730
$\sigma(\tilde{\chi}_2^0) \times \mathrm{BR}(\tilde{\chi}_2^0 \to \tilde{\tau}_1^*)$	2.379	1.742	1.276	0.961	0.730
$\sigma(\tilde{\chi}_1^+) \times \mathrm{BR}(\tilde{\chi}_1^+ \to \tilde{\tau}_1)$	0.777	0.277	0.201	0.111	0.081
$\sigma(\tilde{\chi}_1^+) \times \mathrm{BR}(\tilde{\chi}_1^+ \to \tilde{\tau}_1^*)$	5.802	4.245	3.125	2.337	1.776
$\sigma(\tilde{\chi}_1^-) \times \mathrm{BR}(\tilde{\chi}_1^- \to \tilde{\tau}_1)$	3.464	2.512	1.840	1.362	1.026
$\sigma(\tilde{\chi}_1^-) \times \mathrm{BR}(\tilde{\chi}_1^- \to \tilde{\tau}_1^*)$	0.464	0.164	0.119	0.065	0.047
$\sigma(\tilde{\tau}_2) \times \mathrm{BR}(\tilde{\tau}_2 \to \tilde{\tau}_1)$	0.102	0.067	0.049	0.036	0.032
$\sigma(\tilde{\tau}_2^*) \times \mathrm{BR}(\tilde{\tau}_2^* \to \tilde{\tau}_1^*)$	0.102	0.067	0.049	0.036	0.032
$\sigma(p \to \tilde{\tau}_1)$	0.428	0.317	0.245	0.190	0.150
$\sigma(p \to \tilde{\tau}_1^*)$	0.428	0.317	0.245	0.190	0.150
Total : $\sigma(\tilde{\tau}_1)$	18.026	11.157	7.568	5.182	3.451
Total : $\sigma(\tilde{\tau}_1^*)$	24.694	16.009	10.913	7.576	4.502
Number of produced $\tilde{\tau}_1^{(*)}$					
$N(\tilde{\tau}_1)$	1802	1115	756	518	345
$N(\tilde{\tau}_1^*)$	2469	1600	1091	757	450
Number of produced $\tilde{\chi}_1^0$					
$N(\tilde{\chi}_1^0)$	3687	2635	1829	1375	940

Table 4.13: Summary of the cross sections and branching ratios and number of the produced staus and neutralinos for $\tan\beta = 20$. We assume the energy in the center-of-mass system as 14 TeV at the LHC experiment. In the estimation of the number of produced staus and neutralinos, we assume the luminosity as 100 fb^{-1}.

Input parameters	Point 10 (GeV)	Point 11 (GeV)	Point 12 (GeV)
$M_{1/2}$	932.6	986.0	1038.0
m_0	560.0	704.5	935.0
A_0	-1653.9	-2319.8	-3377.8
Particle			
h	123.3	124.7	126.3
H	1353.2	1534.9	1811.8
A	1353.2	1535.0	1812.2
$H^{\pm}$	1356.1	1537.6	1814.4
$\tilde{g}$	2060.1	2174.1	2289.8
$\tilde{\chi}_1^{\pm}$	759.1	807.0	855.4
$\tilde{\chi}_2^{\pm}$	1410.4	1621.9	1946.4
$\tilde{\chi}_1^0$	399.9	425.0	450.3
$\tilde{\chi}_2^0$	758.9	806.8	855.2
$\tilde{\chi}_3^0$	1406.1	1618.3	1943.5
$\tilde{\chi}_4^0$	1408.9	1620.6	1946.0
$\tilde{e}_L$	835.5	961.2	1159.7
$\tilde{e}_R$	660.7	795.7	1012.1
$\tilde{\nu}_e$	831.4	957.6	1156.7
$\tilde{\tau}_1$	400.3	425.6	450.4
$\tilde{\tau}_2$	763.1	849.1	978.4
$\tilde{\nu}_\tau$	748.3	835.3	966.3
$\tilde{u}_L$	1941.0	2078.9	2252.2
$\tilde{u}_R$	1867.3	2002.5	2175.3
$\tilde{d}_L$	1942.5	2080.3	2253.4
$\tilde{d}_R$	1859.6	1994.4	2166.9
$\tilde{t}_1$	1295.1	1272.0	1127.5
$\tilde{t}_2$	1666.0	1721.3	1741.8
$\tilde{b}_1$	1622.1	1677.6	1697.8
$\tilde{b}_2$	1733.6	1829.6	1935.9

Table 4.14: Input parameters and the mass spectrum of sample points. The value of $\tan\beta$ is fixed to 30 and $\text{sign}(\mu) > 0$. We choose these parameters as the $m_{\tilde{\chi}_1^0}$ is fixed to 400, 425, and 450 GeV, respectively.

Particle	Final states	Point 10 (%)	Point 11 (%)	Point 12 (%)
$\tilde{g}$	$\bar{t}, \tilde{t}_1$	18.1	20.8	24.9
	$t, \tilde{t}_1^*$	18.1	20.8	24.9
	$\bar{b}, \tilde{b}_1$	7.4	7.4	7.3
	$b, \tilde{b}_1^*$	7.4	7.4	7.3
	$\bar{t}, \tilde{t}_2$	8.1	8.7	9.4
	$t, \tilde{t}_2^*$	8.1	8.7	9.4
	$\bar{b}, \tilde{b}_2$	5.0	4.7	3.9
	$b, \tilde{b}_2^*$	5.0	4.7	3.9
$\tilde{u}_L$	$d, \tilde{\chi}_1^+$	65.7	65.7	65.8
	$u, \tilde{\chi}_2^0$	32.8	32.8	32.9
	$u, \tilde{\chi}_1^0$	1.4	1.4	1.4
$\tilde{d}_L$	$u, \tilde{\chi}_1^-$	65.4	65.6	65.7
	$d, \tilde{\chi}_2^0$	32.8	32.8	32.9
	$d, \tilde{\chi}_1^0$	1.5	1.4	1.4
$\tilde{t}_1$	$t, \tilde{\chi}_1^0$	67.6	75.4	88.4
	$b, \tilde{\chi}_1^+$	22.3	17.0	8.4
	$t, \tilde{\chi}_2^0$	10.1	7.6	3.2
$\tilde{t}_2$	$Z, \tilde{t}_1$	27.5	35.3	42.2
	$h, \tilde{t}_1$	19.4	26.0	33.1
	$b, \tilde{\chi}_1^+$	28.6	25.0	16.1
	$t, \tilde{\chi}_2^0$	13.7	12.0	7.8
	$t, \tilde{\chi}_1^0$	1.6	1.3	$\cdots$
	$t, \tilde{\chi}_3^0$	2.1	$\cdots$	$\cdots$
	$t, \tilde{\chi}_4^0$	4.3	$\cdots$	$\cdots$
	$b, \tilde{\chi}_2^+$	2.8	$\cdots$	$\cdots$
$\tilde{b}_1$	$W^-, \tilde{t}_1$	44.6	58.9	74.9
	$t, \tilde{\chi}_1^-$	32.1	26.3	16.1
	$b, \tilde{\chi}_2^0$	16.8	13.7	8.4
	$b, \tilde{\chi}_1^0$	1.3	$\cdots$	$\cdots$
	$b, \tilde{\chi}_2^-$	3.6	$\cdots$	$\cdots$
$\tilde{b}_2$	$W^-, \tilde{t}_1$	34.5	43.2	39.8
	$W^-, \tilde{t}_2$	-	17.0	10.4
	$b, \tilde{\chi}_1^0$	15.8	20.6	19.4
	$b, \tilde{\chi}_2^0$	$\cdots$	2.4	1.1
	$b, \tilde{\chi}_3^0$	8.3	4.1	$\cdots$
	$b, \tilde{\chi}_4^0$	8.5	4.2	$\cdots$
	$h, \tilde{b}_1$	$\cdots$	6.2	17.0
	$Z, \tilde{b}_1$	$\cdots$	3.9	10.1
	$t, \tilde{\chi}_1^-$	6.0	4.6	20.7
	$t, \tilde{\chi}_2^-$	22.9	9.1	$\cdots$
$\tilde{\nu}_\tau$	$W^+, \tilde{\tau}_1$	87.2	87.2	81.7
	$\nu_\tau, \tilde{\chi}_1^0$	12.8	11.9	10.4
$\tilde{\tau}_2$	$Z, \tilde{\tau}_1$	45.6	44.7	41.3
	$h, \tilde{\tau}_1$	40.1	40.5	38.7
	$\tau, \tilde{\chi}_1^0$	14.3	12.9	11.8
$\tilde{\chi}_2^0$	$\bar{\tau}, \tilde{\tau}_1$	46.967	48.5	48.9
	$\tau, \tilde{\tau}_1^*$	46.9	48.5	48.9
	$h, \tilde{\chi}_1^0$	3.5	2.8	2.1

Table 4.15: Branching ratios of the SUSY particles on the sample points for $\tan\beta = 30$.

Particle	Final states	Point 10 (%)	Point 11 (%)	Point 12 (%)
$\tilde{\chi}_3^0$	$W^-, \tilde{\chi}_1^+$	25.0	19.3	11.3
	$W^+, \tilde{\chi}_1^-$	25.0	19.3	11.3
	$\bar{t}, \tilde{t}_1$	$\cdots$	11.3	24.3
	$t, \tilde{t}_1^*$	$\cdots$	11.3	24.3
	$Z, \tilde{\chi}_1^0$	7.2	5.3	2.9
	$h, \tilde{\chi}_1^0$	1.8	1.5	$\cdots$
	$Z, \tilde{\chi}_2^0$	22.6	17.3	9.8
	$h, \tilde{\chi}_2^0$	1.8	1.8	1.4
	$\bar{\tau}, \tilde{\tau}_1$	5.1	3.9	2.3
	$\tau, \tilde{\tau}_1^*$	5.1	3.9	2.3
	$\bar{\tau}, \tilde{\tau}_2$	3.2	2.5	1.5
	$\tau, \tilde{\tau}_2^*$	3.2	2.5	1.5
$\tilde{\chi}_4^0$	$W^-, \tilde{\chi}_1^+$	24.4	16.6	10.2
	$W^+, \tilde{\chi}_1^-$	24.4	16.6	10.2
	$\bar{t}, \tilde{t}_1$	$\cdots$	16.1	27.3
	$t, \tilde{t}_1^*$	$\cdots$	16.1	27.3
	$Z, \tilde{\chi}_1^0$	1.9	1.3	$\cdots$
	$h, \tilde{\chi}_1^0$	6.6	4.3	2.5
	$Z, \tilde{\chi}_2^0$	1.9	1.5	1.2
	$h, \tilde{\chi}_2^0$	23.5	15.8	9.6
	$\bar{\tau}, \tilde{\tau}_1$	4.7	3.3	2.1
	$\tau, \tilde{\tau}_1^*$	4.7	3.3	2.1
	$\bar{\tau}, \tilde{\tau}_2$	3.4	2.3	1.4
	$\tau, \tilde{\tau}_2^*$	3.4	2.3	1.4
$\tilde{\chi}_1^+$	$\nu_\tau, \tilde{\tau}_1^*$	93.3	96.5	97.3
	$W^+, \tilde{\chi}_1^0$	4.2	3.5	2.7
	$\bar{\tau}, \tilde{\nu}_\tau$	2.5	$\cdots$	$\cdots$
$\tilde{\chi}_2^+$	$h, \tilde{\chi}_1^+$	23.5	18.2	11.1
	$Z, \tilde{\chi}_1^+$	22.8	17.6	10.7
	$W^+, \tilde{\chi}_1^0$	8.1	6.1	3.7
	$W^+, \tilde{\chi}_2^0$	23.3	17.9	10.9
	$\bar{b}, \tilde{t}_1$	6.3	28.1	49.2
	$\nu_\tau, \tilde{\tau}_1^*$	8.3	6.6	4.2
	$\tau, \tilde{\nu}_\tau$	8.3	4.6	2.5
	$t, \tilde{b}_1^*$	$\cdots$	$\cdots$	5.6
H	b, b	74.1	69.6	63.3
	$\tau, \bar{\tau}$	14.0	13.5	12.6
	$\tilde{\tau}_1, \tilde{\tau}_1^*$	1.4	1.5	1.5
	$\tilde{\tau}_1, \tilde{\tau}_2^*$	5.0	7.5	11.0
	$\tilde{\tau}_1^*, \tilde{\tau}_2$	5.0	7.5	11.0
A	b, b	73.8	69.3	62.9
	$\tau, \bar{\tau}$	14.0	13.5	12.6
	$\tilde{\tau}_1, \tilde{\tau}_2^*$	5.9	8.4	12.0
	$\tilde{\tau}_1^*, \tilde{\tau}_2$	5.9	8.4	12.0
H^+	b, t	77.5	73.7	68.2
	$\tilde{\tau}_1^*, \tilde{\nu}_\tau$	12.2	11.7	20.7
	$\bar{\tau}, \nu_\tau$	10.2	14.5	11.0

Table 4.16: Branching ratios of the SUSY particles on the sample points for $\tan\beta = 30$.

Cross section	Point 10 (fb)	Point 11 (fb)	Point 12 (fb)
$\sigma(\tilde{u}_L, \tilde{u}_L)$	1.283	0.786	0.425
$\sigma(\tilde{u}_L, \tilde{u}_R)$	0.670	0.397	0.209
$\sigma(\tilde{u}_R, \tilde{u}_R)$	1.336	0.825	0.447
$\sigma(\tilde{d}_L, \tilde{d}_L)$	0.145	0.082	0.040
$\sigma(\tilde{d}_L, \tilde{d}_R)$	0.068	0.037	0.018
$\sigma(\tilde{d}_R, \tilde{d}_R)$	0.150	0.085	0.048
$\sigma(\tilde{u}_L, \tilde{d}_L)$	1.341	0.790	0.406
$\sigma(\tilde{u}_L, \tilde{d}_R)$	0.209	0.119	0.059
$\sigma(\tilde{u}_R, \tilde{d}_L)$	0.206	0.117	0.058
$\sigma(\tilde{u}_R, \tilde{d}_R)$	1.132	0.672	0.347
$\sigma(\tilde{g}, \tilde{u}_L)$	0.887	0.493	0.255
$\sigma(\tilde{g}, \tilde{u}_R)$	1.040	0.580	0.299
$\sigma(\tilde{g}, \tilde{d}_L)$	0.251	0.135	0.070
$\sigma(\tilde{g}, \tilde{d}_R)$	0.304	0.164	0.080
$\sigma(\tilde{g}, \tilde{g})$	0.112	0.062	0.033
$\sigma(\tilde{u}_L, \tilde{u}_L^*)$	0.024	0.012	0.005
$\sigma(\tilde{u}_L, \tilde{u}_R^*)$	0.079	0.043	0.020
$\sigma(\tilde{u}_R, \tilde{u}_L^*)$	0.079	0.043	0.020
$\sigma(\tilde{u}_R, \tilde{u}_R^*)$	0.035	0.017	0.007
$\sigma(\tilde{d}_L, \tilde{d}_L^*)$	0.016	0.007	0.003
$\sigma(\tilde{d}_L, \tilde{d}_R^*)$	0.024	0.012	0.005
$\sigma(\tilde{d}_R, \tilde{d}_L^*)$	0.024	0.012	0.005
$\sigma(\tilde{d}_R, \tilde{d}_R^*)$	0.023	0.011	0.004
$\sigma(\tilde{u}_L, \tilde{d}_R^*)$	0.083	0.043	0.018
$\sigma(\tilde{u}_R, \tilde{d}_L^*)$	0.081	0.041	0.017
$\sigma(\tilde{u}_L, \tilde{d}_L^*)$	0.010	0.005	0.002
$\sigma(\tilde{u}_R, \tilde{d}_R^*)$	0.017	0.008	0.003
$\sigma(\tilde{d}_L, \tilde{u}_L^*)$	0.003	0.001	0.001
$\sigma(\tilde{d}_R, \tilde{u}_L^*)$	0.023	0.012	0.005
$\sigma(\tilde{d}_L, \tilde{u}_R^*)$	0.023	0.012	0.006
$\sigma(\tilde{d}_R, \tilde{u}_R^*)$	0.005	0.002	0.001
$\sigma(\tilde{g}, \tilde{u}_L^*)$	0.014	0.007	0.003
$\sigma(\tilde{g}, \tilde{u}_R^*)$	0.016	0.008	0.004
$\sigma(\tilde{g}, \tilde{d}_L^*)$	0.011	0.005	0.002
$\sigma(\tilde{g}, \tilde{d}_R^*)$	0.014	0.006	0.003

Table 4.17: Cross sections of SUSY particles on the sample points for $\tan\beta = 30$. We assume the energy in the center-of-mass system as 14 TeV at the LHC experiment.

Cross section	Point 10 (fb)	Point 11 (fb)	Point 12 (fb)
$\sigma(\tilde{t}_1, \tilde{t}_1^*)$	0.468	0.494	1.244
$\sigma(\tilde{t}_2, \tilde{t}_2^*)$	0.052	0.038	0.032
$\sigma(\tilde{b}_1, \tilde{b}_1^*)$	0.061	0.046	0.039
$\sigma(\tilde{b}_2, \tilde{b}_2^*)$	0.034	0.021	0.011
$\sigma(\tilde{\chi}_2^0, \tilde{\chi}_2^0)$	0.049	0.038	0.024
$\sigma(\tilde{\chi}_1^0, \tilde{\chi}_2^0)$	0.008	0.005	0.003
$\sigma(\tilde{\chi}_1^0, \tilde{\chi}_1^0)$	0.047	0.041	0.030
$\sigma(\tilde{\chi}_2^0, \tilde{g})$	0.080	0.050	0.031
$\sigma(\tilde{\chi}_1^0, \tilde{g})$	0.098	0.065	0.041
$\sigma(\tilde{\chi}_1^+, \tilde{\chi}_1^-)$	1.289	0.959	0.729
$\sigma(\tilde{\chi}_1^+, \tilde{\chi}_2^0)$	1.904	1.439	1.117
$\sigma(\tilde{\chi}_1^-, \tilde{\chi}_2^0)$	0.632	0.466	0.354
$\sigma(\tilde{\chi}_1^+, \tilde{\chi}_1^0)$	0.012	0.009	0.006
$\sigma(\tilde{\chi}_1^-, \tilde{\chi}_1^0)$	0.004	0.003	0.002
$\sigma(\tilde{\chi}_1^+, \tilde{g})$	0.134	0.084	0.051
$\sigma(\tilde{\chi}_1^-, \tilde{g})$	0.036	0.023	0.014
$\sigma(\tilde{\tau}_1, \tilde{\tau}_1^*)$	0.482	0.375	0.295
$\sigma(\tilde{\tau}_1, \tilde{\tau}_2^*)$	0.007	0.003	0.001
$\sigma(\tilde{\tau}_2, \tilde{\tau}_1^*)$	0.007	0.003	0.001
$\sigma(\tilde{\tau}_2, \tilde{\tau}_2^*)$	0.053	0.030	0.004
σ(all SUSY)	15.199	9.842	6.957

Table 4.18: Cross sections of SUSY particles on the sample points for $\tan\beta = 30$. We assume the energy in the center-of-mass system as 14 TeV at the LHC experiment.

Cross section × branching ratio	Point 10 (fb)	Point 11 (fb)	Point 12 (fb)
$\sigma(\tilde{g}) \times \mathrm{BR}(\tilde{g} \to \tilde{\tau}_1)$	0.555	0.278	0.088
$\sigma(\tilde{g}) \times \mathrm{BR}(\tilde{g} \to \tilde{\tau}_1^*)$	0.555	0.278	0.088
$\sigma(\tilde{u}_L) \times \mathrm{BR}(\tilde{u}_L \to \tilde{\tau}_1)$	0.922	0.553	0.293
$\sigma(\tilde{u}_L) \times \mathrm{BR}(\tilde{u}_L \to \tilde{\tau}_1^*)$	4.620	2.754	1.461
$\sigma(\tilde{d}_L) \times \mathrm{BR}(\tilde{d}_L \to \tilde{\tau}_1)$	1.743	1.010	0.518
$\sigma(\tilde{d}_L) \times \mathrm{BR}(\tilde{d}_L \to \tilde{\tau}_1^*)$	0.349	0.203	0.104
$\sigma(\tilde{t}_1) \times \mathrm{BR}(\tilde{t}_1 \to \tilde{\tau}_1)$	0.023	0.018	0.019
$\sigma(\tilde{t}_1) \times \mathrm{BR}(\tilde{t}_1 \to \tilde{\tau}_1^*)$	0.123	0.099	0.121
$\sigma(\tilde{t}_2) \times \mathrm{BR}(\tilde{t}_2 \to \tilde{\tau}_1)$	0.006	0.003	0.002
$\sigma(\tilde{t}_2) \times \mathrm{BR}(\tilde{t}_2 \to \tilde{\tau}_1^*)$	0.026	0.016	0.008
$\sigma(\tilde{b}_1) \times \mathrm{BR}(\tilde{b}_1 \to \tilde{\tau}_1)$	0.025	0.016	0.008
$\sigma(\tilde{b}_1) \times \mathrm{BR}(\tilde{b}_1 \to \tilde{\tau}_1^*)$	0.013	0.008	0.004
$\sigma(\tilde{b}_2) \times \mathrm{BR}(\tilde{b}_2 \to \tilde{\tau}_1)$	0.008	0.004	0.001
$\sigma(\tilde{b}_2) \times \mathrm{BR}(\tilde{b}_2 \to \tilde{\tau}_1^*)$	0.007	0.005	0.001
$\sigma(\tilde{u}_L^*) \times \mathrm{BR}(\tilde{u}_L^* \to \tilde{\tau}_1)$	0.113	0.059	0.027
$\sigma(\tilde{u}_L^*) \times \mathrm{BR}(\tilde{u}_L^* \to \tilde{\tau}_1^*)$	0.022	0.012	0.005
$\sigma(\tilde{d}_L^*) \times \mathrm{BR}(\tilde{d}_L^* \to \tilde{\tau}_1)$	0.022	0.012	0.005
$\sigma(\tilde{d}_L^*) \times \mathrm{BR}(\tilde{d}_L^* \to \tilde{\tau}_1^*)$	0.111	0.055	0.023
$\sigma(\tilde{t}_1^*) \times \mathrm{BR}(\tilde{t}_1^* \to \tilde{\tau}_1)$	0.123	0.099	0.121
$\sigma(\tilde{t}_1^*) \times \mathrm{BR}(\tilde{t}_1^* \to \tilde{\tau}_1^*)$	0.023	0.018	0.019
$\sigma(\tilde{t}_2^*) \times \mathrm{BR}(\tilde{t}_2^* \to \tilde{\tau}_1)$	0.026	0.016	0.008
$\sigma(\tilde{t}_2^*) \times \mathrm{BR}(\tilde{t}_2^* \to \tilde{\tau}_1^*)$	0.006	0.003	0.002
$\sigma(\tilde{b}_1^*) \times \mathrm{BR}(\tilde{b}_1^* \to \tilde{\tau}_1)$	0.013	0.008	0.004
$\sigma(\tilde{b}_1^*) \times \mathrm{BR}(\tilde{b}_1^* \to \tilde{\tau}_1^*)$	0.025	0.016	0.008
$\sigma(\tilde{b}_2^*) \times \mathrm{BR}(\tilde{b}_2^* \to \tilde{\tau}_1)$	0.007	0.005	0.001
$\sigma(\tilde{b}_2^*) \times \mathrm{BR}(\tilde{b}_2^* \to \tilde{\tau}_1^*)$	0.008	0.004	0.001
$\sigma(\tilde{\chi}_2^0) \times \mathrm{BR}(\tilde{\chi}_2^0 \to \tilde{\tau}_1)$	1.304	0.987	0.759
$\sigma(\tilde{\chi}_2^0) \times \mathrm{BR}(\tilde{\chi}_2^0 \to \tilde{\tau}_1^*)$	1.304	0.987	0.759
$\sigma(\tilde{\chi}_1^+) \times \mathrm{BR}(\tilde{\chi}_1^+ \to \tilde{\tau}_1^*)$	3.202	2.404	1.852
$\sigma(\tilde{\chi}_1^-) \times \mathrm{BR}(\tilde{\chi}_1^- \to \tilde{\tau}_1)$	1.881	1.400	1.069
$\sigma(\tilde{\tau}_2) \times \mathrm{BR}(\tilde{\tau}_2 \to \tilde{\tau}_1)$	0.051	0.028	0.004
$\sigma(\tilde{\tau}_2^*) \times \mathrm{BR}(\tilde{\tau}_2^* \to \tilde{\tau}_1^*)$	0.051	0.028	0.004
$\sigma(p \to \tilde{\tau}_1)$	0.245	0.189	0.148
$\sigma(p \to \tilde{\tau}_1^*)$	0.245	0.189	0.148
Total : $\sigma(\tilde{\tau}_1)$	7.309	4.874	3.224
Total : $\sigma(\tilde{\tau}_1^*)$	10.893	7.269	4.758
Number of produced $\tilde{\tau}_1^{(*)}$			
$N(\tilde{\tau}_1)$	730	487	322
$N(\tilde{\tau}_1^*)$	1089	726	475
Number of produced $\tilde{\chi}_1^0$			
$N(\tilde{\chi}_1^0)$	1215	754	593

Table 4.19: Summary of the cross sections and branching ratios and number of the produced staus and neutralinos for $\tan\beta = 30$. We assume the energy in the center-of-mass system as 14 TeV at the LHC experiment. In the estimation of the number of produced staus and neutralinos, we assume the luminosity as 100 fb^{-1}.

Chapter 5

Summary

We have studied the scenario of the CMSSM in which the so-called lithium-7 problem can be solved via internal conversion processes with long-lived staus. For the abundance of lithium-7 to be reduced to the observed one, we imposed the following conditions, that (i) the mass difference of the stau NLSP and the neutralino LSP is smaller than 0.1 (1)GeV, and (ii) the yield value of the stau NLSP is larger than 10^{-13}. The first condition that guarantees enough long lifetime of the stau constrains the stau mass for a fixed neutralino mass, hence the scalar soft mass m_0 and the trilinear coupling A_0, while the second one that guarantees the sufficient reduction of the lithium-7 constrains the upper bound on the neutralino mass or the gaugino soft mass $M_{1/2}$. We analyzed the parameter space as well as the SUSY spectrum of the CMSSM by taking the recent results on the Higgs mass, SUSY searches and the dark matter abundance into account.

In Sec. III, we have shown the allowed region on the A_0-m_0 and m_0-$M_{1/2}$ plane for $\delta m \leq 0.1$ and 1GeV varying $\tan\beta = 10,\ 20$ and 30, respectively. We found a linear relation between A_0 and m_0 in all cases as given in Eq.(4-2-1). The relation originates from the tightly degenerate mass of the stau and the relic abundance of the neutralino. It was also found that the allowed region on A_0-m_0 plane shifts to higher scale as $\tan\beta$ increases. Thus the SUSY spectrum is heavier for large $\tan\beta$. On the other hand, as seen in Fig.4.3, $M_{1/2}$ is constrained between 750(950) and 1050GeV for $\tan\beta = 10(30)$. The upper bound comes from the yield value of the stau while the lower one from the small mass difference and the dark matter abundance. Thus, the conditions required to solve the lithium-7 problem play an important role to determine the allowed region of the CMSSM parameters. Notably, these results naturally lead to heavy SUSY spectrum. The bounds on $M_{1/2}$ lead to the stau mass between 310(400) and 450GeV. Such heavy staus evade the present bound from direct searches at LHC.

In Figs.4.5-4.9, we have shown the SUSY spectrum and the heavier Higgs mass in the allowed region. One can see that the whole spectrum is relatively heavy so that it is consistent with the null results of the SUSY searches at the LHC experiment. Among the spectrum, one of the important predictions is the masses of the gluino and the 1st/2nd generation squarks. In Fig.4.5, it was shown that the the masses are clearly correlated with the neutralino mass. This is the direct consequences from the linear relation of A_0 and m_0. Thus in our scenario, once one of them is determined, the others can be predicted. It is important to emphasize here that the masses of gluino and squarks are constrained between 1.6(1.8) and 2.3TeV for $\tan\beta = 10(30)$. These gluino and squark masses are out of reach at 8 TeV LHC run but really in reach of 14TeV LHC run. The expected numbers of the long-lived staus (nearly degenerate neutralino) to 100fb^{-1} are about 1570 (7200) for the light neutralino mass and 490 (2100) for the heavy one in the case of $\tan\beta = 10$, respectively. With these numbers, the long-lived stau and the nearly degenerate neutralino will be identified easily. Thus our scenario explains why SUSY has not been found yet, and at the same time predicts the early discovery of SUSY in the coming few years. The other important prediction is the stop mass. The stops are also relatively heavy in our scenario. Such stop masses gives large radiative corrections to the Higgs mass, and in fact the Higgs mass is pushed up to 125GeV in sizable regions of the

parameter space. The production cross section of such a lighter stop pair is comparable to those of the gluino and the squarks, and the expected number of the stops to 100fb^{-1} are between 880 and 540. Thus we can expect that the lighter stops also will be found at the 14TeV run of LHC.

The SUSY spectrum is consistent with the present results on muon anomalous magnetic moment within 3 σ and $b \to s+\gamma$ and $B_s \to \mu\mu$ within 1 σ. The direct detection cross section of the neutralino is from 3×10^{-47} to 6×10^{-48}cm^2 and is in reach of LUX/ZEP 20ton.

In conclusion, our scenario is predictive and indeed testable in the coming 14TeV LHC run. When SUSY is the solution of the lithium-7 problem and its breaking is controlled in the CMSSM framework, the time to discover SUSY is coming soon.

acknowledgments

I would like to express my gratitude to my supervisor, Associate Professor Joe Sato, for his expertise, many discussion and advise, and patience.

I appreciate Professor Yoshiaki Tanii for his significant lectures, seminars and examining this paper, and Professor Takeshi Suzuki and Professor Kazuo Hida for examining this paper and valuable comments on my thesis and research.

I also appreciate my collaborators, Toshifumi Jittoh, Kohri Kazunori, Masafumi Koike, Takashi Shimomura, Masato Yamanaka and Koichi Yazaki for collaboration with my research and meaningful discussions. All the members of my laboratory support my student life in various ways. I am grateful to them. Finally I would like to thank to all of the friends and family.

Calculation for changes in yield values of light elements through exotic nuclear reactions

We calculate changes in yield values of light elements through exotic nuclear reactions, e.g. internal conversions, catalyzed fusion reactions, and ^{4}He spallation processes.

Abundances of light elements The observed values of light elements are [119, 121, 128, 129],

$$n_{\rm D}/n_p = (2.80 \pm 0.20) \times 10^{-5}, \tag{-0-1}$$
$$n_{^3{\rm He}}/n_{\rm D} = 0.87 \pm 0.27, \tag{-0-2}$$
$$n_{^7{\rm Li}}/n_p = (2.34 \pm 1.15) \times 10^{-10}, \tag{-0-3}$$
$$n_{^6{\rm Li}}/n_{^7{\rm Li}} = 0.046 \pm 0.022, \tag{-0-4}$$

We express $^6{\rm Li}/n_p$ as follows from Eqs. (-0-4) and (-0-4).

$$\begin{aligned}\frac{n_{^6{\rm Li}}}{n_p} &= \frac{n_{^6{\rm Li}}}{n_{^7{\rm Li}}}\frac{n_{^7{\rm Li}}}{n_p} \\ &= (0.108 \pm 0.051) \times 10^{-10}.\end{aligned} \tag{-0-5}$$

We calculate production of light elements in the form of yield value, and so we rewrote the observed abundances as yield value. Firstly we represent yield value of the p. We calculate the value as follows; Baryon density of the universe is represented in Ref. [131],

$$\Omega_b h^2 = 2.207 \times 10^{-2} \equiv \frac{\rho_b}{\rho_{\rm crit}} h^2, \tag{-0-6}$$

where h is the scale factor of the Hubble expansion rate, $h = 0.673$, ρ_b is the energy density of the baryon, and $\rho_{\rm crit}$ is the critical density of the universe, $\rho_{\rm crit} = 1.054 \times 10^{-5} h^2 ({\rm GeV}/c^2)$ cm^{-3}. The energy density of the baryon is defined as follows;

$$\begin{aligned}\rho_b &\simeq n_p m_p + n_{^4{\rm He}} + m_{^4{\rm He}} \\ &\simeq 2 n_p m_p.\end{aligned} \tag{-0-7}$$

Here we approximate $n_{^4{\rm He}} \simeq 1/4 n_p$ and $m_{^4{\rm He}} \simeq 4 m_p$. The value of n_b is

$$n_b = 2.482 \times 10^{-7} {\rm cm}^{-3}. \tag{-0-8}$$

Therefore, we calculate the value of n_p as follows;

$$n_p = \frac{\Omega_b \rho_{\rm crit}}{2 m_p} = 1.239 \times 10^{-7} {\rm cm}^{-3}, \tag{-0-9}$$

where $m_p = 938.27$ MeV is the mass of a proton. Using n_p, we can calculate the yield value of p as follows;

$$Y_p \equiv \frac{n_p}{s} = 4.287 \times 10^{-11}. \tag{-0-10}$$

Here s is the entropy density of the universe, and we use the today's value, $s_0 = 2891.2$ cm^{-3} [131].

Using Eqs. (-0-1), (-0-4), (-0-3) and (-0-10), we calculate yield value of light elements as follows;

$$Y_{\rm D} = (1.200 \pm 0.086) \times 10^{-15}, \tag{-0-11}$$

$$Y_{^7{\rm Li}} = (1.00 \pm 0.49) \times 10^{-20}, \tag{-0-12}$$

$$Y_{^6{\rm Li}} = (4.63 \pm 2.19) \times 10^{-22}. \tag{-0-13}$$

Numder density of p and D at T We need the number density of D at temperature T in a calculation of the catalyzed fusion, and so we calculate the number density. Firstly we calculate the numder density of p at T , and then we calculate that of D. Since the yield value of p is same at any temperature, we express the number density of p as follows;

$$\begin{aligned} n_p(T) &= \frac{s(T)}{s_0} n_{p,0} \\ &= \left(\frac{T}{T_0}\right)^3 n_{p,0}, \end{aligned} \tag{-0-14}$$

where T_0 is today's temperature, $T_0 = 2.725$ K. We express T in a unit of keV. Using Boltzmann constant $k_B = 8.617$ eV K^{-1}, we rewite the first factor at the right hand side of Eq. (-0-14) as follows;

$$\begin{aligned} \frac{T}{T_0} &= \frac{T}{2.725 \times 8.617 \times 10^{-8}\ {\rm keV}} \\ &= 4.26 \times 10^6 T_{\rm keV}, \end{aligned} \tag{-0-15}$$

where $T_{\rm keV}$ is dimensionless quantity normalized by keV. Therefore, we calculate the number density of p as follows;

$$\begin{aligned} n_p(T) &= 7.72 \times 10^{19} \times 1.24 \times 10^{-7} T_{\rm keV}^3 {\rm cm}^{-3} \\ &= 9.57 \times 10^{12} T_{\rm keV} {\rm cm}^{-3}. \end{aligned} \tag{-0-16}$$

Using Eqs. (-0-16) and (-0-1), we also calculate the number density of D.

$$n_{\rm D}(T) = 2.68 \times 10^8 T_{\rm keV}^3 {\rm cm}^{-3}. \tag{-0-17}$$

Timescale of the catalyzed fusion We calculate the timescale of the catalyzed fusion from now. The analytical expression of the reaction rate is given by [37]

$$N_A \langle \sigma_{\rm CF} v \rangle = 2.37 \times 10^8 \times (1 - 0.34 T_9) T_9^{-2/3} \exp(-5.33 T_9^{-1/3}) {\rm cm}^3 {\rm s}^{-1} {\rm mol}, \tag{-0-18}$$

where N_A is the Avogadro constant, $N_A = 6.02 \times 10^{23}$ mol, σ is the cross section of the reaction, v is relative velocity, $\langle\rangle$ expresses the thermal average, and T_9 is dimensionless temperature in unit of 10^9 K. Here we express T_9 as $T_{\rm keV}$ as follows;

$$\begin{aligned} T_9 &= \frac{T}{10^9 {\rm K}} \\ &= \frac{T}{86.17 {\rm keV}} \\ &= 1.161 \times 10^{-2} T_{\rm keV}. \end{aligned} \tag{-0-19}$$

Using the equation, we rewrite Eq. (-0-18) as follows;

$$\langle \sigma_{\rm CF} v \rangle = 7.68 \times 10^{-15} (1 - 3.95 \times 10^{-3} T_{\rm keV}) T_{\rm keV}^{-2/3} \exp(-23.5 T_{\rm keV}^{-1/3}) {\rm cm}^3 texts^{-1} \tag{-0-20}$$

Conecting the Eqs. (-0-17) and (-0-20), we obtain the reaction rate of the catalyzed fusion as follows;

$$\begin{aligned} \Gamma_{\rm CF} &\equiv \langle \sigma_{\rm CF} v \rangle \\ &= 2.06 \times 10^{-6} T_{\rm keV}^{7/3} (1 - 3.94 \times 10^{-3} T_{\rm keV}) \exp(-23.5 T_{\rm keV}^{-1/3}) {\rm s}^{-1} \end{aligned} \tag{-0-21}$$

The reaction rates at $T = 30, 10$,and 5 keV are 2.60×10^{-6} s^{-1}, 7.65×10^{-9} s^{-1} and 9.05×10^{-11} s^{-1}, respectively.

Effect of the catalyzed fusion on the ^{6}Li abundance We roughly calculate the effect of the catalyzed fusion on the ^{6}Li abundance. The change of the abudance is reperesented as follows;

$$\Delta Y_{^6{\rm Li}} = Y_{\tilde{\tau},{\rm F.O.}} e^{-\tau_{\rm B.F.}/\tau_{\tilde{\tau}}} \frac{\Gamma_{\rm CF}}{\Gamma_{\rm Sp.} + \Gamma_{\tilde{\tau}} + \Gamma_{\rm CF}}, \tag{-0-22}$$

where $\Delta Y_{^6{\rm Li}}$ is the yield value of the ^{6}Li, $\tau_{\rm B.F.}$ is a timescale of (^{4}He $\tilde{l}^-$) formation, $\Gamma_{\tilde{l}}$ is a decay rate of the slepton, $\Gamma_{\rm Sp.}$ and $\Gamma_{\rm C.F.}$ are a reaction rate of the ^{4}He spallation processes and the catalyzed fusion process, respectively. In the equation, $Y_{\tilde{l}^-} e^{-\tau_{\rm B.F.}/\tau_{\tilde{l}}}$ represent a yield value of the bound state, and the factor at the last of right hand side is the branching ratio of the bound state to the catalyzed fusion reaction. Here we consider the allowed region in Fig. 3.4.4, $\delta m \simeq = 0.1$ GeV and $Y_{\tilde{\tau}} \simeq 2 \times 10^{-13}$. We put the constraint from the observed value on the calculated value as follows;

$$\frac{Y_{^6{\rm Li,Ob.}}}{Y_{\tilde{\tau}}} \simeq (2.31 \pm 1.09) \times 10^{-9} \gtrsim e^{-\tau_{\rm B.F.}/\tau_{\tilde{l}}} \frac{\Gamma_{\rm CF}}{\Gamma_{\rm Sp.} + \Gamma_{\tilde{l}} + \Gamma_{\rm CF}}, \tag{-0-23}$$

We take the timescale of the bound state formation 5×10^4 s (see the Fig. 3.3), and $\Gamma_{\rm CF} \simeq 7.65 \times 10^{-9}$ s^{-1}. We see that $\tau_{\tilde{\tau}} \simeq 10^4$ s and $\Gamma_{\rm Sp} \simeq 1$ s^{-1} in the allowed region(see Fig. 3.2) and Fig. (3.7)). We confirm that the calculated yield value of ^{6}Li is consistent with that of the observational value at the allowed region.

Effect of the ^{4}He spallation processes on the D abundance We calculate the effect same way as that of the catalyzed fusion. The change of the abudance is reperesented as follows;

$$\Delta Y_{\rm D} = Y_{\tilde{\tau},{\rm F.O.}} e^{-\tau_{\rm B.F.}/\tau_{\tilde{\tau}}} \frac{\Gamma_{\rm SP}}{\Gamma_{\rm Sp.} + \Gamma_{\tilde{\tau}} + \Gamma_{\rm CF}}, \tag{-0-24}$$

Here we also conside the allowed region in Fig. 3.4.4. We put the constraint from the observed value on the calculated value as follows;

$$\frac{Y_{\rm D,Ob.}}{Y_{\tilde{\tau}}} \simeq (6.00 \pm 0.43) \times 10^{-3} \gtrsim e^{-\tau_{\rm B.F.}/\tau_{\tilde{l}}} \frac{\Gamma_{\rm CF}}{\Gamma_{\rm Sp.} + \Gamma_{\tilde{l}} + \Gamma_{\rm CF}}, \tag{-0-25}$$

We also confirm that the calculated yield value of D is consistent with that of the observational value at the allowed region.

references

[1] G. Aad *et al.* [ATLAS Collaboration], Phys. Lett. B **716** (2012) 1 [arXiv:1207.7214 [hep-ex]].

[2] S. Chatrchyan *et al.* [CMS Collaboration], Phys. Lett. B **716** (2012) 30 [arXiv:1207.7235 [hep-ex]].

[3] S. F. King and P. L. White, Phys. Rev. D **52**, 4183 (1995) [hep-ph/9505326].

[4] B. Bhattacherjee, A. Dighe, D. Ghosh and S. Raychaudhuri, Phys. Rev. D **83**, 094026 (2011) [arXiv:1012.1052 [hep-ph]].

[5] O. Buchmueller, R. Cavanaugh, A. De Roeck, M. J. Dolan, J. R. Ellis, H. Flacher, S. Heinemeyer and G. Isidori *et al.*, Eur. Phys. J. C **72**, 2020 (2012) [arXiv:1112.3564 [hep-ph]].

[6] M. Kadastik, K. Kannike, A. Racioppi and M. Raidal, JHEP **1205**, 061 (2012) [arXiv:1112.3647 [hep-ph]].

[7] D. Ghosh, M. Guchait, S. Raychaudhuri and D. Sengupta, Phys. Rev. D **86**, 055007 (2012) [arXiv:1205.2283 [hep-ph]].

[8] A. Dighe, D. Ghosh, K. M. Patel and S. Raychaudhuri, Int. J. Mod. Phys. A **28**, 1350134 (2013) [arXiv:1303.0721 [hep-ph]].

[9] Y. Okada, M. Yamaguchi and T. Yanagida, Prog. Theor. Phys. **85** (1991) 1.

[10] J. R. Ellis, G. Ridolfi and F. Zwirner, Phys. Lett. B **257** (1991) 83.

[11] H. E. Haber and R. Hempfling, Phys. Rev. Lett. **66** (1991) 1815.

[12] J. A. Casas, J. R. Espinosa, M. Quiros and A. Riotto, Nucl. Phys. B **436** (1995) 3 [Erratum-ibid. B **439** (1995) 466] [hep-ph/9407389].

[13] J. F. Navarro, C. S. Frenk and S. D. M. White, Astrophys. J. **462** (1996) 563 [astro-ph/9508025].

[14] D. Clowe, M. Bradac, A. H. Gonzalez, M. Markevitch, S. W. Randall, C. Jones and D. Zaritsky, Astrophys. J. **648** (2006) L109 [astro-ph/0608407].

[15] V. Springel, J. Wang, M. Vogelsberger, A. Ludlow, A. Jenkins, A. Helmi, J. F. Navarro and C. S. Frenk *et al.*, Mon. Not. Roy. Astron. Soc. **391** (2008) 1685 [arXiv:0809.0898 [astro-ph]].

[16] M. Boylan-Kolchin, V. Springel, S. D. M. White, A. Jenkins and G. Lemson, Mon. Not. Roy. Astron. Soc. **398** (2009) 1150 [arXiv:0903.3041 [astro-ph.CO]].

[17] Q. Guo, S. White, M. Boylan-Kolchin, G. De Lucia, G. Kauffmann, G. Lemson, C. Li and V. Springel *et al.*, Mon. Not. Roy. Astron. Soc. **413** (2011) 101 [arXiv:1006.0106 [astro-ph.CO]].

[18] G. Hinshaw, D. Larson, E. Komatsu, D. N. Spergel, C. L. Bennett, J. Dunkley, M. R. Nolta and M. Halpern *et al.*, arXiv:1212.5226 [astro-ph.CO].

[19] J. L. Feng, K. T. Matchev and T. Moroi, Phys. Rev. Lett. **84** (2000) 2322 [hep-ph/9908309].

[20] J. L. Feng, K. T. Matchev and T. Moroi, Phys. Rev. D **61** (2000) 075005 [hep-ph/9909334].

[21] E. Aprile *et al.* [XENON100 Collaboration], Phys. Rev. Lett. **107** (2011) 131302 [arXiv:1104.2549 [astro-ph.CO]].

[22] A. Fowlie, M. Kazana, K. Kowalska, S. Munir, L. Roszkowski, E. M. Sessolo, S. Trojanowski and Y. -L. S. Tsai, Phys. Rev. D **86**, 075010 (2012) [arXiv:1206.0264 [hep-ph]].

[23] O. Buchmueller, R. Cavanaugh, M. Citron, A. De Roeck, M. J. Dolan, J. R. Ellis, H. Flacher and S. Heinemeyer *et al.*, Eur. Phys. J. C **72** (2012) 2243 [arXiv:1207.7315 [hep-ph]].

[24] K. Griest and D. Seckel, Phys. Rev. D **43** (1991) 3191.

[25] J. Edsjo and P. Gondolo, Phys. Rev. D **56** (1997) 1879

[26] L. Aparicio, D. G. Cerdeno and L. E. Ibanez, JHEP **1204** (2012) 126 [arXiv:1202.0822 [hep-ph]].

[27] M. Citron, J. Ellis, F. Luo, J. Marrouche, K. A. Olive and K. J. de Vries, Phys. Rev. D **87**, 036012 (2013) [arXiv:1212.2886 [hep-ph]].

[28] S. Profumo, K. Sigurdson, P. Ullio and M. Kamionkowski, Phys. Rev. D **71** (2005) 023518 [arXiv:astro-ph/0410714].

[29] T. Jittoh, J. Sato, T. Shimomura and M. Yamanaka, Phys. Rev. D **73** (2006) 055009 [arXiv:hep-ph/0512197].

[30] K. Jedamzik, Phys. Rev. D **70**, 063524 (2004) [arXiv:astro-ph/0402344].

[31] M. Kawasaki, K. Kohri and T. Moroi, Phys. Lett. B **625**, 7 (2005) [arXiv:astro-ph/0402490].

[32] M. Kawasaki, K. Kohri and T. Moroi, Phys. Rev. D **71**, 083502 (2005) [arXiv:astro-ph/0408426].

[33] M. Pospelov, Phys. Rev. Lett. **98**, 231301 (2007) [arXiv:hep-ph/0605215].

[34] K. Kohri and F. Takayama, Phys. Rev. D **76**, 063507 (2007) [arXiv:hep-ph/0605243].

[35] M. Kaplinghat and A. Rajaraman, Phys. Rev. D **74**, 103004 (2006) [arXiv:astro-ph/0606209].

[36] R. H. Cyburt, J. R. Ellis, B. D. Fields, K. A. Olive and V. C. Spanos, JCAP **0611**, 014 (2006) [arXiv:astro-ph/0608562].

[37] K. Hamaguchi, T. Hatsuda, M. Kamimura, Y. Kino and T. T. Yanagida, Phys. Lett. B **650** (2007) 268 [arXiv:hep-ph/0702274].

[38] C. Bird, K. Koopmans and M. Pospelov, Phys. Rev. D **78**, 083010 (2008) [arXiv:hep-ph/0703096].

[39] M. Kawasaki, K. Kohri and T. Moroi, Phys. Lett. B **649**, 436 (2007) [arXiv:hep-ph/0703122].

[40] T. Jittoh, K. Kohri, M. Koike, J. Sato, T. Shimomura and M. Yamanaka, Phys. Rev. D **76** (2007) 125023 [arXiv:0704.2914 [hep-ph]].

[41] K. Jedamzik, Phys. Rev. D **77**, 063524 (2008) [arXiv:0707.2070 [astro-ph]].

[42] D. Cumberbatch, K. Ichikawa, M. Kawasaki, K. Kohri, J. Silk and G. D. Starkman, Phys. Rev. D **76**, 123005 (2007) [arXiv:0708.0095 [astro-ph]].

[43] J. Pradler and F. D. Steffen, Phys. Lett. B **666**, 181 (2008) [arXiv:0710.2213 [hep-ph]].

[44] M. Kawasaki, K. Kohri, T. Moroi and A. Yotsuyanagi, Phys. Rev. D **78**, 065011 (2008) [arXiv:0804.3745 [hep-ph]].

[45] T. Jittoh, K. Kohri, M. Koike, J. Sato, T. Shimomura and M. Yamanaka, Phys. Rev. D **78** (2008) 055007 [arXiv:0805.3389 [hep-ph]].

[46] M. Kusakabe, T. Kajino, T. Yoshida, T. Shima, Y. Nagai and T. Kii, Phys. Rev. D **79**, 123513 (2009) [arXiv:0806.4040 [astro-ph]].

[47] M. Pospelov, J. Pradler and F. D. Steffen, JCAP **0811**, 020 (2008) [arXiv:0807.4287 [hep-ph]].

[48] M. Kamimura, Y. Kino and E. Hiyama, Prog. Theor. Phys. **121**, 1059 (2009) [arXiv:0809.4772 [nucl-th]].

[49] K. Kohri and Y. Santoso, Phys. Rev. D **79**, 043514 (2009) [arXiv:0811.1119 [hep-ph]].

[50] S. Bailly, K. Jedamzik and G. Moultaka, Phys. Rev. D **80**, 063509 (2009) [arXiv:0812.0788 [hep-ph]].

[51] S. Bailly, K. Y. Choi, K. Jedamzik and L. Roszkowski, JHEP **0905**, 103 (2009) [arXiv:0903.3974 [hep-ph]].

[52] R. H. Cyburt, J. Ellis, B. D. Fields, F. Luo, K. A. Olive and V. C. Spanos, JCAP **0910**, 021 (2009) [arXiv:0907.5003 [astro-ph.CO]].

[53] T. Jittoh, K. Kohri, M. Koike, J. Sato, T. Shimomura and M. Yamanaka, Phys. Rev. D **82** (2010) 115030 [arXiv:1001.1217 [hep-ph]].

[54] M. Kusakabe, T. Kajino, T. Yoshida and G. J. Mathews, Phys. Rev. D **81**, 083521 (2010) [arXiv:1001.1410 [astro-ph.CO]].

[55] M. Pospelov and J. Pradler, Phys. Rev. D **82**, 103514 (2010) [arXiv:1006.4172 [hep-ph]].

[56] M. Pospelov and J. Pradler, Ann. Rev. Nucl. Part. Sci. **60** (2010) 539 [arXiv:1011.1054 [hep-ph]].

[57] M. Kawasaki and M. Kusakabe, Phys. Rev. D **83**, 055011 (2011) [arXiv:1012.0435 [hep-ph]].

[58] T. Jittoh, K. Kohri, M. Koike, J. Sato, K. Sugai, M. Yamanaka and K. Yazaki, Phys. Rev. D **84** (2011) 035008 [arXiv:1105.1431 [hep-ph]].

[59] M. Kusakabe, A. B. Balantekin, T. Kajino and Y. Pehlivan, Phys. Lett. B **718** (2013) 704 [arXiv:1202.5603 [astro-ph.CO]].

[60] K. Kohri, S. Ohta, J. Sato, T. Shimomura and M. Yamanaka, Phys. Rev. D **86** (2012) 095024 [arXiv:1208.5533 [hep-ph]].

[61] M. Kusakabe, K. S. Kim, M. -K. Cheoun, T. Kajino and Y. Kino, arXiv:1305.6155 [astro-ph.CO].

[62] L. Monaco, P. Bonifacio, L. Sbordone, S. Villanova and E. Pancino, to the Astron. Astrophys. **519** (2010) L3. arXiv:1008.1817 [astro-ph.GA].

[63] A. Coc, S. Goriely, Y. Xu, M. Saimpert and E. Vangioni, Astrophys. J. **744** (2012) 158 [arXiv:1107.1117 [astro-ph.CO]].

[64] F. Spite and M. Spite, Astron. Astrophys. **115** (1982) 357.

[65] E. W. Kolb and M. S. Turner, *The Early Universe*, Westview Press, (1990)

[66] Barbara ryden, *Introduction to cosmology*, Addison Wesley, (2002)

[67] Katsuhiko Sato and Toshifumi Futamase, UchuronI, Nippon Hyoron Sha, (2008)

[68] A. Coc, J. Phys. Conf. Ser. **420**, 012136 (2013) [arXiv:1208.4748 [nucl-ex]].

[69] Descouvemont P, Adahchour A, Angulo C, Coc A and Vangioni-Flam E, *Atomic Data and Nuclear Data Tables* **88** 203, (2004),

[70] R. H. Cyburt and B. Davids, Phys. Rev. C **78**, 064614 (2008) [arXiv:0809.3240 [nucl-ex]].

[71] S. Ando, R. H. Cyburt, S. W. Hong and C. H. Hyun, Phys. Rev. C **74**, 025809 (2006) [nucl-th/0511074].

[72] E. Komatsu *et al.* [WMAP Collaboration], Astrophys. J. Suppl. **192**, 18 (2011) [arXiv:1001.4538 [astro-ph.CO]].

[73] A. Coc, E. Vangioni-Flam, P. Descouvemont, A. Adahchour and C. Angulo, Astrophys. J. **600**, 544 (2004) [astro-ph/0309480].

[74] S. G. Ryan, T. C. Beers, K. A. Olive, B. D. Fields and J. E. Norris, Astrophys. J. **530** (2000) L57.

[75] R. H. Cyburt, B. D. Fields and K. A. Olive, JCAP **0811** (2008) 012 [arXiv:0808.2818 [astro-ph]].

[76] Coc A and Vangioni E 2010, *Journal of Physics Conference Series* **202** 012001

[77] L. Sbordone, P. Bonifacio, E. Caffau, H. -G. Ludwig, N. T. Behara, J. I. G. Hernandez, M. Steffen and R. Cayrel *et al.*, Astron. Astrophys. **522**, A26 (2010) [arXiv:1003.4510 [astro-ph.GA]].

[78] E. Aver, K. A. Olive and E. D. Skillman, JCAP **1103**, 043 (2011) [arXiv:1012.2385 [astro-ph.CO]].

[79] E. Aver, K. A. Olive and E. D. Skillman, JCAP **1204**, 004 (2012) [arXiv:1112.3713 [astro-ph.CO]].

[80] K. A. Olive, P. Petitjean, E. Vangioni and J. Silk, arXiv:1203.5701 [astro-ph.CO].

[81] Bania T, Rood R and Balser D 2002 *Nature* **415** 54

[82] H. A. Bethe, E. E. Salpeter, *Quantun Mechanics of One-and Two- Electron Atoms*, SpringerVerlag OHG. Berlin Gottingen Heidelberg (1957)

[83] D. Borisyuk, Nucl. Phys. A **843**, 59 (2010) [arXiv:0911.4091 [hep-ph]].

[84] G. Kubon *et al.*, Phys. Lett. B **524** (2002) 26 [arXiv:nucl-ex/0107016].

[85] C. W. Wong, Int. J. Mod. Phys. E **3**, 821 (1994).

[86] M. Yoshitake *et al.*, private communication.

[87] P. Egelhof, Prog. Part. Nucl. Phys. **46**, 307-316 (2001)

[88] P. J. Mohr, B. N. Taylor, and D. B. Newell, Rev. Mod. Phys. **80**, 633 (2008)

[89] R. B. Firestone, *Table of Isotopes. Eighth Edition Volume I*, John Wiley and Sons Inc, New York, (1999)

[90] G. Belanger, F. Boudjema, A. Pukhov and A. Semenov, arXiv:1305.0237 [hep-ph].

[91] [CMS Collaboration], CMS-PAS-HIG-12-045. ATLAS:2012klqCMS:aya

[92] [ATLAS Collaboration], ATLAS-CONF-2012-170.

[93] B. C. Allanach, eConf C **010630**, P319 (2001) [hep-ph/0110227].

[94] A. Djouadi, hep-ph/0211357.

[95] B. C. Allanach, S. Kraml and W. Porod, JHEP **0303**, 016 (2003) [hep-ph/0302102].

[96] B. C. Allanach, A. Djouadi, J. L. Kneur, W. Porod and P. Slavich, JHEP **0409**, 044 (2004) [hep-ph/0406166].

[97] W. Porod, Comput. Phys. Commun. **153** (2003) 275 [hep-ph/0301101].

[98] W. Porod and F. Staub, Comput. Phys. Commun. **183** (2012) 2458 [arXiv:1104.1573 [hep-ph]].

[99] S. Heinemeyer, W. Hollik and G. Weiglein, Comput. Phys. Commun. **124** (2000) 76 [hep-ph/9812320].

[100] S. Heinemeyer, W. Hollik and G. Weiglein, Eur. Phys. J. C **9** (1999) 343 [hep-ph/9812472].

[101] G. Degrassi, S. Heinemeyer, W. Hollik, P. Slavich and G. Weiglein, Eur. Phys. J. C **28** (2003) 133 [hep-ph/0212020].

[102] M. Frank, T. Hahn, S. Heinemeyer, W. Hollik, H. Rzehak and G. Weiglein, JHEP **0702** (2007) 047 [hep-ph/0611326].

[103] S. P. Martin, In *Kane, G.L. (ed.): Perspectives on supersymmetry II* 1-153 [hep-ph/9709356].

[104] J. Pradler and F. D. Steffen, Nucl. Phys. B **809**, 318 (2009) [arXiv:0808.2462 [hep-ph]].

[105] S. Chatrchyan *et al.* [CMS Collaboration], arXiv:1305.0491 [hep-ex].

[106] [ATLAS Collaboration], ATLAS-CONF-2013-037 .

[107] G. W. Bennett *et al.* [Muon G-2 Collaboration], Phys. Rev. D **73** (2006) 072003 [hep-ex/0602035].

[108] M. Davier, A. Hoecker, B. Malaescu and Z. Zhang, Eur. Phys. J. C **71**, 1515 (2011) [Erratum-ibid. C **72**, 1874 (2012)] [arXiv:1010.4180 [hep-ph]].

[109] K. Hagiwara, R. Liao, A. D. Martin, D. Nomura and T. Teubner, J. Phys. G **38** (2011) 085003 [arXiv:1105.3149 [hep-ph]].

[110] RAaij *et al.* [LHCb Collaboration], Phys. Rev. Lett. **111**, 101805 (2013) [arXiv:1307.5024 [hep-ex]].

[111] S. Chatrchyan *et al.* [CMS Collaboration], Phys. Rev. Lett. **111**, 101804 (2013) [arXiv:1307.5025 [hep-ex]].

[112] Y. Amhis *et al.* [Heavy Flavor Averaging Group Collaboration], arXiv:1207.1158 [hep-ex].

[113] J. beringer *et al.* [Partticle Data Group Collaboration], Phys. Rev. D **86** (2012) 010001

[114] G. Jungman, M. Kamionkowski and K. Griest, Phys. Rept. **267** (1996) 195 [hep-ph/9506380].

[115] E. Aprile *et al.* [XENON100 Collaboration], Phys. Rev. Lett. **109** (2012) 181301 [arXiv:1207.5988 [astro-ph.CO]].

[116] E. Aprile [XENON1T Collaboration], arXiv: 1206.6288 [astro-ph.IM].

[117] D. S. Akerib *et al.* [LUX Collaboration], Astropart. Phys. **45** (2013) 34 [arXiv:1210.4569 [astro-ph.IM]].

[118] A. Belyaev, N. D. Christensen and A. Pukhov, Comput. Phys. Commun. **184** (2013) 1729 [arXiv:1207.6082 [hep-ph]].

[119] J. Melendez and I. Ramirez, Astrophys. J. **615** (2004) L33 [arXiv:astro-ph/0409383].

[120] P. Bonifacio *et al.*, Astron. Astrophys. **462** (2007) 851 [arXiv:astro-ph/0610245].

[121] M. Asplund, D. L. Lambert, P. E. Nissen, F. Primas and V. V. Smith, Astrophys. J. **644** (2006) 229 [arXiv:astro-ph/0510636].

[122] W. Aoki *et al.*, Astrophys. J. **698** (2009) 1803 [arXiv:0904.1448 [astro-ph.SR]].

[123] R. H. Cyburt, B. D. Fields and K. A. Olive, Phys. Rev. D **69** (2004) 123519 [arXiv:astro-ph/0312629].

[124] C. Angulo *et al.*, Astrophys. J. **630** (2005) L105 [arXiv:astro-ph/0508454].

[125] O. Richard, G. Michaud and J. Richer, Astrophys. J. **619**, 538 (2005) [arXiv:astro-ph/0409672].

[126] A. J. Korn *et al.*, Nature **442** (2006) 657 [arXiv:astro-ph/0608201].

[127] K. Lind, F. Primas, C. Charbonnel, F. Grundahl and M. Asplund, arXiv:0906.2876 [astro-ph.SR].

[128] M. Pettini, B. J. Zych, M. T. Murphy, A. Lewis and C. C. Steidel, MNRAS, **391** (2008) 1499 [arXiv:0805.0594 [astro-ph]].

[129] J. Geiss and G. Gloeckler, Space Sience Reviews **106**, 3 (2003).

[130] O. Erken, P. Sikivie, H. Tam and Q. Yang, arXiv:1104.4507 [astro-ph.CO].

[131] P. J. Mohr, B. N. Taylor, and D. B. Newell, CODATA Recommended Values of the Fundamental Physical Constants, Rev. Mod. Phys, **84, 1527 (2012)**